Diana Oberbichler, B.Sc.

01210798

Investigation of the Rockfall Fragmentation at a Recent Case Study in the Gschliefgraben (Gmunden, Upper Austria)

Master's Thesis

Submitted in fulfilment of the requirements for the degree of

Master of Science

Master's programme – Earth Science

at

Graz University of Technology

Supervisors

Buyer, Andreas Anjan, B.Sc. M.Sc.

Institute of Rock Mechanics and Tunneling

Graz University of Technology

Univ.-Prof. Dipl.-Ing. Dr.techn. Roman Marte

Institute of Soil Mechanics and Foundation Engineering

Graz University of Technology

Ao.Univ.-Prof. Mag.rer.nat. Dr.rer.nat. Qian Liu

Institute of Applied Geoscience

Graz University of Technology

Graz, May 2018

EIDESSTATTLICHE ERKLÄRUNG

AFFIDAVIT

Ich erkläre an Eides statt, dass ich die vorliegende Arbeit selbstständig verfasst, andere als die angegebenen Quellen/Hilfsmittel nicht benutzt, und die den benutzten Quellen wörtlich und inhaltlich entnommenen Stellen als solche kenntlich gemacht habe. Das in TUGRAZonline hochgeladene Textdokument ist mit der vorliegenden Masterarbeit identisch.

I declare that I have authored this thesis independently, that I have not used other than the declared sources/resources, and that I have explicitly marked all material which has been quoted either literally or by content from the used sources. The text document uploaded to TUGRAZonline is identical to the present master‘s thesis.

Datum / Date

Unterschrift / Signature

Danksagung

Habt Dank ihr alle, die dies hier lesen oder bereits gelesen haben!

Ein Dankeschön an meine Betreuer Herrn Roman Marte und Herrn Qian Liu fürs Zeitnehmen zur Überarbeitung und Beurteilung meiner Masterarbeit. Jedoch ein ganz besonderes Dankeschön an Andreas Buyer, welcher mich mit Geduld und Beständigkeit, wiederholenden Diskussionen und ehrlichen Kritiken durchwegs motiviert und begleitet hat. Ohne dich, Andi, wäre dies hier gar nicht zustande gekommen.

Auch ein herzliches Dankeschön an meine liebe Mama und meinen lieben Papa, Kerstin, meine lieben Geschwister Petra, Branko, Arnika, Gonda, Silvan und Sirius. Eure lieben Worte, eure Unterstützung und oft auch nur eure Gegenwart geben mir so viel. Ich hab euch alle sehr lieb!

Und noch zu meinen Lieblingsmenschen, die ich erst während meiner Zeit hier in Graz kennen und so sehr zu schätzen gelernt habe. Ihr, meine Freunde der Steine und Berge, habt mit unvergesslichen Zeiten, in denen tiefschürfende sowie hochtrabende Gespräche geführt wurden, mit träneneichen Lachanfällen, herzerwärmenden Knuddeleinheiten und fantastischen Augenblicken für immer einen Platz in meinem Herzen eingenommen. Danke, dass ich immer auf euch zählen kann, selbst wenn oft, aber nicht immer, Halligalli ist.

Danke Anna, Isa und Katja für die wundervollen Aperitivino- Abende! Und Danke Katja, dass ich immer ein Plätzchen bei dir und deiner superwitzigen WG habe. Auch einen Dank an Luki für die einmalige letzte Zeit in Graz und deinen unbändigen Willen die sonst so alltäglichen Abende mit Kunst, Kultur und abenteuerreichen Unternehmungen zu füllen. Des Weiteren auch ein Danke an dich, liebe Karin! Weil du wie eine Schwester für mich bist. Deine Einzigartigkeit inspiriert jeden, seine besten Seiten hervorzubringen.

Und auch ein Zu-wenig-gesagtes-aber-oft-Gemeintes Dankeschön an all die wunderbaren Leute, denen ich begegnen durfte und die mich ein ganzes Stückchen während meiner Zeit hier begleitet haben.

Abstract

Modelling and the simplification of natural processes often involve great uncertainties.

In this thesis, a rockfall event in 2014 is investigated in detail. Therefore, in the field, the accumulation area investigated to reconstruct the theoretical rock mass before the rockfall event. There, the three block axes of boulders in the debris are recorded. The minimum boulder size was set to 0.2 m^3. Furthermore, data was acquired during the field work to generate a digital surface model (DSM), which is used to map discontinuities in the outcrop with JMX Analyst in ShapeMetriX^{3D}, where four heavily scattered joint sets could be identified. The orientation and size of the discontinuities is used to identify areas in the investigated rock cliff, which pose a higher potential for future failures. These areas are characterized by an overhanging morphology, intersections of discontinuities and fresh outbreaks. In addition, a kinematic analysis, based on the investigation of the discontinuity surfaces in the detachment area of the rockfall was performed. This indicates the failure on a steeply inclined, planar surface along which the rockfall material slips off.

The orientation and spacing of the discontinuities are used to determine and illustrate the theoretical in-situ block size (IBSD) and block shape distribution (BSD) as well as the theoretical orientation of the blocks using the program 3DEC. The results are compared to the residual block fragments in the deposit. 3DEC reveals elongated block shapes and widely distributed block sizes with a mean block volume of 31.43 m^3. In contrast, the mapped block fragments in the accumulation area of the rockfall are dominated by cubic to columnar shapes and the corresponding $\bar{V}$ is 3.80 m^3. The difference can be explained by an overestimation of the joint normal spacing of a sub-horizontal joint set and persistence. Additionally, the high bending moment of elongated blocks is assumed to cause fraction during the rockfall event.

The geometry of the joint network in the detachment area is also used to generate a fragmentation model in UDEC. Based on the modelling of a block fitted to the geometry of the detachment area, the effects of joint normal (jkn) and joint shear (jks) stiffness and the cohesion (c) on the behaviour of the rockfall are investigated. The values for jkn range from 1E13 Pa/m to 1E11 Pa/m, for jks from 1E13 Pa/m to 1E5 Pa/m, decreasing by the power of 10. The cohesion is reduced from 2E7 Pa to zero. The results reveal disintegration at the first impact at jkn = 1E13 Pa/m, jks = 1E13 Pa/m and c = 0 Pa and jkn = 1E13 Pa/m, jks = 1E12 Pa/m and c = 2E7 Pa, respectively.

Kurzfassung

Die Modellierung und die damit einhergehende Vereinfachung natürlicher Prozesse ist häufig mit großen Unsicherheiten verbunden.

Im Zuge dieser Arbeit wurde ein Steinschlag aus dem Jahr 2014 untersucht. Die im Gelände durchgeführte Untersuchung des Akkumulationsbereichs dient zur Rekonstruktion der theoretischen Masse vor dem Steinschlag. Hierbei werden die drei Blockachsen gemessen, wobei als Untergrenze der Messung ein Wert von 0,2 m³ angenommen wird. Darüber hinaus wurden in der Geländearbeit Daten erfasst, um ein digitales Oberflächenmodell zu generieren. Die Trennflächen im Aufschluss werden mit dem JMX Analyst in ShapeMetriX^{3D} erfasst werden, wobei vier chaotisch orientierte Trennflächensets identifiziert werden konnten.

Die Trennflächenorientierung wird verwendet, um Bereiche in der Felswand mit einem erhöhten Versagenspotenzial zu definieren. Diese Bereiche zeichnen sich durch eine überhängende Morphologie, Verschneidungen von Trennflächen und frischen Ausbrüchen aus. Zusätzlich wird eine kinematische Analyse durchgeführt, die auf der Untersuchung der Trennflächen im Ablösungsbereich des Steinschlags beruht und das Versagen auf einer steil geneigten, planaren Fläche anzeigt, auf der das Steinschlagmaterial abrutscht.

Orientierungen und der Abstand der Trennflächen werden verwendet, um die theoretische in-situ Blockgrößen- (IBSD) und Blockformverteilung (BSD), sowie die Orientierung der Blöcke mittels 3DEC zu bestimmen. Die Ergebnisse werden mit den kartierten Blockfragmenten im Ablagerungsbereich verglichen. Die 3DEC-Modelle zeigen überwiegend längliche Blockformen mit einem Durchschittsvolumen von 31.43 m³. Im Gegensatz dazu werden die kartierten Blockfragmente von kubischen bis säulenförmigen Formen dominiert und das entsprechende $\bar{V}$ beträgt 3.80 m³. Der Unterschied kann durch eine Überschätzung des Normalabstandes einer subhorizontalen Trennflächenschar, der Persistenz und durch das hohe Biegemoment der länglichen Blöcke während des Steinschlags, welches zu einer Fragmentierung führt, erklärt werden.

Die Trennflächengeometrie wird zudem für die numerische Simulation der Fragmentierung (UDEC) verwendet. Basierend auf der Modellierung eines an den Ablösebereich angepassten Blocks wurden die Auswirkungen der Steifigkeit der Trennflächennormal- (jkn) und der Trennflächenschersteifigkeit (jks), sowie der Kohäsion (c) untersucht. Die Werte für jkn liegen im Bereich von 1E13 Pa/m bis 1E11 Pa/m, für jks von 1E13 Pa/m bis 1E5 Pa/m. Die Kohäsion wird von 2E7 Pa auf null reduziert. Die Ergebnisse zeigen einen Zerfall bei dem ersten Stoß bei jkn = 1E13 Pa/m, jks = 1E13 Pa/m und c = 0 Pa und jkn = 1E13 Pa/m, jks = 1E12 Pa/m bzw. c = 2E7 Pa.

Table of Contents

List of figures

List of tables

Abbreviations

IBSD................in-situ block size distribution

RBSD..............resultant block size distribution

BSD................block shape distribution

NCA ....Northern Calcareous Alps

GBA ....Geologische Bundesanstalt or Geological Survey of Austria

DSM ....digital surface model

E_{pot}.................potential energy [J]

SS ....structure set

jkn ....joint normal stiffness [Pa/m]

jks..................joint shear stiffness [Pa/m]

c ....cohesion [Pa]

1 Introduction

1.1 Relevance of the Topic

The environment of the Alpine region is sensitive to external influences. Therefore, the climate change has a strong impact. The average temperature within the Alps increased by 1.6°C, since climatic recordings have been available and is prompted to increase up to 4°C [1]. As a consequence, this affects the thawing of permafrost and precipitation. In Austria, regional climate models show an increase of precipitation by 7 to 9 %. Both, thawing of permafrost and the increase of precipitation, are a causal factor for slope instability and further gravitational mass movements [2,3].

Furthermore, in Alpine regions topological and geological features, such as steep flanks and unstable surfaces restrict habitable areas. As the population in Austria increased to 8.77 Mio. in 2017 [4], more habitable space is needed and remote areas at higher risk are cultivated with the establishment of infrastructure and buildings [5]. This accounts also for an increased trend for outdoor activities. According to the ÖGG [6], it can be roughly estimated that annually two people die as a consequence of rockfalls or landslides.

Summarizing, gravitational mass movements, such as landslides, rockfalls, denudation, and others pose a high risk for infrastructural facilities, buildings and people. Figure 1 displays mass movements events such as rockslides, rockfalls, rock avalanches and slumpings in Austria [7]. Rockslides and rockfalls are dominant in areas with exposed hard rock faces, such as in the Central Alps and in the Northern Calcareous Alps.

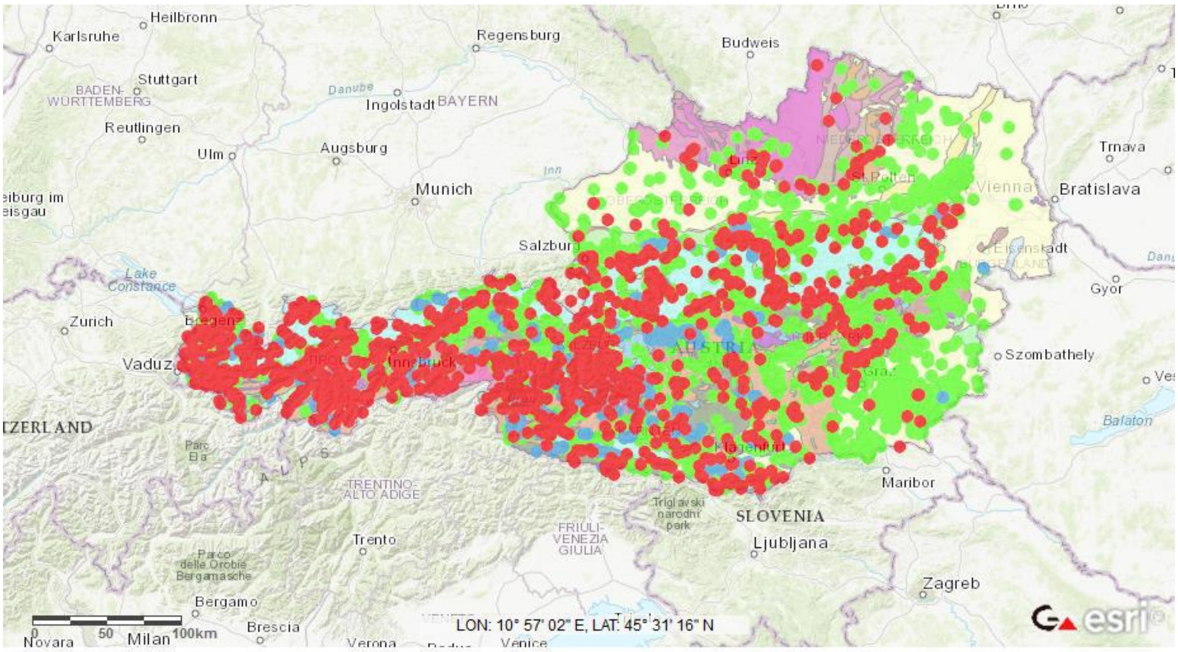

Figure 1: Distribution of mass movements in Austria, which are of economical and scientific interest but may not necessarily pose a risk for human and infrastructure [7]; red: rockslides and rockfalls, green: slumpings, blue: debris flows, sagging

In both natural processes and engineering activities, the behaviour of rock is affected by the presence and characteristics of geological structures. Thus, for better risk management of rockfall events, it is important to provide proper investigation programs for dimensioning protection and/or remedial measures. In literature [5,8–10], various site specific geotechnical assessments are proposed. This includes an assessment of the rock source area, geological description, the possible kinematic energy, run-out lengths and the level of damage. Additionally, current risk analysis attempts to take rock fragmentation into consideration. Fragmentation, which is defined as the reduction of particle size due to the application of an action, is frequently observed during rockfalls, but due to its physical complexity difficult to consider in rockfall analysis [11].

This thesis aims to incorporate joint set parameters resulting from discontinuity mapping of a DSM in a theoretical distribution of in-situ blocks on the one hand. On the other hand, it tries to improve the understanding of the transformation of the theoretical in-situ block size distribution (IBSD) and block shape distribution (BSD) in the cliff and the observed resultant block size distribution (RBSD) considering fragmentation.

1.2 Formulation of the Research Question

Discontinuity mapping serves to deal with the following question:

- Exist further areas/zones at higher risk and potential failure in the investigated rock wall?

Additionally, this thesis aims to improve existing investigation methods and assumptions by satisfying the following issues:

- Is there a connection between the RBSD and the IBSD after a fragmentation process?
- Can this fragmentation process be simulated numerically, and which parameters are sensitive?

Basis for these research questions are observations in the field which are related to results of modelling and inversely.

2 Study Site

2.1 Geographical Setting

The study site is located in Gmunden, in the south-western part of Upper Austria, the so-called Salzkammergut (Figure 2). The investigated rockfall detached from a steep cliff at the northern flank of the Traunstein Mountain. The mapped area within the rock cliff has a height of about 168 m from the debris accumulation area to the top and a width of about 262 m. Its debris accumulates about 20 m above a forest path, which was constructed for remediation work of the Gschliefgraben-Landslide. The landslide, which is reactivated regularly [12], is bordered by the mountains Traunstein (south) and Grünberg (north) and the lake Traunsee (west).

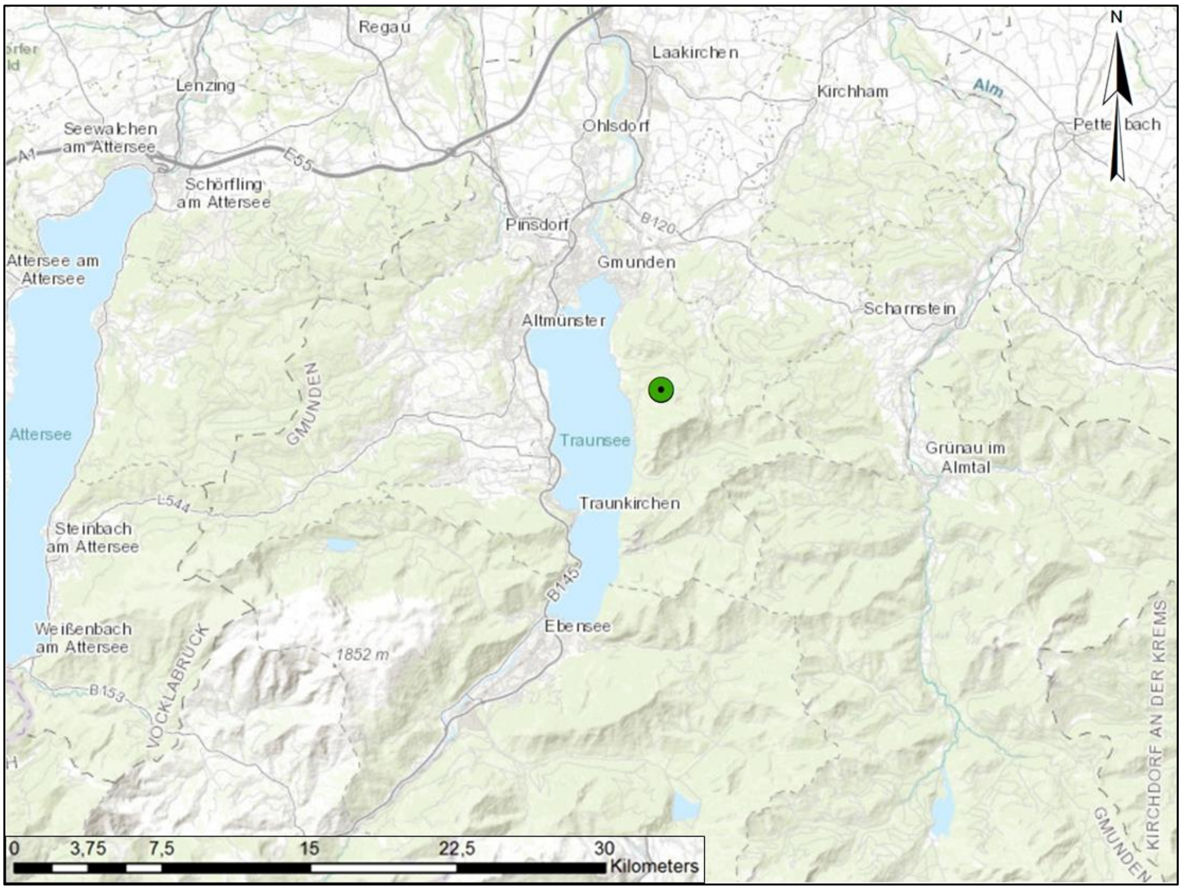

Figure 2: Overview of the region Salzkammergut (Austria); the green marker indicates the location of the investigated rockfall (source: Esri, DeLome, USGS, NPS)

2.2 Geological Setting

Within the Northern Calcareous Alps (NCA), the studied rockfall borders the tectonic window of the “Ultrahelvetic” [13]. There is a well-known boundary of the Flysch Nappe and the Calcareous Alps, which overthrusted the Ultrahelvetic rocks. Figure 3 displays the geological units of the intermediate surrounding of the investigated rockfall.

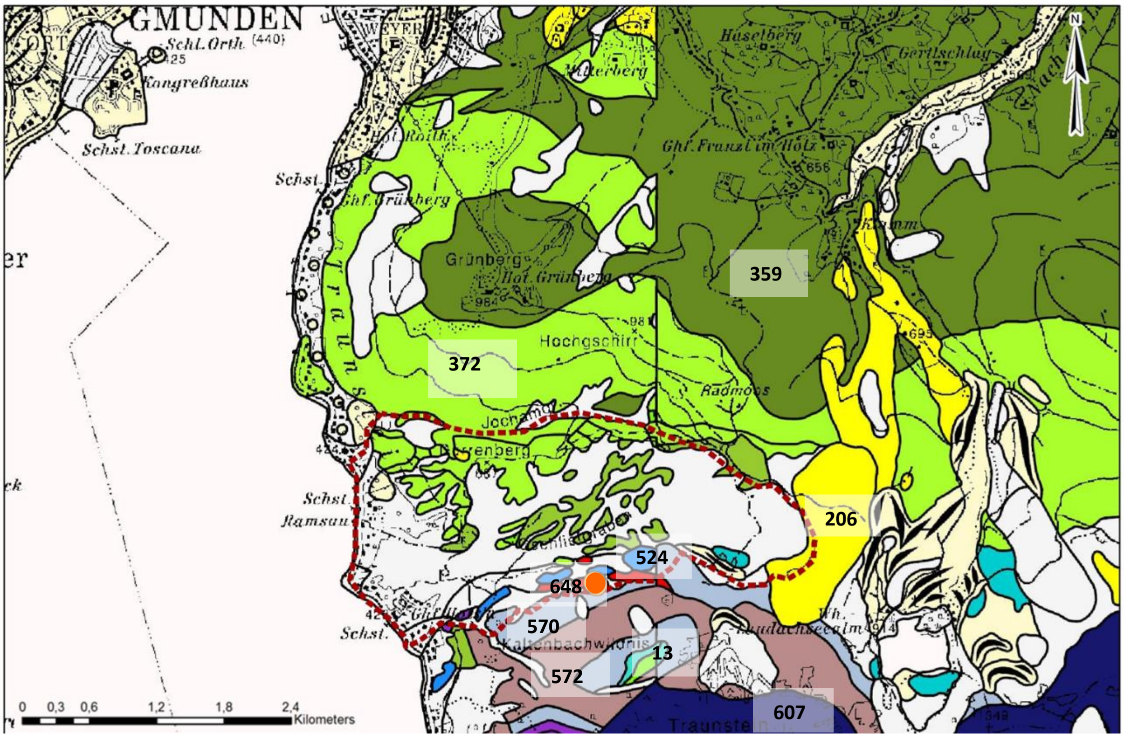

Figure 3: Geological units around the investigation site; red, dashed line indicates the Gschliefgraben-landslide; orange marker indicates the location of the investigated rockfall; 13 – talus deposit, 206 – debris flow breccia, 359 – “Altlengbach”- Formation (“Buntmergelserie”), 372 – “Zementmergelserie” (Rhenodanubic Flysch), 524 – Liassic Limestone, 570 – Jurassic Limestone, 572 – Main Dolomite, 607 – “Wetterstein”- Formation, 648 – “Haselgebirge”

During the orogenesis of the Alps, the NCA have been transported over the crystalline units of the Central Alps and overthrusted the Flysch Zone and the Molasse Zone. As a result, the Northern foothills were exposed to major tectonic stress that caused brittle structures, such as faults and chaotic joint networks. A major fault separates the overlaying Main Dolomite and “Wetterstein”-formation of the NCA from the Jurassic Limestone in the footwall [14]. These structures can be found in the outcrop of the investigated rockfall, which is composed of limestone of the “Kalkofenzug”-formation. This carbonaceous formation contains clay and gypsum and belongs probably to the “Haselgebirge” [13,15–17].

3 Methodology

The methodology can be divided into two main aspects. First, field work is performed to measure field parameters, such as the residual block size and shape distribution over the whole accumulation area. Additionally, photos were taken from the opposite site of the Gschliefgraben to generate a 3D digital surface model for the discontinuity mapping. For the second part the discontinuity characterization is used in order to determine the in-situ block size and shape distribution and further model the influence of joint parameters on the fragmentation process.

3.1 Field Work

3.1.1 *Determination of the Residual Block Size and Shape Distribution*

The determination of block size and shape distribution has always been important for the design in engineering projects. In this thesis the size and geometry of the blocks in the deposit of the rockfall are measured in the fieldwork [18]. The three axes were recorded, where the x-axis corresponds to the longest, the y-axis to the middle and the z-axis to the shortest (Figure 4). The threshold for the minimum length of the x-axis was set to be 70 cm. As a result, the minimum volume of a block was calculated to be 0.2 m³.

Figure 4: Exemplary measurement of a block in the field; pink marks indicate the measured axes (x,- y-, z-axis); bar in the upper right corner of the block has a dimension of 20 cm.

There are various approaches to classify the block shape [19–22]. As the method by Franklin and Dusseault [19] is common in practice, their method is chosen for descriptions in the field. It characterizes the block shape using the ratio of the middle axis to the longest and the ratio of the shortest to the longest. This reveals the dependency on the number of joint sets, their relative orientation and spacings. Another method after Kalenchuck et al. [22] which is selected for IBSD and BSD classification in this thesis derived from 3DEC modelling suggests using two geometric factors, α and β. Where α reflects the relation of surface area and volume of an arbitrary object to define its flatness, and β the co-linearity of the longest vertex-to-vertex distance to discriminate the elongation of an object.

3.1.2 *Generation of the Digital Surface Model*

In order to obtain a DSM, photos are taken from the Grünberg Mountain side, using a calibrated DSL Canon EOS 70D, with an objective lens Tamron AF 70- 200 mm. Seven different positions are selected, from where the reference targets, placed in the accumulation area, the rock cliff, as well as the detachment area, are clearly visible. The distances of the camera positions to the rock cliff ranged from 300 to 1150 m. The images are processed with a structure from motion implementation of the software ShapeMetriX^{3D} in order to generate a high-resolution point cloud. The characteristics of the generated point cloud are listed in Table 1. The DSM is scaled, normalized and referenced to north.

Table 1: Statistical data of the DSM

Parameter	**Value**
Number of Subimages	155
Number of 3D points	1,448,517
Total surface area [m^2]	188,227.6
Average geometric image resolution [m/pt]	0.01
Average 3D point spacing [m/pt]	0.36
Image size [MP]	1,878.93

3.2 Numerical Processing

3.2.1 *Mapping of the Discontinuities with JMX Analyst*

JMX Analyst, provided by the software ShapeMetriX^{3D} (3GSM GmbH), enables the digital mapping of discontinuity in the investigated outcrop [23].

At first, the planes of the local detachment area were mapped in detail and clustered according to their orientation. The manual identification of the planes within the detachment area covers precisely its reliefs and is controlled by its outbreak contours. In the second step, the global joint network of the entire rock wall was mapped. This step increases the statistical reliability of the determined global discontinuity characteristics, such as set orientation and spacing, used in the numerical modelling. The mapped joints were semi-automatically clustered to their respective joint set orientation with the SMX implemented k-means clustering algorithm [23].

Apart from discontinuity mapping, an estimation of the volume of the detached rock mass has been performed. Therefore, the tool "Volume" in the JMX Analyst is used. The tool generates a closed polyhedron by extrapolating and connecting a mapped polygon with the DSM. The distance between the polyhedron and the point cloud of the DSM yield an approximation of the volume for the rockfall.

3.2.2 *Kinematic and Risk Analyses*

Both, the failure mechanism of the rockfall event and the most common failure modes of further events in the investigated rock wall are identified with the program Dips 7.0 [24]. Therefore, the orientation of the set planes of the previously conducted discontinuity mapping (Appendix) and the mean slope orientation (325/74) are used. The orientation of the slope results from averaging the orientation of the points in the DSM. For the friction angle a value of 30° is assumed. Moreover, it is important to consider that further internal properties of the jointed rock mass, such as persistence, or seepage pressure, are unknown and cannot be defined. Thus, the kinematic analysis indicates only the theoretical behaviour of all intersecting discontinuities within the rock mass and also the intersection with the slope.

The failure modes planar and wedge sliding, as well as direct and flexural toppling are considered (Figure 5). Planar sliding occurs under gravity when a block daylights slipping on a plane of weakness of which the inclination is greater than its friction angle, whereas wedge sliding results from the intersection of two discontinuities [25]. Failure can occur when the line of intersection daylights into the slope. Direct toppling occurs when the centre of gravity of a block is outside its base and as a consequence an overturning moment develops. Regarding flexural toppling, an interlayer slip is induced that causes fraction [26].

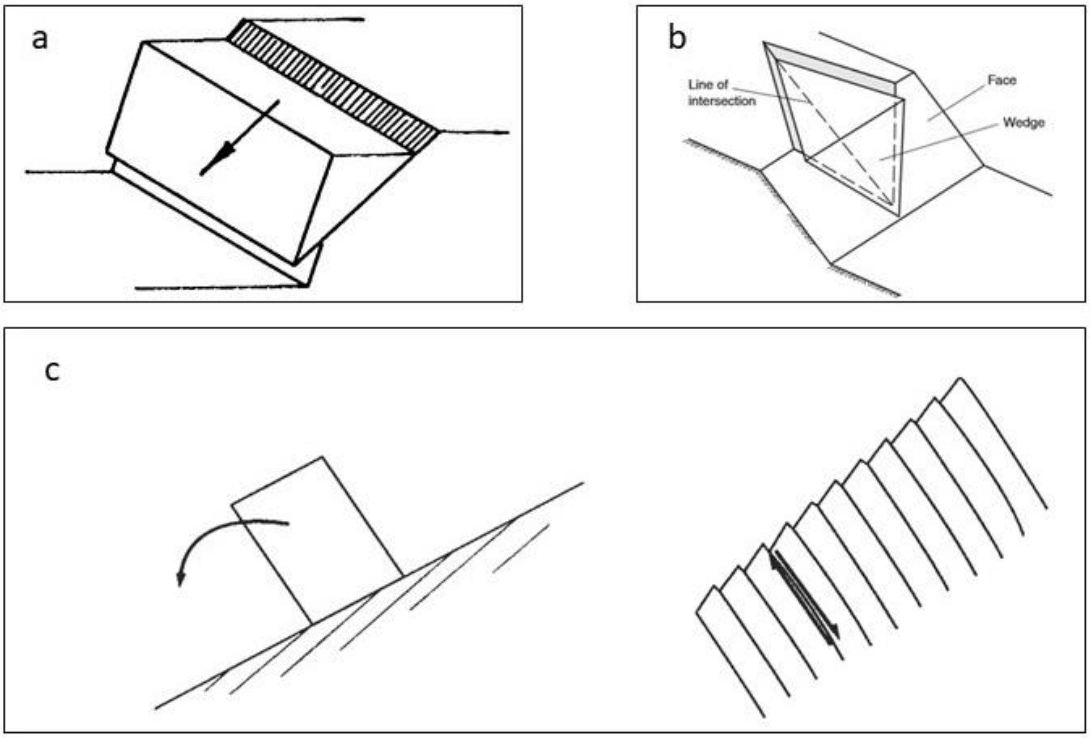

Figure 5: Kinematic behaviour of failures; a) planar sliding [27], b) wedge sliding [27], c) direct toppling [26], d) flexural toppling [26]

Furthermore, to define areas which indicate a higher risk for rockfalls, the topography of the cliff in the DSM was examined in detail. The determination of these areas and of removable blocks, respectively, follows three main criteria:

- The intersection of critical joint sets, which may destabilize the rock mass [27]
- Overhanging areas increasing the rockfall probability for slope-parallel discontinuity sets [28]
- Recent detachments indicating active failing zones

If these criteria are fulfilled within an area, it is defined as being susceptible for rockfall events.

To identify critical joint intersections, the tool "Discontinuity" in the JMX Analyst is used, indicating a plane which expands the theoretical spatial extension of the joint plane [23]. It is defined by the position and orientation (normal vector, or dip direction and dip, and ε-angle which depends on the discontinuity shape). Overhanging areas are mapped by visual aspects and fresh outbreaks in the DSM.

Furthermore, for the kinematic analysis of the investigated rockfall event, the detachment area was also investigated in detail. A joint plane was assumed to act as a failure plane for the detaching material (Figure 6). Hence, in this case, the orientation of this plane, which is (306/85), was used as the slope direction in the stability analyses.

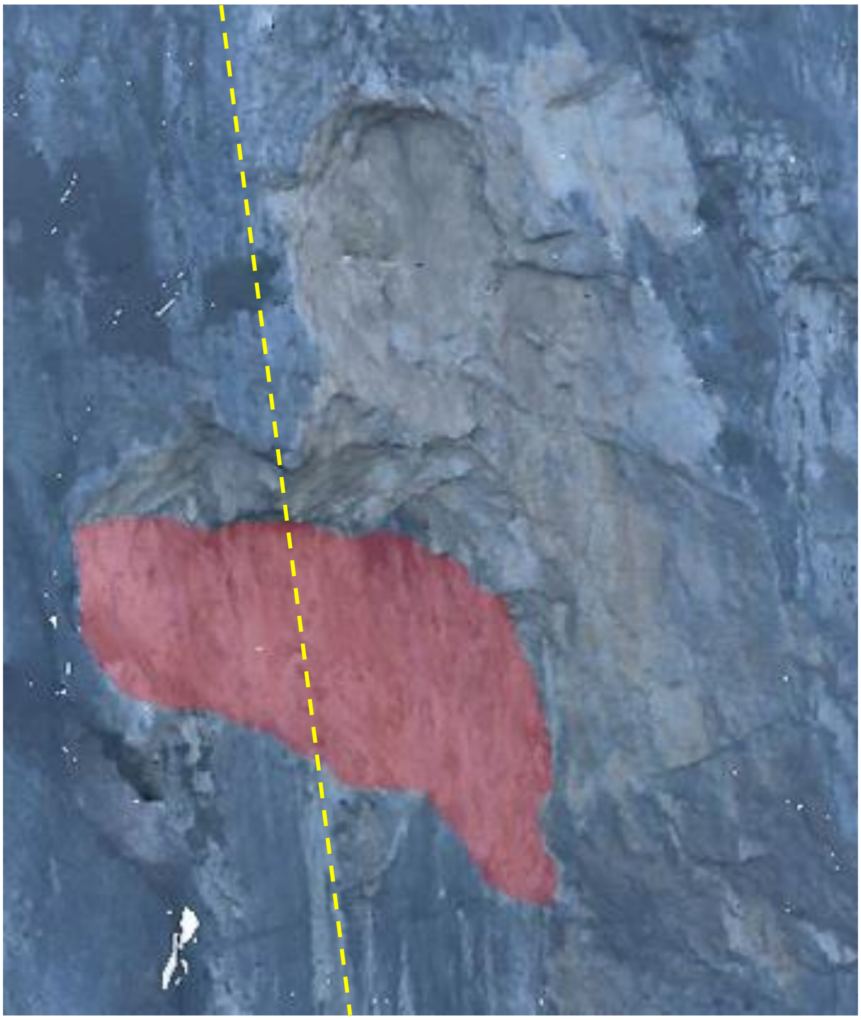

Figure 6: Detachment area of the rockfall (fresh out-breaks); the red polygon indicates the presumed failure plane; yellow dashed line marks the cross section used for the 2D computations in UDEC (see Chapter 3.2.4)

3.2.3 *Determination of the In-situ Block Size and Shape Distribution*

The theoretical in-situ block size and shape distribution, along with the predominant block orientation in jointed block model was simulated using 3DEC, a three-dimensional distinct element code by Itasca Consulting Group Inc. Therefore, a code provided by Söllner [29] and Aichinger [30] is adopted and modified in this work. In the code, the necessary joint characteristics, such as dip direction, dip angle, persistence, and spacing are derived from the previously conducted discontinuity mapping with JMX Analyst and are listed in Table 2. A cubic model with an edge length of 100 m x 100 m x 100 m is created, which represents the rock mass.

Table 2: Results from the Lambert Projection; SS= structure set, dd= dip direction of the projection plane, d= dip angle of the projection plane, n= number of joints, p= joint persistence, s= normal spacing, σ_s= standard deviation of the normal spacing

Set	dd [°]	d [°]	n	p [m]	s [m]	σ_s [m]	Origin
SS 01	173.5	87.1	88	1	2.3	13.4	0,0,0
SS 02	259.8	12.8	61	1	8.7	9.4	0,0,0
SS 03	248.6	89.7	52	1	11.4	18.8	0,0,0
SS 04	309.1	83.7	123	1	1.8	5.6	0,0,0

For the virtual model boundary, also blocks (Figure 7) have to be defined in order not to bias the results. This model boundary, located at the model margin, represents a fictitious, non-natural boundary. The blocks are smaller than the inner ones and border the mapping window. They have contact to free space in y- and z-direction, thus they are neglected in the analysis [31].

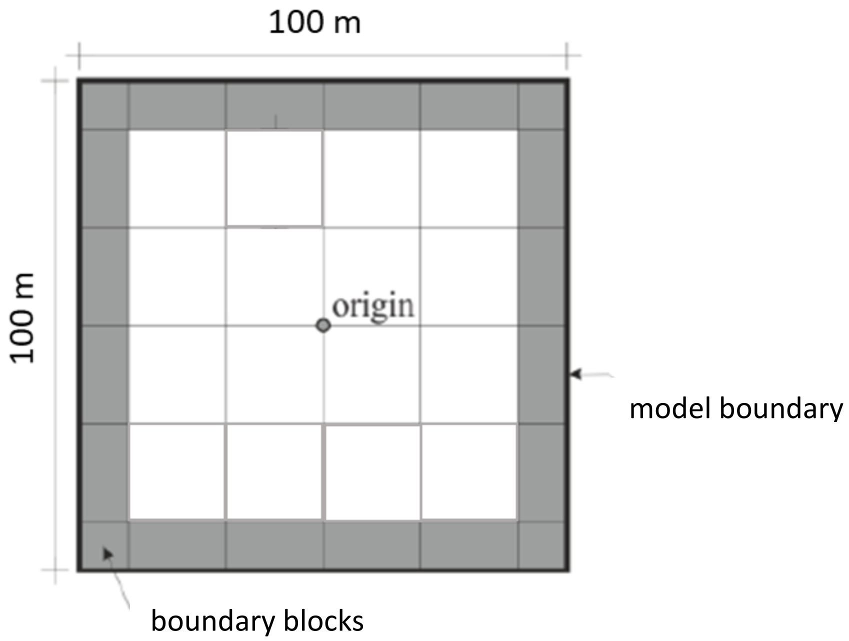

Figure 7: Schematic illustration of the boundary blocks (modified after Kluckner et al. [31])

In total, 50 replications are performed to achieve a statistical reliability due to the randomized joint spacings within the given standard deviation.

The classification of the block shape is based on the Block Shape Characterization Method [22,30]. The authors use two variables, which characterize the flatness (α; equation 1) and the elongation (β; equation 2) of a block and plot their results according to the accumulated density distribution (Figure 8). The results of the replications are plotted according to accumulated density distribution as well.

$$\alpha = \frac{A_s * l_{avg}}{7.7 * V} \quad 1$$

$$\beta = 10 * \left[\frac{\sum (a * b)^2}{\sum \left|\left|a\right|\right|^2 \left|\left|b\right|\right|^2} \right]^2 \quad 2$$

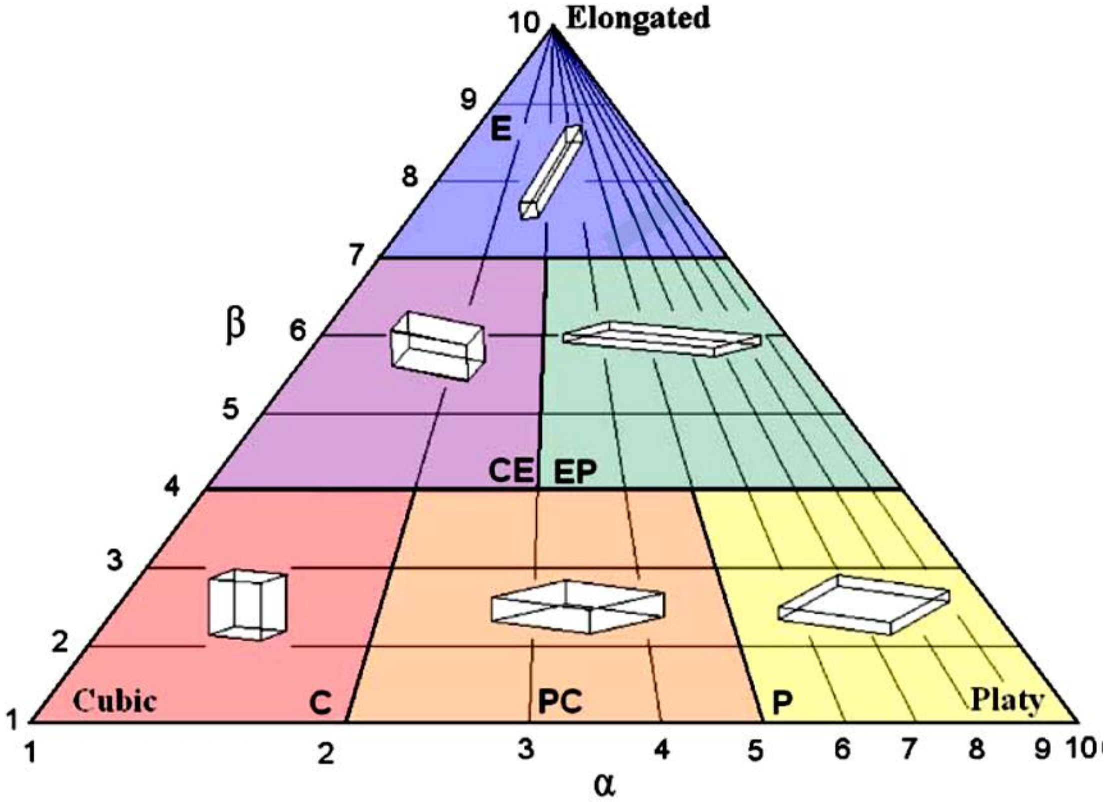

Figure 8: Block Shape Characterization after Kalenchuk et al.[22]; E= elongated, C= cubic, P= platy, CE= cubic-elongated, EP= elongated-platy, PC= platy-cubic

3.2.4 *Numerical Simulation of the Fragmentation Process*

The Universal Distinct Element Code (UDEC, Itasca Consulting Group Inc.) is a 2D numerical software, which can simulate the behaviour of a system responding to quasi-static or dynamic loading [32]. A discontinuous medium, such as the rock mass, is represented by an assemblage of discrete blocks. The corresponding discontinuities form the boundary conditions between blocks. As large displacements and rotational movements are expected to occur during the analysis, this program is sufficient for investigating the fragmentation process of the rockfall event.

In order to capture fast and large block displacements during the calculation process, it is possible to trace the movements of the blocks. This dynamic process depends on the predefined physical properties of the system. The characteristics of motion are represented numerically by a time stepping algorithm where the size of the time step is based on the assumption that velocities and accelerations are constant within a time step. As a consequence, the time steps between two iterations have to be as small as possible, otherwise the contact of a falling block on the surface might not be detected. The time step restriction, which in fact states the limited speed at which information can be transmitted in a physical medium, applies in both contacts and blocks. Blocks can either be rigid or deformable (zoned). Hence, for rigid blocks and the interface stiffness between blocks determine the time step limitation; for deformable blocks, the zone size defines the stiffness of the system including both the intact rock modulus and the stiffness of the contacts [33].

The basic assumption is a pre-fractured block, held together by the joint properties (jkn, jks, tensile strength and c) acting like intact rock bridges. Figure 9 shows the basic mechanical model, which defines contacts and joint stiffness properties implemented in UDEC.

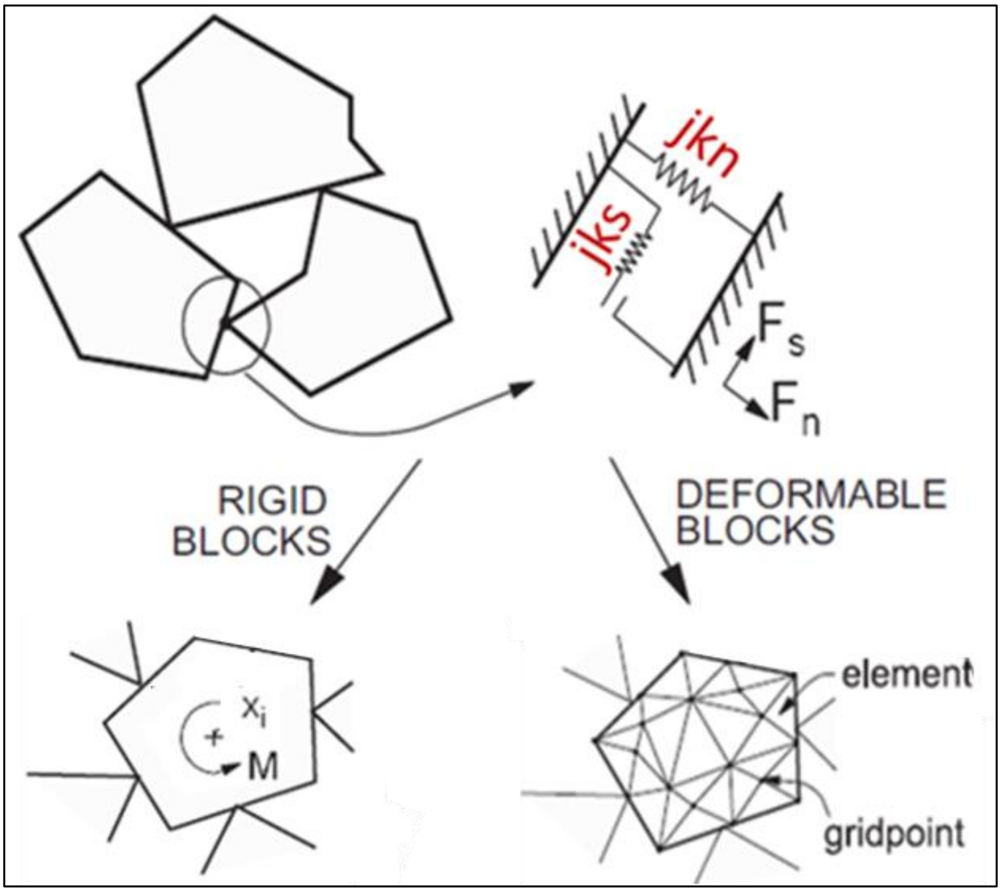

Figure 9: Calculation cycle of a dynamic process for a DEM for both rigid and deformable blocks [33]; with: jkn = joint normal stiffness [Pa/m], jks = joint shear stiffness [Pa/m], F = force [N], xi = coordinate of block centroid, M = moment acting on the block

The setup of the model comprises of three code parts, where the overall conditions (contact properties of falling blocks, gravity force, coefficient of rebound as the ratio of the height of bounce to the height of drop, and the fraction value [33]), geometry and material of the slope and modelled block are specified. To define the block properties, an isotropic-elastic model was selected. For the joint characteristics the constitutive model of Coulomb-Slip is used. To model the energy dissipation of a falling block during an impact with the solid rock wall, a damping parameter is used. It defines the energy absorption during a dynamic analysis. In the investigations, the default value of 0.8 is used throughout all computations, as modifications showed no influence on the results. Furthermore, for the simulations a fraction value of 1E-2 is used.

Initially, intact rock conditions are simulated using higher values for stiffness parameters, and cohesion. The values for jkn and jks were constantly reduced in order to observe their influence of disaggregation on the simulation. Additionally, the value for cohesion is set to zero in the lowest and highest jks- modification in a jkn- calculation cycle. More precisely, c assumed to be zero when jkn = 1E11 Pa/m and jks = 1E5 Pa/m or jks = 1E11 Pa/m, jkn = 1E12 Pa/m and jks = 1E5 Pa/m or jks = 1E12 Pa/m, and jkn = 1E13 Pa/m and jks = 1E5 Pa/m or jks = 1E13 Pa/m. For the joint normal stiffness values from 1E11 Pa/m to 1E12 Pa/m and for the joint shear stiffness values between 1E5 Pa/m and 1E13 Pa/m were presumed. It is assumed that the value of the joint shear stiffness does not exceed the value of the joint normal stiffness. So, if on the one hand, the joint normal stiffness is less than 1E11 Pa/m, the modelled rigid blocks overlap. On the other hand, if the value for the shear stiffness is less than 1E5 Pa/m, the disaggregation arises before the first impact. For upper limits of both joint normal and joint shear stiffness, 1E13 Pa/m is chosen because higher values may be unrealistic for this problem [34]. In the modelling process, jkn and jks are modified in the range to the power of 10. For the UCS a value of 70 MPa is assumed. The value was chosen due to the tectonized limestone in the investigation site. Assuming 30° for the internal friction, the cohesion of 2E7 Pa could be approximated using equation 3. The tensile strength is, according to the rule of thumb $^{1}/_{10}$ of the UCS, which reveals 7E6 Pa.

$$UCS = 2 * c * \tan\left(45 + \frac{\varphi}{2}\right) \qquad 3$$

Initially, the block geometry is oversimplified in order to understand the fragmentation process of the rockfall. Therefore, the joint stiffness parameters are frequently modified to approximate a realistic behaviour. The focus of the fragmentation modelling is on the simulation of the bouncing of a block, which is fitted to the geometry of the detachment area. Note that the shape of that "fitted" block bases on empirical estimations, resulting from visual inspection of the slope morphology in the cross section. In Figure 10 is the setup of the model depicted.

In all calculations, the rock slope remains rigid (not zoned). However, for the model type, three initial conditions for the internal structure are assumed:

- A zoned/deformable block based on an isotropic-elastic zoned model [35] in order to determine the position of the predefined cracks (Figure 11: a)
- A fractured, rigid block with cracks (Figure 11: b), having the same orientation as SS 02 (dip angle 12°) and SS 04 (dip angle 80°, see Table 2)
- Combination of a zoned and cracked model

Figure 10: Fitted block with joints (red circle)

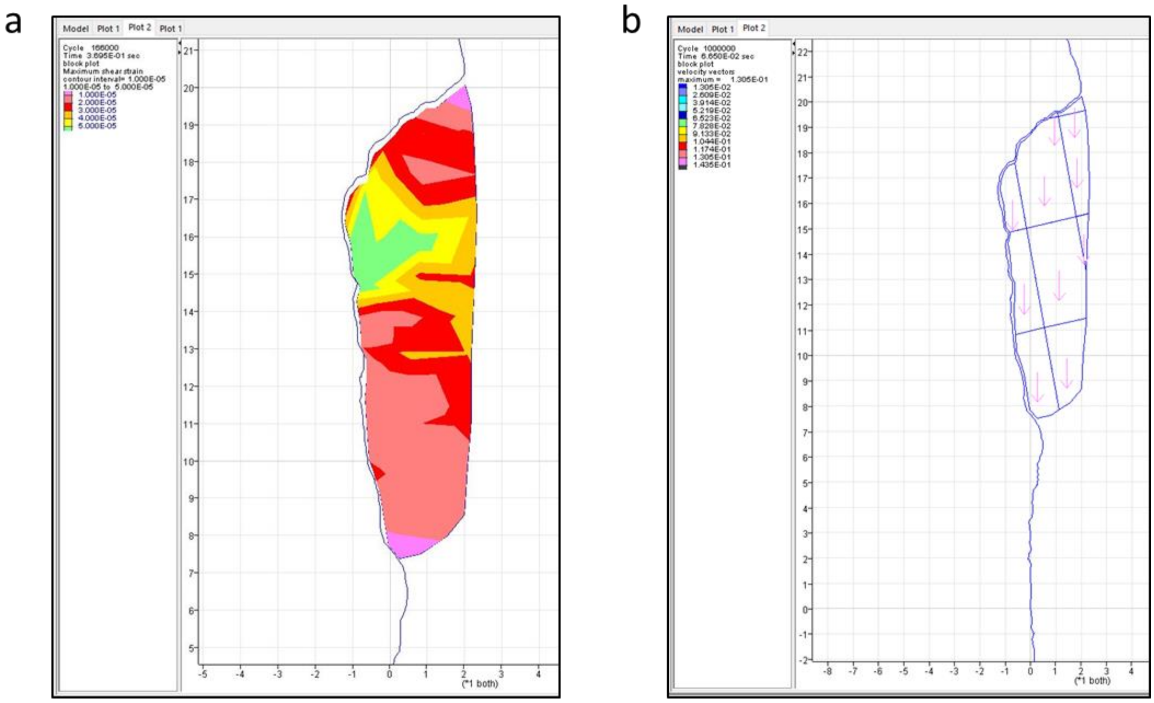

Figure 11: Model setup; a: maximum shear strain at the first impact defines the position of future cracks, b: model block with joints before the first impact (pink arrows indicate direction and magnitude of the velocity of the rigid blocks)

Table 3 displays the initial model parameters for the fitted block model. With the values for the joint normal and joint shear stiffness as well as the joint cohesion being unknown, a sensitivity analysis was performed.

*Table 3: Initial material parameters of the model with the fitted block; * [36]; ^ $^{1}/_{10}$ of UCS = 70 MPa; #marks minimum values which are adjusted and modified*

Parameter	Variable	Value
Bulk modulus* [Pa]	K	6.5E10
Shear modulus* [Pa]	G	2.4E10
Density* [g/m³]	rho	2.7E3
Joint normal stiffness# [Pa/m]	jkn	1E11
Joint shear stiffness# [Pa]	jks	1E5
Friction angle* [°]	phi	30
Cohesion# [Pa]	c	2E7
Tensile strength^* [Pa]	ten	7E6

Furthermore, the E_{pot} of blocks from the detachment area was estimated in order to assess maximum available energy amount for fragmentation. In theory, a certain proportion of E_{pot} is used for the fragmentation, while the rest is transferred to the transport of the fragments [37]. Therefore, equation 4 and the values from Table 4 are used.

$$E_{pot} = m * g * h \quad (4)$$

Table 4: Values for the calculation of E_{pot}

Parameter	Variable	Value
Mass [kg]	m	1,431,270
acceleration of gravity [N/kg]	g	9.81
total height [m]	h	75

4 Results

4.1 Residual Block Size and Block Shape Distribution

In total, 62 blocks were measured during the field work. The analysis of the block size distribution in the field showed that most measured blocks have an average volume of 3.8 m^3. The added-up volume of the measured blocks is 235.7 m^3. In Table 5, the results of block size analysis are presented. In the Appendix, all results of the measured block axes from the field work are shown.

Table 5: Calculations of the residual block size distribution in the accumulation area

Parameter	Value
Number of measurements	62
V_{total} [m^3]	235.72
$\overline{V}$ [m^3]	3.80
$\overline{\sigma}$ [m^3]	4.10
$V_{0.25}$ [m^3]	0.69
$V_{0.5}$ [m^3]	1.15
$V_{0.75}$ [m^3]	3.38
V_{max} [m^3]	62.16
V_{min} [m^3]	0.23

Figure 12 illustrates the results of the analysis of the block shape distribution in the accumulation area of the deposit (RBSD). The analysis reveals that most of the blocks are cubic to slightly columnar shaped.

The cumulative block size distribution (Figure 13) of the measured blocks show a scattered pattern due to low amount of measurements in the field.

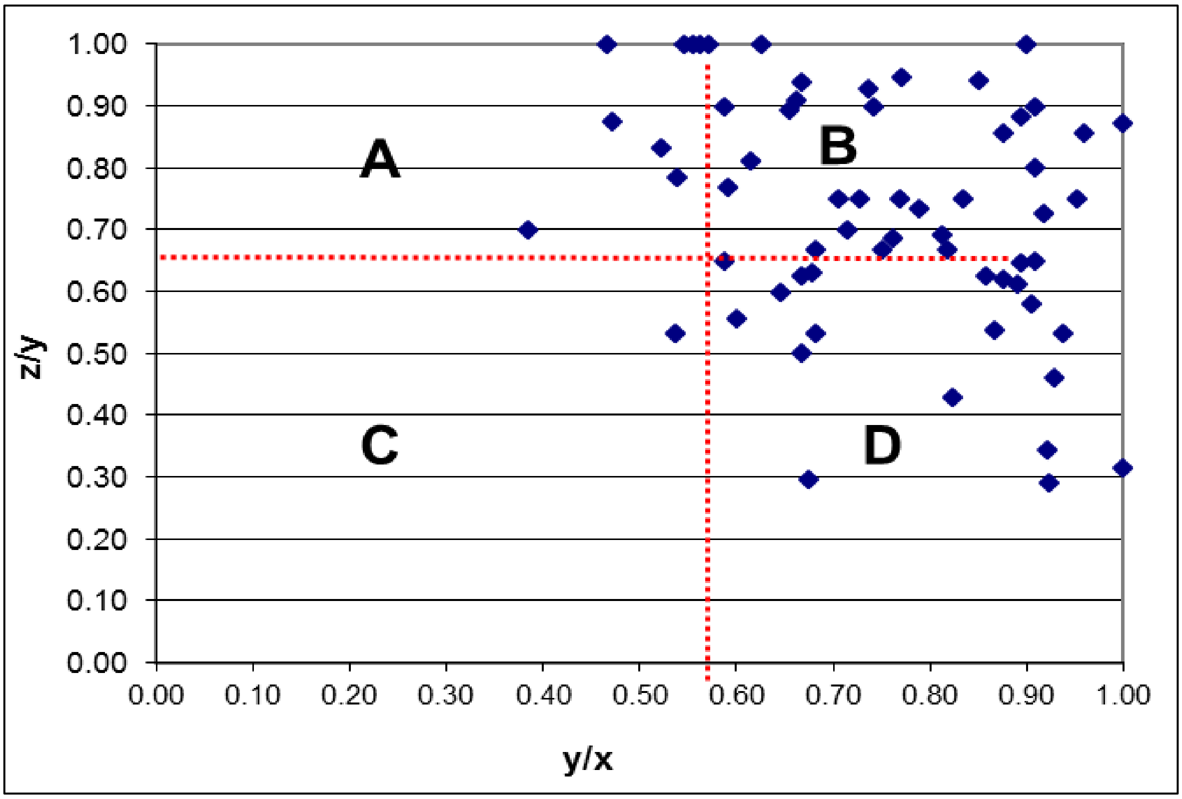

Figure 12: Block shape distribution in the accumulation area; with: A= tabular, B= cubic, C= prismatic, D= columnar; abscissa shows the ratio of middle to longest block axis, ordinate displays the ratio of shortest to middle block axis

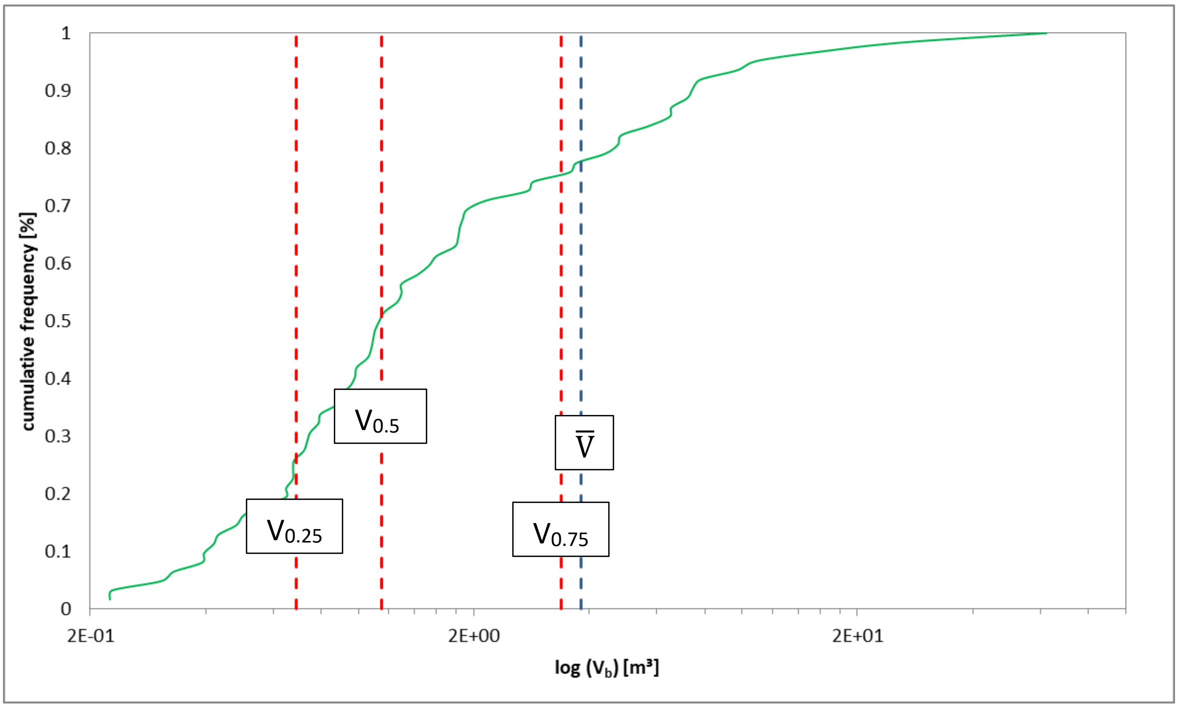

Figure 13: Cumulative block size distribution of the measured blocks in the rockfall deposit (green line); with $V_{0.25}$ = 0.69 m³, $V_{0.5}$ = 1.15 m³, $V_{0.75}$ = 3.38 m³ (red dashed lines); $\bar{V}$ = 3.80 m³ (blue dashed line)

4.2 Mapping of the Discontinuities with JMX Analyst

The resolution of the DSM is most accurate for mapping in the central region. Thus, discontinuities in the peripheral areas, are not mapped. The resulting mean values and standard deviations of the joint orientations (Figure 14) are shown in Table 6. Additionally, all orientation measurements are listed in the Appendix. Figure 15 shows all discontinuities, which are illustrated and clustered according to their orientations. Moreover, the volume of the detached rock fall event is approximated with 530.1 m³.

Table 6: Mean orientations of the structure sets; SS= structure set, $\overline{dd}$= mean dip direction, $\bar{d}$= mean dip angle, sa= spherical aperture, cc= cone of confidence; NoM = number of measurements.

Set	$\overline{\mathbf{dd}}$ [°]	$\bar{\mathbf{d}}$ [°]	sa [°]	cc [°]	NoM
SS 01	190	79	20.3	3.9	88
SS 02	222	27	26.6	6.1	61
SS 03	173	74	24.9	6.2	52
SS 04	267	77	20.1	3.2	123

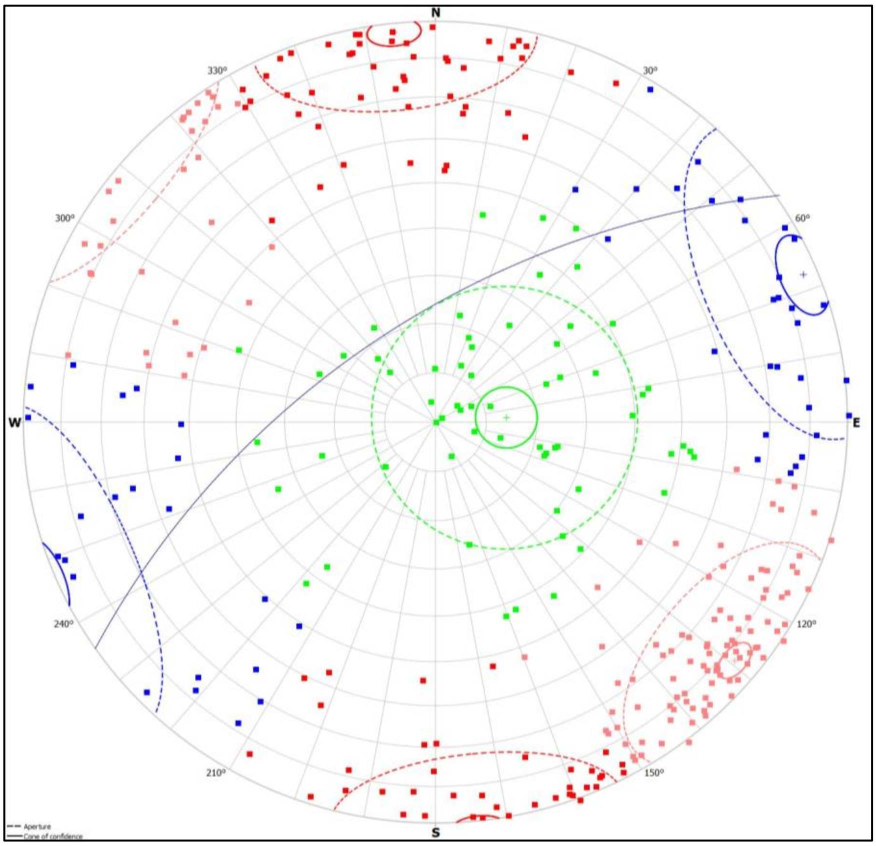

Figure 14: Lambert projection of the mapped discontinuities in JMX Analyst; the black great circle indicates the mean orientation of the slope; the discontinuity sets are plotted with the corresponding cones of confidence (straight line) and angular apertures (dashed line); SS 01= red, SS 02= green, SS 03= blue, SS 04= pink.

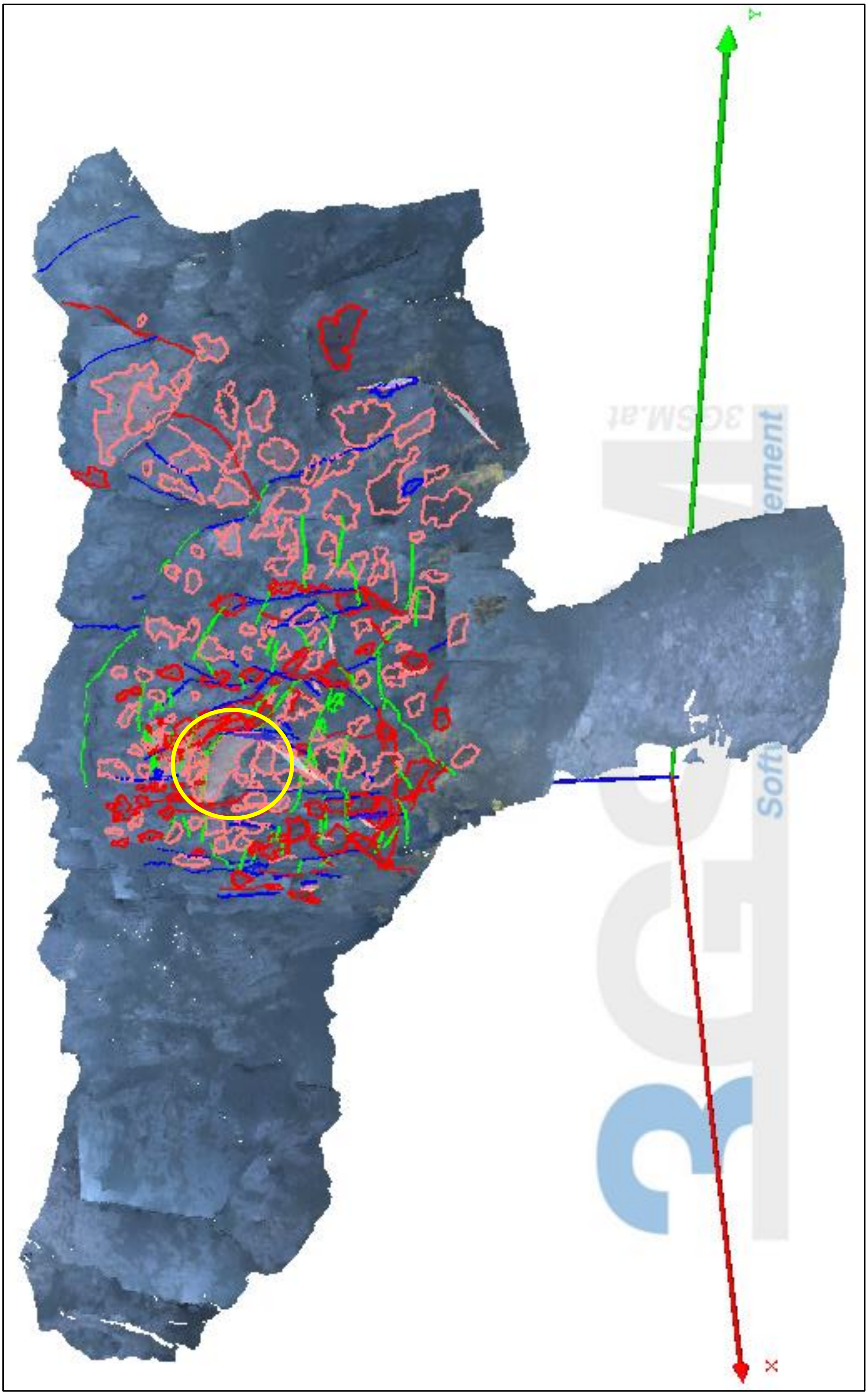

Figure 15: Mapped and clustered discontinuities in the rock wall; SS 01= red, SS 02= green, SS 03= blue, SS 04= pink; yellow circle indicates the position of the detaching block

4.3 Kinematic and Risk Analyses

4.3.1 *Failure Mechanisms in the Rock Wall*

In order to test which failure mechanism is common in the investigation area, all mechanisms are considered. For a better visualization, solely the mean set planes of the SS are displayed in the figures below (Figure 16). The analysis considering wedge sliding and direct toppling show additionally the critical intersections with the set planes, which are indicated as red bordered dots in the marked sections. In total, 13605 intersections of the mapped discontinuities are possible.

The analyses indicate the greatest probability of failure for wedge sliding (b; 12 %) and flexural toppling, which triggers interlayer slipping (d; 8 %). Planar sliding (a; 4 %) and direct toppling (c; 3 %) are less common. Moreover, according to the analyses, oblique toppling, which is a special case of direct toppling, seems also probable (10 %).

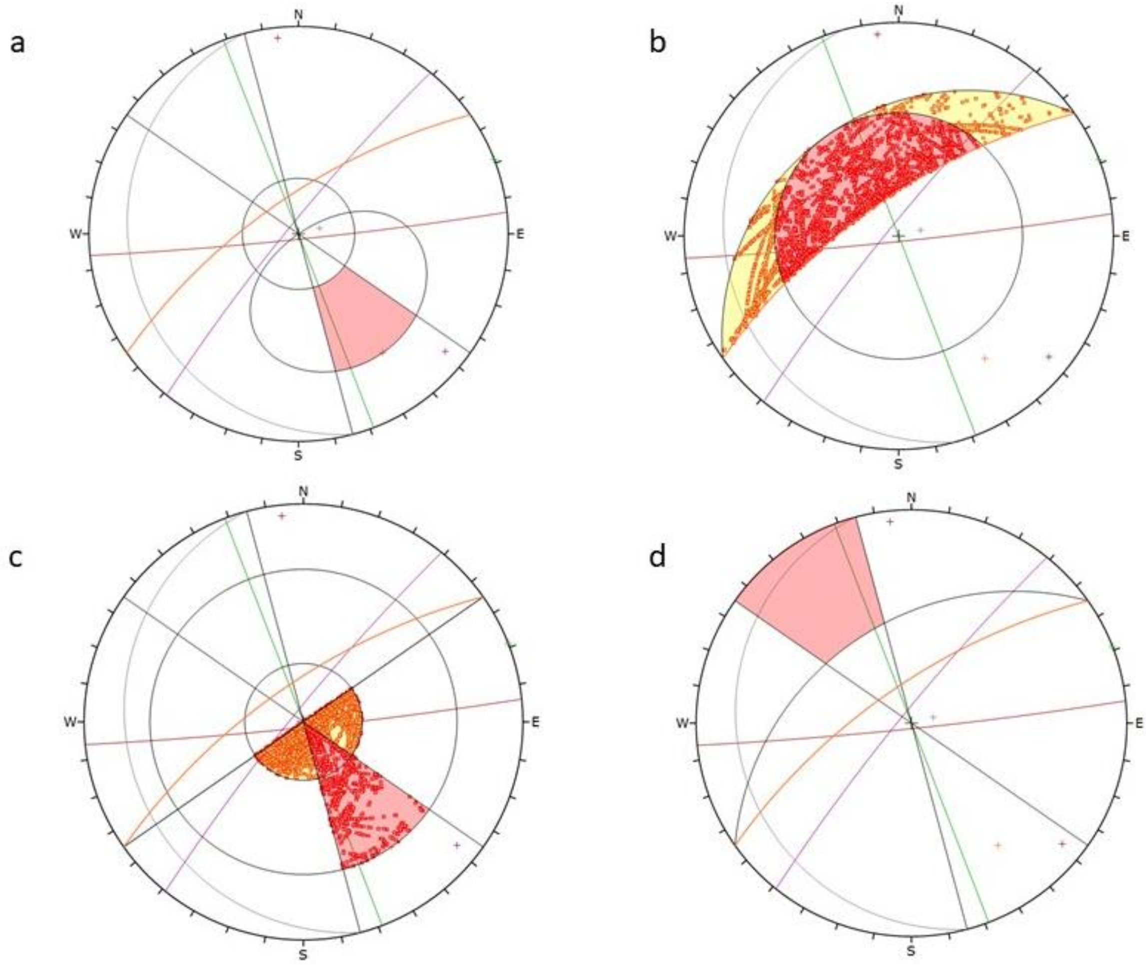

Figure 16: Kinematic analyses of the rock mass considering planar sliding (a), wedge sliding (b), direct (c) and flexural toppling (d)

4.3.2 *Failure Mechanism in the Detachment Area*

Using the orientation data of the discontinuities within the detachment area, the kinematic analysis indicates that the failure mode of the detachment area is also a combination of the already mentioned mechanisms (Figure 17). Assuming a planar failing surface (Figure 6) about 10 % of the 39 mapped discontinuities in the detachment area show a favourable orientation for planar sliding. All of them belong to structure set 04. For flexural toppling, 20.5 % of the mapped discontinuities could contribute to a failure. Direct toppling and wedge sliding base on the analysis of intersections of all planes (grid data planes), which is 527 for this analysis. For wedge sliding about 27 % of the intersections form a wedge that may slide on the line of intersection or on one plane having a favourable orientation. According to the analysis, direct toppling is less common (6.8 %). Subordinately, the kinematic analysis of direct toppling also considers oblique toppling (critical intersections: 8.9 %) and failure on a base plane (critical intersections: 12.8 %).

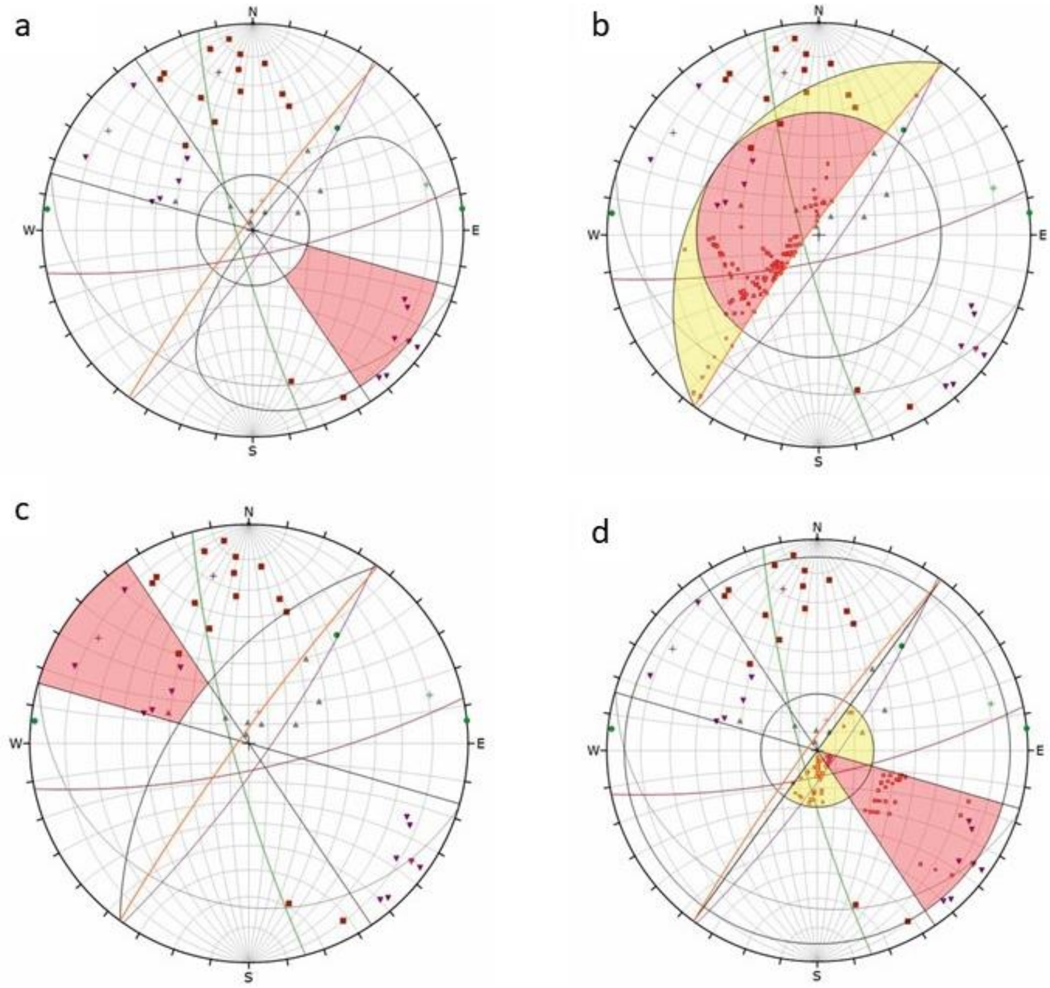

Figure 17: Results of the analysis of the detachment area with planar sliding (a), wedge sliding (b), direct (c) and flexural toppling (d)

4.3.3 *Risk Analysis of the Rock Cliff*

The areas highlighted in Figure 18 may pose a higher risk for failure than elsewhere in the cliff due to the aspects mentioned in chapter 3.2.2.

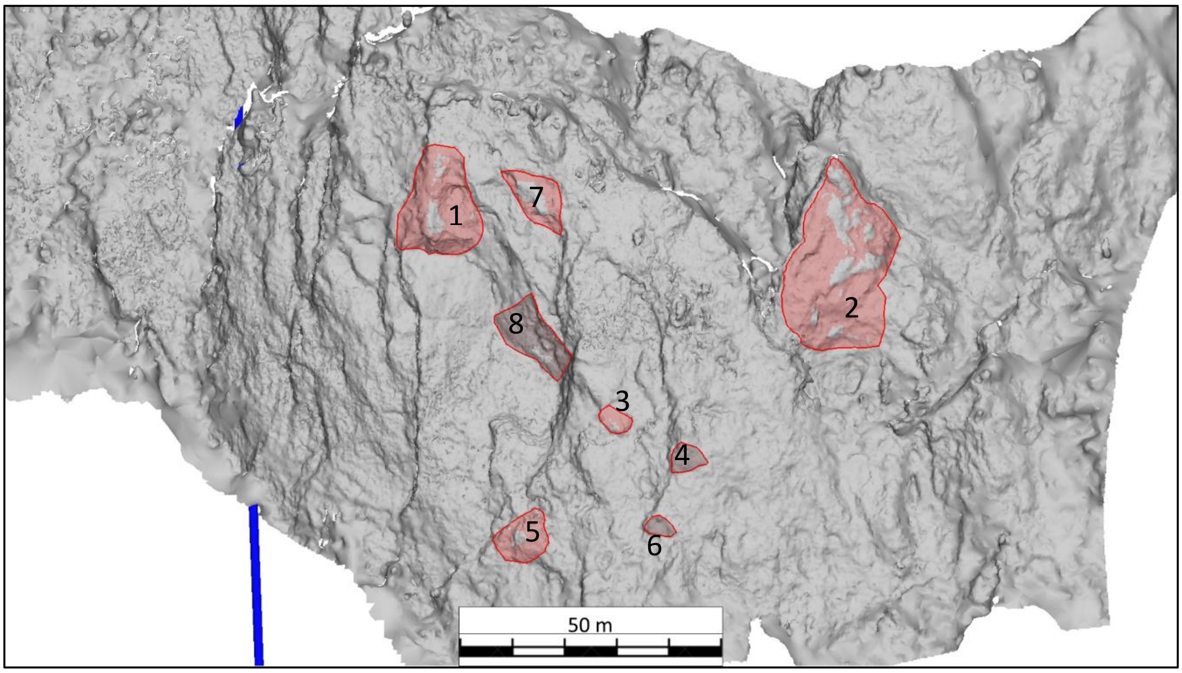

Figure 18: Risk map of the investigation site; red areas mark zones of potential failures

In Table 7, the characteristics of the areas at risk are described and explained.

Table 7: Description of the areas mapped in the risk analysis.

ID	Description
1	Distinct intersection of joints; SS 01/04; overhang; outbreaks visible
2	Younger outbreaks visible; appropriate orientation of joint sets for failure; SS 01/04; zone for potential failures mapped, probably not the whole marked block will fail
3	Slightly overhanging topography; plate-like detachment of blocks; sliding on SS 04
4	Slightly overhanging topography; smaller outbreaks visible; SS 01/04
5	Very small outbreaks; overhang; SS 01/02/04
6	Small, younger outbreaks; overhang; SS 02/04
7	Compare with 6
8	Clear overhanging topography; small, younger outbreaks; intersection of SS 01/04

4.4 Determination of the in-situ Block Size and Shape Distribution

According to 3DEC, most blocks are elongated (Figure 19). In Figure 20, the density plot (a), which is defined by the two geometric factors α and β [22,30], and the orientation of the longest block axis (b) are displayed. The density plot also reveals elongated blocks shapes. The orientation of the main block axis is more or less vertical and parallel to the cliff face.

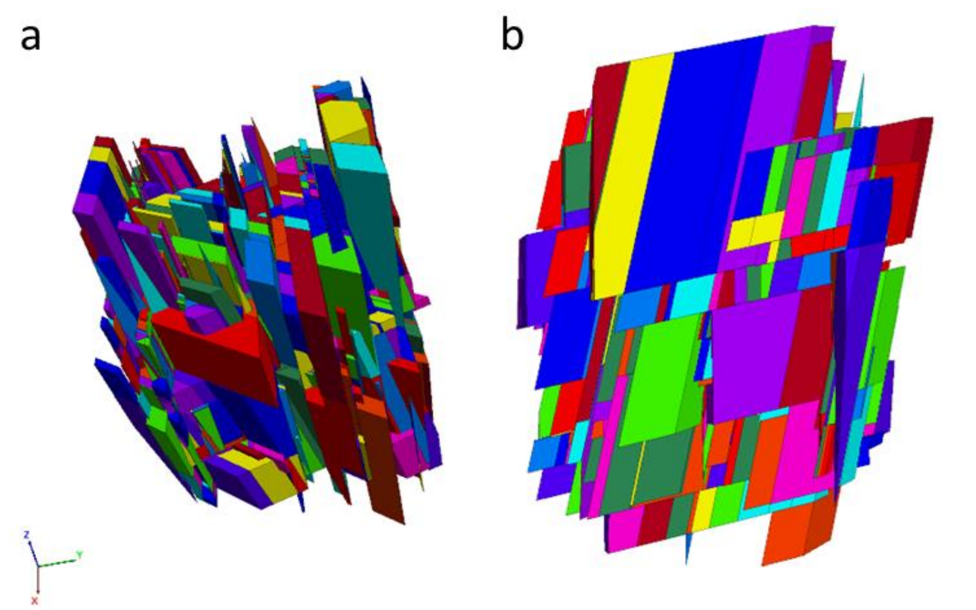

Figure 19: Examples of the BSD at the first permutation (a: top view, b: side view)

Figure 21 shows the cumulative IBSD of rock cliff. The difference of the results for the IBSD are within a relatively wide range (note, the abscissa is in a logarithmic scale), which results from the implemented standard deviation of the spacing. In Table 8 are the results of the IBSD computation, including their standard deviation, displayed.

Table 8: Results of the in-situ block size distribution

Parameter	Value
$\bar{V}$ [m³]	31.43
$V_{0.25}$ [m³]	1.45
$V_{0.5}$ [m³]	7.65
$V_{0.75}$ [m³]	30.64

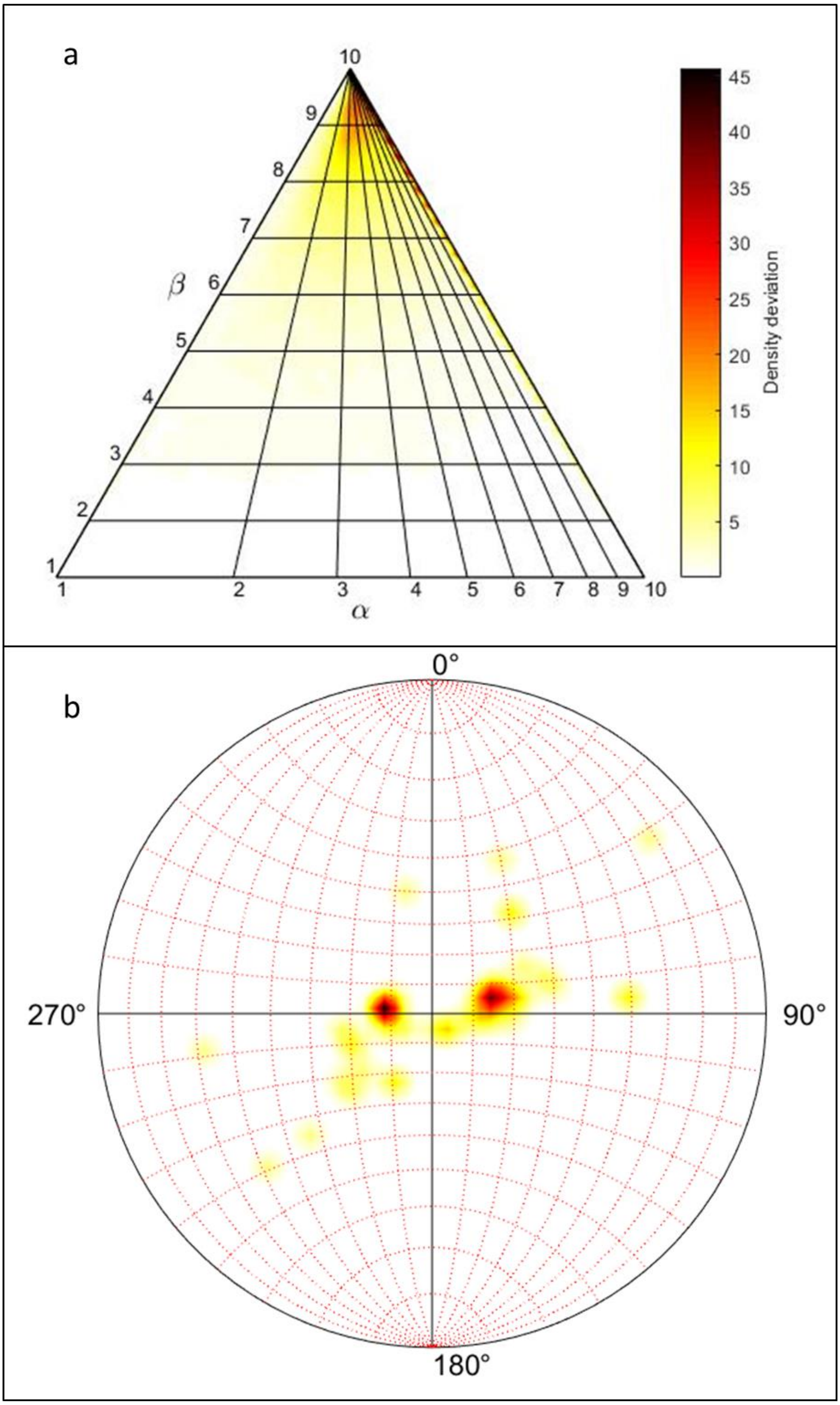

Figure 20: Results of the BSD computation with 3DEC after 50 replications; a: density plot, b: orientation of the main axis of the blocks

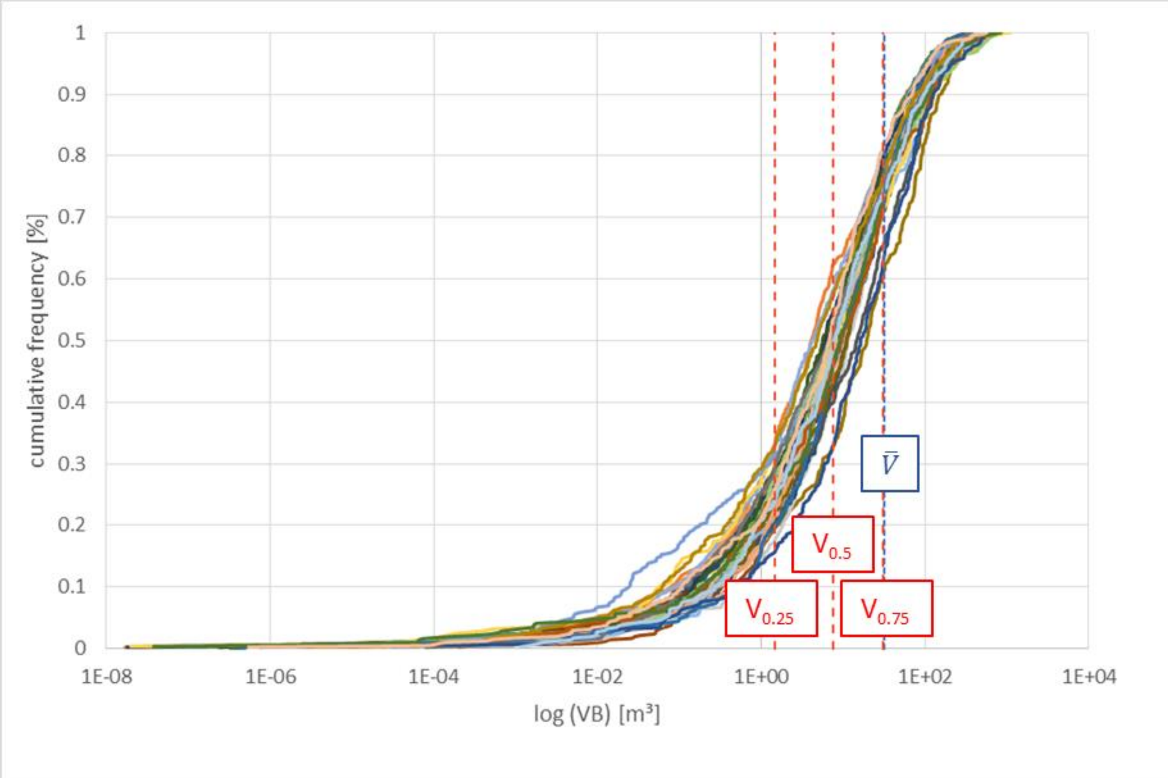

Figure 21: Cumulative distribution of the block size of 50 replications; $\bar{V}$ = 31.43 m^3, $V_{0.25}$ = 1.45 m^3, $V_{0.50}$ = 7.65 m^3, $V_{0.75}$ = 30.64 m^3

4.5 Numerical Simulation of the Fragmentation Process

The theoretical height of the rockfall (75 m) results in an E_{pot} of 105 MJ for the whole block (parameter see Table 4). However, as the slope is not planar, but has protrusions and is slightly inclined, the block will bounce several times on its way down. Since the model is not georeferenced, the elevation data is only relative and here referred as the model elevation which reflects the model range in the y-direction. Observing the block, the free fall is about 0.4 m (from model elevation 15.1 to 14.7 m) before its first impact.

In Table 9 the results of the first impact of jkn 1E11 Pa/m, 1E12 Pa/m, 1E13 Pa/m and the corresponding lowest and highest jks- and c-modifications of the rigid blocks are presented. The plots, which display the velocity vectors, demonstrate the behaviour of the rigid blocks and are shown in the Appendix. Furthermore, in Table 10 the maximum shear strain of the first impact with varying jkn, jks and c, as mentioned before, are presented. The corresponding plots reveal the internal behaviour of the block, such as the development of potential and new shear bands along which displacement and failure could occur. The results of all modifications are illustrated in the Appendix.

Table 9: Results of the modifications of jkn, jks and c at the first impact of the rigid block

jkn [Pa/m]	jks [Pa/m]	c [Pa]	velocity [m/s]
1E13	1E13	2E7	8.164E-2
1E13	1E13	0	1.394E-1
1E13	1E5	2E7	4.990E-1
1E13	1E5	0	7.250E-1
1E12	1E12	2E7	1.728E-2
1E12	1E12	0	3.716E-1
1E12	1E5	2E7	4.534E-1
1E12	1E5	0	5.315E-1
1E11	1E11	2E7	2.236E-1
1E11	1E11	0	1.387E0
1E11	1E5	2E7	6.476E-1
1E11	1E5	0	1.492E0

Table 10: Results of the modifications of jkn, jks and c at the first impact of the zoned-meshed block

jkn [Pa/m]	jks [Pa/m]	c [Pa]	maximum shear strain [-]
1E13	1E13	2E7	5.000E-6
1E13	1E13	0	9.000E-6
1E13	1E5	2E7	6.000E-6
1E13	1E5	0	3.500E-6
1E12	1E12	2E7	5.000E-6
1E12	1E12	0	7.000E-6
1E12	1E5	2E7	7.000E-6
1E12	1E5	0	2.500E-6
1E11	1E11	2E7	7.000E-6
1E11	1E11	0	6.000E-6
1E11	1E5	2E7	6.000E-6
1E11	1E5	0	4.000E-6

5 Discussion

5.1 Mapping of the Discontinuities with JMX Analyst

Discontinuity mapping using remote sensing techniques is already widely established in geotechnical mapping [23], because it is fast, objective and could minimize the risk for the mapping geologist. The results derived from the point cloud data, such as the orientation of the discontinuities, as well as the spacings and the corresponding standard deviations are often basis for further analysis and modelling.

The DSM, used for this thesis, is created from images taken from a distance of up to 1,150 m, which reduced the resolution and accuracy of the DSM. This, and the chaotic orientation of the discontinuities resulting from tectonic stress, may cause the problem of identifying the major joint set pattern. Nevertheless, the automatic k-means clustering algorithm in SMX was not able to properly solve this problem because of the relatively high tolerance of the confidence level (95 %). Therefore, some outliners had to be allocated manually.

Besides the fact that the resolution is reduced in the outer part and manual allocation of some clustered discontinuities, following statements can be made:

- Discontinuities belonging to SS 04 are subparallel to the slope surface and are preferentially affected by potential failures (chapter 5.2).
- SS 02 is most important considering the difference in BSD in the rock wall and the accumulation area of the rockfall as well as the IBSD and RBSD (chapter 5.3).

5.2 Kinematic and Risk Analyses

For the reconstruction of the failure mechanism during the rockfall event and also for potential future events, various modes have to be considered. The kinematic analyses base on geometric operations in the Lambert azimuthal projection. In this consideration, overhanging cliffs cannot be taken into account, although this kind of morphology plays an important role for failures in steep rock walls [28]. However, the focus of these analyses is on the intersections of discontinuities and the orientation of discontinuities with reference to the slope.

In chapter 4.3.1, there are the probabilities of the various failures mentioned. These probabilities indicate the percentage of critical intersections of the mapped discontinuities. Favourable intersections may pose a higher risk for potential failures, but more important is, whether joints are persistent, rock bridges exist, or asperities on the sliding planes prevent blocks from sliding.

Considering the investigated failure modes available in Dips 7.0, every one of them reveals specific characteristics. The probability of planar sliding is, compared to other failure mechanisms, relatively low (about 4 %). This means that parts of the rock wall could be more favourable for planar sliding, especially when discontinuities insect the cliff face and fulfil the criteria for planar failure [20,25,38]. Therefore, a more detailed analysis is required which would go beyond the scope of this thesis. Furthermore, wedge failure is relatively common according to the analysis (about 12 % of all intersections are accounted for being critical). The chaotic orientation of the discontinuities favours the probability of forming wedges. Also, the results of the analysis concerning direct (3 % of probability of failure) and flexural toppling (8 %) have to be regarded critically. In literature [25,26], both modes act similarly, with only direct toppling requiring, additionally to the two joint sets which form an intersection line that dips into the slope, a third joint set of near horizontal planes that act as release planes for discrete blocks. Flexural toppling, which is most common in steeply inclined, thin- bedded rocks, which does not apply for the investigation site. The analysis considering flexural toppling indicates that SS 01 and SS 04 are most likely to be affected. The analysis concerning direct toppling is more complex. It can be split into direct and oblique toppling, and toppling on the basal plane which is represented by the poles depicting the release planes that act also as sliding plane [24]. SS 02 and SS 04 act as base planes for the direct toppling mode.

The rock wall in the investigation site is tectonically heavily disturbed and a bedding of the limestone layers is not well-pronounced. Thus, the probabilities of flexural and direct toppling do not sufficiently depict the real conditions of susceptibility, although the geometric conditions for failure may be satisfied. Also, for planar and wedge sliding the kinematic analysis of the whole rock wall is too imprecise. Nevertheless, it helps to roughly estimate what kind of failures are possible and with which probability they may occur.

In contrast to the large-scale investigation of a whole rock wall, the kinematic analysis of the detachment area is more valid. Chapter 4.3.2 shows that different failure mechanisms are probable for the rock fall event depending on the orientation of the various surfaces within the detachment area. However, as one plane seems to act as the failing surface of the rockfall, planar sliding seems to be the dominant failure mechanism of this event. However, due to the steep inclination of the plane (> 80°), it is termed to be rather a falling mode [39,40]. Structure set 04 is most susceptible for failure in all types of mechanisms, which dips more or less parallel to the slope.

As mentioned in chapter 3.2.2 , the intersection of discontinuities and the local morphology of the slope play an important role for risk assessment. However, it is very important to consider the identification of zones at higher risk based on visual inspections of the DSM. Thus, real properties and conditions of discontinuities, such as seepage, persistence and shear resistance of the failure plane, cannot be determined. The risk analysis provides only estimations of zones at higher susceptibility for failure, which may not necessarily occur in the near future or even in the highlighted areas.

5.3 Comparison of the BSD and the Correlation of the RBSD with the IBSD

There is a significant difference of the observed BSD in the accumulation area of the rockfall event and the modelled results with 3DEC.The predominant geometry in the deposit in the field is rather cubic (see chapter 4.1), whereas the blocks modelled in 3DEC reveal an elongated geometry (see chapter 4.3.3). The different shapes can be explained as follows:

- Due to the high potential energy (app. 105 MJ) of the detaching material, much of it can be contributed to the fragmentation. The dominantly cubic shaped RBSD had probably exceeded the tensile strength of elongated rock blocks due to high bending moments impacting at the ground. Elongated blocks tend to break in the middle of the longest axis, where the bending moment increases the formation of high gradients in local stress distribution concentration [41]. The bending moment affects both the deformation and ultimate fracturing of the blocks.

Furthermore, there is also a difference in the modelled IBSD and observed RBSD. Following aspects can explain that:

- In 3DEC, a persistence of 1.0 is assumed. This causes the modelled block size distribution to be smaller than in the actual rock wall. Thus, the persistence value, which is probably overestimated, underrepresents the block size.
- Visual discontinuity mapping may not sufficiently cover all structures which exist in the joint network. Consequently, the determined spacing resulting from the

discontinuity mapping may be too big. As shown in Table 2, the standard deviation of the spacings are higher, than the mean values themselves. Especially for SS 02, which cuts the blocks in the rock wall sub-horizontally, its insufficient representation becomes obvious in the 3DEC model. It is expected to cut the elongated blocks horizontally, which would result in more cubic shaped blocks, with about half of their size. Thus, the spacing resulting from the discontinuity mapping may cause an overrepresentation of the block size distribution in the rock wall. Hence, the computed blocks are not as jointed as the natural state might be.

- Comparing the average RBSD in the deposit (3.8 m^3) with the mean value of the modelled IBSD (31.43 m^3) reveal a significant difference. The reason for this, is the potential energy of the detaching rock mass that causes fragmentation of the blocks. As well as the above-mentioned draw backs.
- Considering the total volume of the rockfall (530.1 m^3) with the total volume of the measured blocks in the deposit (235.7 m^3), about 44 % of the material must have turned into fragments smaller 0.2 m^3, which was assumed to be the lower threshold for this thesis or are concealed due to burial by other fragments.

Combining the first two perspectives, it can be possible that their influence on the IBSD is cancelled out.

Ruiz-Carulla et al. [11] stated that the difference of the theoretical IBSD and the observed RBSD result mainly from breakage of the fragments as they disaggregated. This process could also be obtained in the results of this study (Figure 22).

After all, the correlation of the theoretical IBSD and the observed RBSD could not be proved to be useful because no exponents for a power of law could be derived.

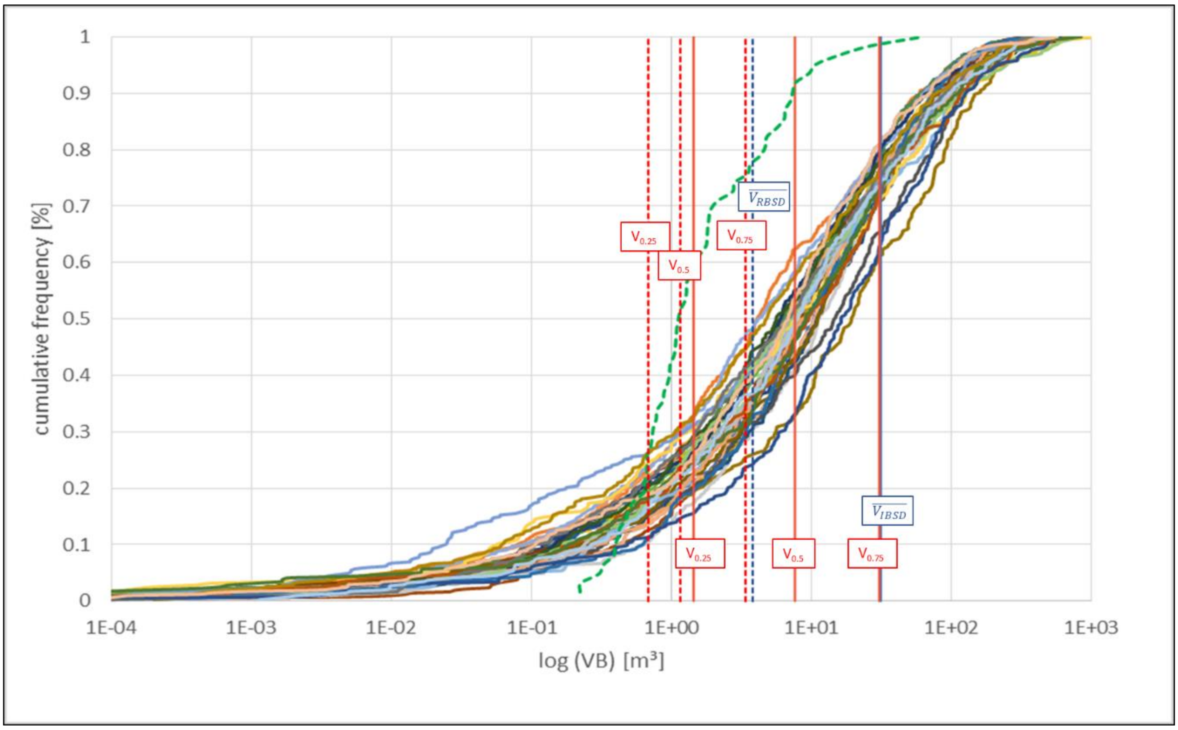

Figure 22: Correlation of the theoretical IBSD (full lines; with $V_{0.25}$ = 1.45 m³, $V_{0.5}$ = 7.65 m³, $V_{0.75}$ = 30.64 m³, $\overline{V_{IBSD}}$ = 31.43 m³) and observed RBSD (dotted lines; with $V_{0.25}$ = 0.69 m³, $V_{0.5}$ = 1.15 m³, $V_{0.75}$ = 3.38 m³, $\overline{V_{RBSD}}$ = 3.80 m³)

5.4 Numerical Simulation of the Fragmentation Process

The aim of the fragmentation model is to approximate a realistic fragmentation process. However, the model needed predefined cracks in order to create rigid blocks. The spacing of the joints of SS 02 and SS 04 which are introduced in chapter 4.5 might be too large. Also new cracks cannot be implemented during the fracturing/rock fall process simulated with UDEC and hence real fracturing cannot be modelled. Nevertheless, with reducing the joint shear and normal stiffness parameters and the cohesion in the joints, the disaggregation at the first impact and the influence of the parameters could be investigated.

Table 9 and Table 10 in chapter 4.5 (and the figures in the Appendix) show the influence of modifying the stiffness parameters and reducing the cohesion. The analyses reveal that jkn influences predominantly the stress propagation in normal direction. The higher jkn, the less energy is conducted into the blocks. The jks influences the disaggregation of the cracked blocks. The lower jks, the more likely is the disaggregation at the first impact. Also the reduction of c causes early disaggregation. According to the analysis, jks has a maximum value of 1E12 Pa/m while c was assumed with 2E7 Pa. If the cohesion was set to zero, disintegration already occurred at jks of 1E13 Pa/m.

The combined model with the zoned-jointed block was initially set up in order to identify further potential cracks because of the formation of new shear bands within the block. However, it turned out that the cracks do not propagate the energy but create rigid, zoned blocks where the energy is transferred to its borders. So once the block started to disaggregate, the stress concentrates in zones, where the fragments press against each other. As already mentioned, the predefined cracks determine where the block will disintegrate. Thus, no further fragments could be generated and therefore the only considered mechanism in the fragmentation modelling is disaggregation without breakage [11]. Anyway, the energy of the first impact is too low for a breakage of the fragments.

6 Conclusion & Outlook

Base of this thesis are investigations in the field, such as mapping of the residual block size distribution in the accumulation area of the rockfall and acquisition of data for the DSM. Four, heavy scattered joint sets are identified, where one of those is subparallel to the rock cliff. By means of both data records, parameters, such as the block size and shape distribution in the deposit, the orientation and spacing of the discontinuities in the rock cliff are used to generate numerical models. Furthermore, these data are used to correlate the IBSD and BSD, resulting from 3DEC, and fragmentation behaviour in the UDEC model, respectively, with the natural state.

The kinematic analysis of the rock wall enables the identification of further areas with an higher potential for risk. Furthermore, the kinematic analysis of the detachment area revealed planar sliding as the possible failure mechanism of the investigated rockfall event. The IBSD is computed with 3DEC, using the mean set orientations and spacings with the corresponding standard deviation of all structure set resulting from the discontinuity mapping. The simulations reveal a dominance of elongated BSD and a mean IBSD of 31.43 m^3. This does not correspond to the observed cubic shaped block and an average RBSD of 3.80 m^3 in the deposit. The divergence of the BSD could be explained by exceedance of the bending moment of the elongated block, which also causes fragmentation. Considering the difference in block size distribution, other reasons could be the overestimation of the theoretical persistence, insufficiently mapped discontinuities in the DSM and the transformation of the IBSD into the RBSD due to fragmentation caused by the relatively high potential energy of the rockfall. In literature [11,42] a plausible explanation of the connection between the IBSD and RBSD is formulated by fitting power laws and defining exponents. As the results of the transformation of the theoretical IBSD into the observed RBSD do not correspond well in this study, a more detailed investigation of the accumulation area in the field is suggested.

UDEC is used to model the fragmentation process at the example of the detaching block. Therefore, the spacing and orientation of SS 02 and SS 04 are used to crack the detaching block in the model. The modification of the input parameters, such as joint normal stiffness, joint shear stiffness and cohesion, indicate a major influence on the disintegration at the first impact. The most significant influence showed the reduction of the jks and c. The higher these values, the stronger the bounding between the rigid block fragments.

Generally spoken, as this thesis investigated only a theoretical approach, more research is needed to model the potential behaviour of a rockfall considering fragmentation during an event. Further work is recommended including studies on real materials and rockfall events, detailed investigations of energy distributions, lithologies, height of drop, ground surface rigidity and joint pattern.

7 References

[1] B. Chimani, G. Heinrich, M. Hofstätter et al., “ÖKS15 - Klimaszenarien für Österreich: Daten, Methoden und Klimaanalyse,” 2016.

[2] C. Bommer, M. Phillips, H.-R. Keusen et al., *Bauen im Permafrost*: *Ein Leitfaden für die Praxis*, Eidg. Forschungsanstalt für Wald, Schnee und Landschaft WSL, 2009.

[3] M. W. Bo, M. Fabius, and K. Fabius, “Impact of global warming on stability of natural slopes,” *Proceedings of the 4th Canadian Conference on Geohazards*, 2008.

[4] Statistik Austria, “Bevölkerung von Österreich 2007 bis 2017,” https://de.statista.com/statistik/daten/studie/19292/umfrage/gesamtbevoelkerung-in-oesterreich/.

[5] C. Zangler, C. Prager, R. Brandner et al., “Methodischer Leitfaden zur prozessorientierten Bearbeitung von Massenbewegungen,” *Geo. Alp*, vol. 5, 2008.

[6] Österreichische Gesellschaft für Geomechanik, “Empfehlung für das Schutzziel bei gravitativen Naturgefahren in Österreich,” 2014.

[7] GBA, “GBA MapViewer: Massenbewegungen in Österreich,” 11/7/2017, https://gisgba.geologie.ac.at/gbaviewer/?url=https://gisgba.geologie.ac.at/ArcGIS/rest/services/AT_GBA_MASSENBEWEGUNGEN/MapServer.

[8] Christchurch City Council, “Technical Guideline for Rockfall Protection Structures,” https://www.ccc.govt.nz/assets/Uploads/techguidelinerockfallprotectionstructures-mar2013.pdf.

[9] Bundesamt für Umwelt, *Schutz vor Massenbewegungsgefahren*: *BAFU*, 2016.

[10] Plattform Naturgefahren der Alpenkonvention, ed., *Dokumentation von Naturereignissen - Feldanleitung*, 2006.

[11] R. Ruiz-Carulla, J. Corominas, and O. Mavrouli, “A fractal fragmentation model for rockfalls,” *Landslides*, vol. 14, no. 3, pp. 875–889, 2017.

[12] J. T. Weidinger, “Das Gschliefgraben- Rutschgebiet am Traunsee- Ostufer (Gmunden/OÖ) - Ein Jahrtausende altes Spannungsfeld zwischen Mensch und Natur,” *Berichte Geol.B.-A.*, 2009.

[13] S. Prey, “Das Ultrahelvetikum-Fenster des Gschliefgrabens südöstlich von Gmunden (Oberösterreich),” *Jahrbuch Der Geologischen Bundesanstalt*, vol. 126, no. 1, pp. 95–

127, 1983.

[14] J. T. Weidinger and W. Vortisch, "Massenbewegungen im System Hart- auf- Weich zwischen Traunstein und Dachstein (OÖ, STMK) und ihre anthropogene Beeinflussung," 2005.

[15] G. W. Mandl, "Geologische Profilschnitte durch das Salzkammergut – vom Traunstein zum Dachstein (Ostalpen, Österreich)," GBA, 2017, https://opac.geologie.ac.at/wwwopacx/wwwopac.ashx?command=getcontent&server=images&value=ATA_2017_206.pdf.

[16] G. W. Mandl, "Vom Traunstein zum Dachstein – Geologie im Querschnitt," GBA, 2017, https://opac.geologie.ac.at/wwwopacx/wwwopac.ashx?command=getcontent&server=images&value=ATA_2017_022.pdf.

[17] O. Hausberger, *Petrophysikalische Charakterisierung der lithologischen Einheiten im Bereich der Massenbewegung im Gschliefgraben bei Gmunden (Oberösterreich),* Bachelor Thesis, Montanuniversität Leoben, 2012.

[18] B. Sellmeier, *Quantitative Parameterization and 3D-run-out Modelling of Rockfalls at Steep Limestone Cliffs in the Bavarian Alps*, Springer International Publishing, Cham, 2015.

[19] J. A. Franklin and M. B. Dusseault, *Rock engineering*, McGraw-Hill, New York, 1989.

[20] E. Hoek and E. T. Brown, "Practical Estimations of Rock Mass Strength," *International Journal of Rock Mechanics and Mining Sciences,* no. 34, pp. 1165–1186, 1997.

[21] J. V. Smith, "Determining the size and shape of blocks from linear sampling for geotechnical rock mass classification and assessment," *Journal of Structural Geology*, vol. 26, 6-7, pp. 1317–1339, 2004.

[22] K. S. Kalenchuk, M. S. Diederichs, and S. McKinnon, "Characterizing block geometry in jointed rockmasses," *International Journal of Rock Mechanics and Mining Sciences*, vol. 43, no. 8, pp. 1212–1225, 2006.

[23] 3GSM GmbH, "ShapeMetrix3D: User Manual JMX Analyst for ShapeMetrix3D," C:\Program Files\ShapeMetriX 3D\doc\en\analyst.html.

[24] Rocscience, "Dips: Kinematic Analysis Tutorial," https://www.rocscience.com/help/dips/webhelp/tutorials/Dips_Tutorials.htm.

[25] R. E. Goodman, ed., *Introduction to Rock Mechanics*, John Wiley & Sons, Inc, 1989.

[26] J. A. Hudson and J. P. Harrison, *Engineering Rock Mechanics*: *An Introduction to the Principles*, ELSEVIER SCIENCE, 1997.

[27] K. Terzaghi, "Stability of Steep Slopes on Hard Unweathered Rock," *Geotechnique*, vol. 12, pp. 251–263, 1962.

[28] B. Matasci, G. M. Stock, M. Jaboyedoff et al., "Assessing rockfall susceptibility in steep and overhanging slopes using three-dimensional analysis of failure mechanisms," *Landslides*, vol. 119, no. 2, p. 162, 2017.

[29] P. Söllner, *Determination of the In Situ Block Size Distribution as a Parameter for the Rock Mass Characterization Based on Measurements and Statistical Methods*, TU Graz, 2014.

[30] S. Aichinger, *Determination of the Block Size and Shape Distribution in a Quarry by Using Remote Sensing Techniques*, TU Graz, 2018.

[31] A. Kluckner, P. Söllner, W. Schubert et al., "Estimation of the in situ block size in jointed rock masses using three- dimensional block simulations and discontinuity measurements," International Symposium on Rock Mechanics, 2015.

[32] Itasca Consulting Group, "UDEC Version 5.2: 2D discrete element modeling (DEM) in jointed and blocky material," https://www.itascacg.com/software/udec.

[33] Itasca Consulting Group, "Theory and Background : The 2D Distinct Element Method," 2014.

[34] Itasca Consulting Group, "Example Applications : 12 : Blocks Bouncing down Slope," 2014.

[35] Itasca Consulting Group, "Constitutive Models : 1 : Block Constitutive Models," 2014.

[36] C. Onasch, "Some Useful Numbers," http://www.jsg.utexas.edu/tyzhu/files/Some-Useful-Numbers.pdf.

[37] A. Tiwari, "Coefficient Of Restitution: Definition, Explanation And Formula » Science ABC," https://www.scienceabc.com/pure-sciences/coefficient-of-restitution-definition-explanation-and-formula.html.

[38] E. Hoek and J. W. Bray, eds., *Rock Slope Engineering*: *Civil and mining*, Springer-Verlag, Berlin/Heidelberg, 2005.

[39] T. H. Erismann and G. Abele, "Dynamics of Rockslides and Rockfalls," *Springer-Verlag*, 2001.

[40] M. Entfellner, *Trennflächenkartierung mittels ShapeMetrix3D,* Bachelorarbeit, TU

Graz, Jänner 2016.

[41] D. P. Adhikary, A. V. Dyskin, and R. J. Jewell, “Numerical modelling of the flexural deformation of foliated rock slopes,” *International Journal of Rock Mechanics and Mining Sciences & Geomechanics Abstracts*, vol. 33, no. 6, pp. 595–606, 1996.

[42] R. Ruiz-Carulla, J. Corominas, and O. Mavrouli, “A methodology to obtain the block size distribution of fragmental rockfall deposits,” *Landslides*, vol. 12, no. 4, pp. 815–825, 2015.

Appendix

Measurements of the blocks in the accumulation area of the rockfall

date	GPS_ID	x [cm]	y [cm]	z [cm]	Volume [m³]
8/17/2017	60	110	100	80	0.9
		95	95	83	0.7
		83	55	50	0.2
		73	70	60	0.3
	61	120	105	90	1.1
		130	80	65	0.7
		95	75	55	0.4
		140	120	75	1.3
		140	100	70	1.0
		220	130	100	2.9
		170	100	90	1.5
	62	440	300	200	26.4
		310	200	120	7.4
		110	75	40	0.3
		480	370	350	62.2
		240	210	130	6.6
		165	120	90	1.8
	63	190	190	60	2.2
		170	80	70	1.0
		160	90	90	1.3
	64	110	98	60	0.6
		170	100	65	1.1
		210	190	110	4.4
		120	80	75	0.7
		110	100	90	1.0
		140	80	80	0.9
		260	100	70	1.8
		200	135	40	1.1
		220	180	120	4.8
	65	160	150	80	1.9
		150	70	70	0.7
		110	60	60	0.4
		95	70	65	0.4
		90	50	50	0.2
		130	120	35	0.5
		150	90	50	0.7
		140	130	60	1.1
		100	85	80	0.7
		130	70	55	0.5
	66	145	95	85	1.2

		190	170	110	3.6
		120	110	80	1.1
8/30/2017	67	210	160	110	3.7
		170	120	90	1.8
		160	130	90	1.9
		120	80	50	0.5
		180	120	60	1.3
		300	260	140	10.9
	68	170	140	60	1.4
		260	200	150	7.8
		160	100	100	1.6
		140	95	60	0.8
		140	75	40	0.4
		120	90	60	0.6
		105	100	75	0.8
	70	190	170	150	4.8
		230	120	100	2.8
		240	200	150	7.2
	71	200	180	180	6.5
		380	350	120	16.0
		220	200	130	5.7
		270	200	180	9.7

Clustered orientations of the discontinuities

Set	dip direction [°]	dip angle [°]
StructureSet 01		
	174	87
	332	85
	161	58
	142	55
	196	64
	149	81
	346	74
	184	78
	159	69
	174	76
	151	82
	173	86
	167	84
	176	81
	192	68
	175	69
	156	79
	181	53
	174	55
	336	86
	182	71
	341	88
	184	67
	156	74
	341	87
	167	84
	182	54
	191	86
	5	87
	29	83
	207	85
	179	89
	175	85
	200	83
	154	56
	348	52

	22	65
	27	60
	0	68
	3	54
	167	85
	2	87
	160	77
	18	88
	14	78
	2	69
	175	75
	23	57
	170	80
	346	87
	185	69
	336	86
	350	89
	339	81
	333	87
	154	86
	334	80
	8	82
	337	83
	169	89
	14	83
	182	80
	169	87
	353	82
	193	83
	1	75
	168	89
	174	88
	341	85
	358	82
	157	89
	167	73
	337	88
	354	88
	355	88
	187	86
	338	87
	4	81
	343	87
	193	87
	181	81
	159	89
	340	90

	192	87
	189	82
	352	86
	173	73
	150	86
StructureSet 02		
	259	12
	111	43
	138	18
	214	50
	236	5
	203	17
	295	31
	249	23
	138	14
	147	23
	200	13
	280	24
	199	19
	164	5
	248	26
	136	1
	282	13
	224	5
	177	11
	250	11
	341	42
	346	25
	240	8
	312	38
	281	24
	281	7
	213	12
	307	29
	285	22
	127	23
	338	7
	209	2
	267	39
	221	43
	261	42
	215	25
	192	44
	283	21
	235	29
	287	22

	232	33
	275	50
	251	33
	239	41
	191	23
	276	52
	260	43
	213	37
	277	48
	206	48
	37	37
	75	24
	51	13
	68	35
	114	26
	338	41
	84	36
	39	42
	313	34
	287	48
	327	42
StructureSet 03		
	249	89
	100	79
	97	63
	249	76
	277	53
	260	71
	276	67
	260	72
	264	90
	269	90
	242	88
	252	88
	67	86
	95	89
	272	81
	75	79
	277	76
	70	88
	91	90
	70	86
	246	80
	249	77
	240	87
	251	80

	275	78
	262	78
	272	68
	254	80
	95	66
	83	54
	78	65
	90	52
	77	69
	72	58
	267	79
	278	75
	219	65
	225	72
	47	87
	32	70
	233	82
	224	80
	48	86
	236	79
	230	76
	212	88
	44	51
	33	78
	36	64
	43	75
	34	51
	42	78
	222	52
	210	57
	255	59
StructureSet 04		
	309	84
	306	85
	294	77
	308	81
	306	88
	297	79
	318	87
	124	46
	106	53
	138	50
	109	50
	141	84
	320	86
	123	83

301	48
316	47
323	68
311	70
284	72
306	84
114	82
146	90
299	79
312	85
126	89
118	70
317	85
101	81
112	58
324	58
102	61
101	53
104	62
321	80
295	89
312	80
332	76
311	79
306	72
318	86
306	88
283	83
296	84
292	82
280	73
307	78
308	83
301	87
297	74
300	65
141	88
329	86
316	83
118	87
309	73
313	79
326	86
326	74
129	82
312	80
310	79

119	83
284	75
303	90
315	69
133	64
297	83
279	62
142	88
287	90
308	78
146	88
295	75
305	78
143	84
139	78
321	79
318	74
313	77
329	72
312	82
141	88
320	78
323	82
311	67
311	86
317	68
311	76
307	79
146	85
293	84
294	64
314	74
319	83
309	85
322	90
326	67
332	75
316	65
309	76
297	55
304	75
297	67
280	77
303	78
310	74
304	81
314	82

302	87
310	74
319	81
314	88
318	79
290	83
330	81
144	89
328	83

114	81
302	83
330	76
340	52
149	83
330	86
330	85

Zoned model showing the total stress, maximum shear strain and shear strain at the first and second impact of the model block

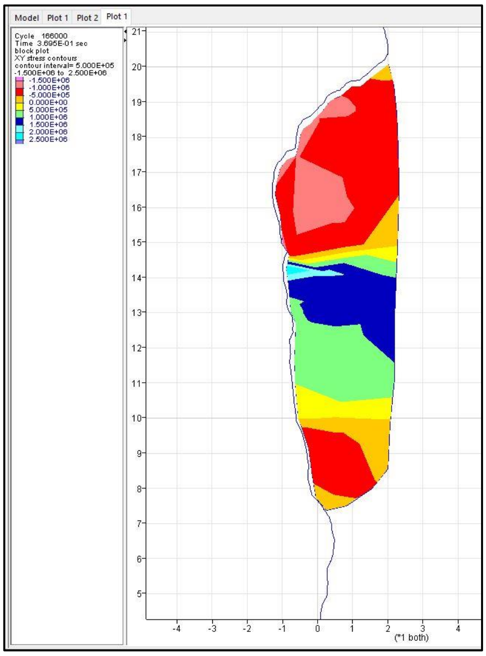

Fig. 1: first contact (step 1.66E5), total stress

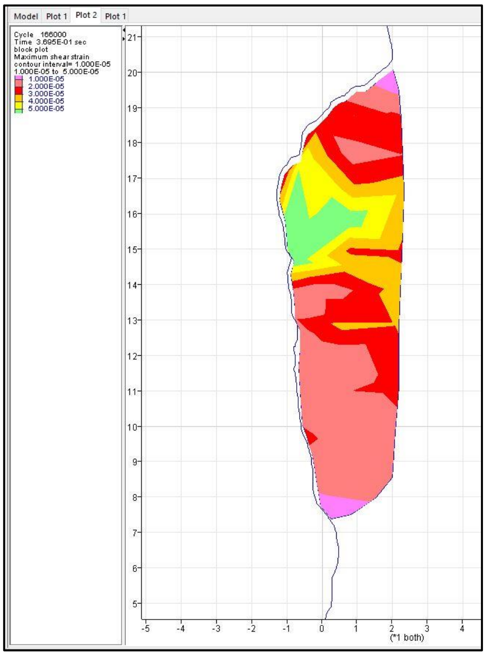

Fig. 2: first contact (step 1.66E5), maximum shear strain

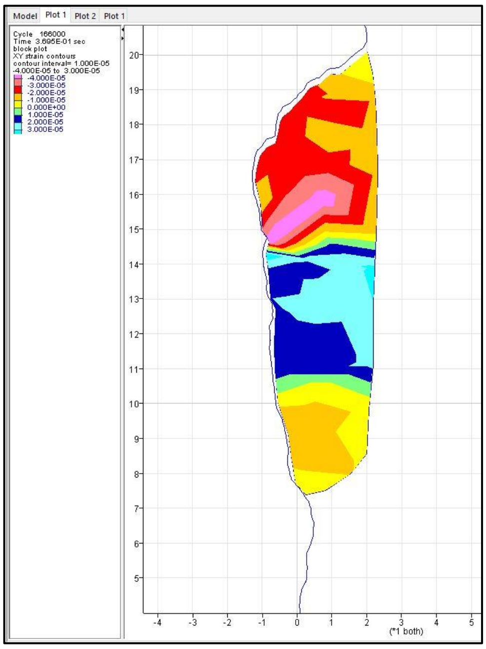

Fig. 3: first contact (step 1.66E5), shear strain

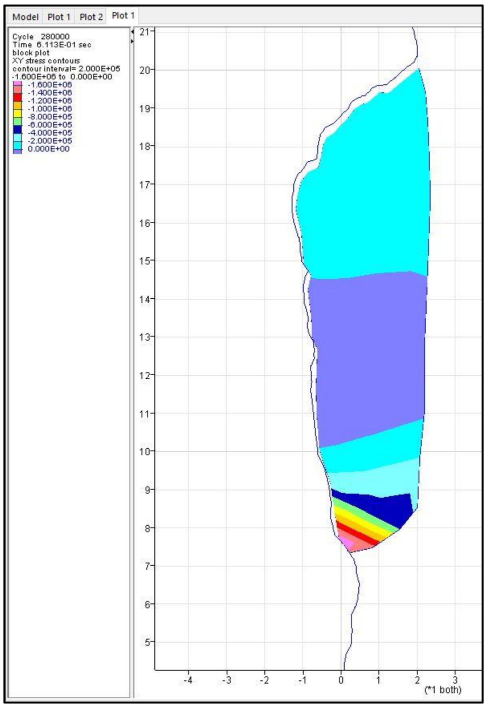

Fig. 4: second contact (step 2.8E5), total stress

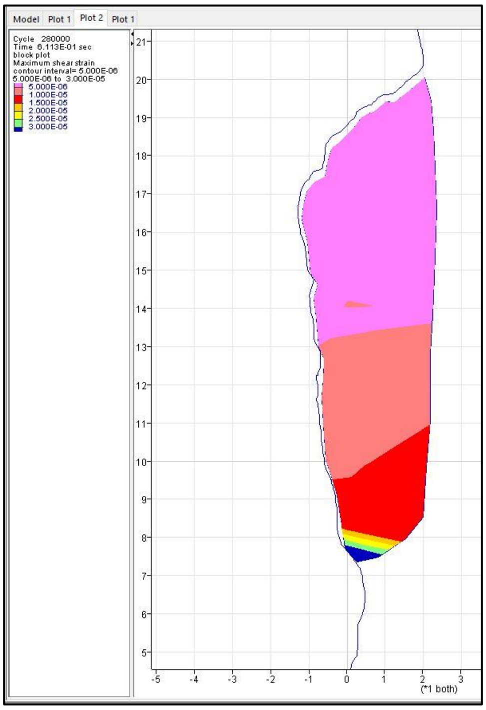

Fig. 5: second contact (step 2.8E5), maximum shear strain

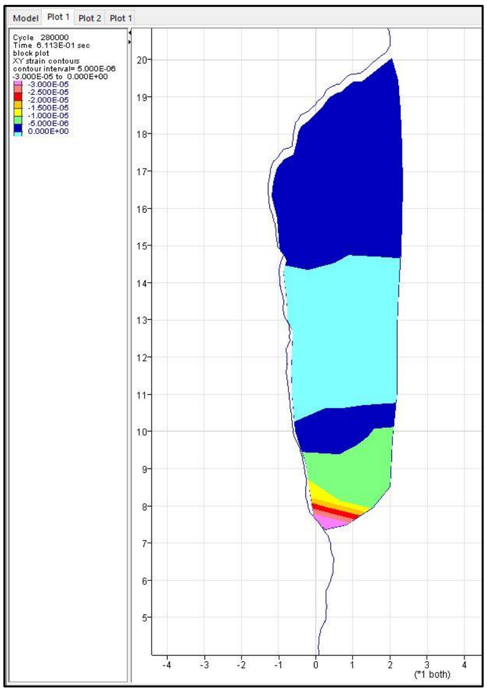

Fig. 6: second contact (step 2.8E5), shear strain

Cracked model showing the velocity trajectories of the rigid block with varying the parameters jkn [Pa/m] = 1E11, 1E12, 1E13, and jks [Pa/m] = 1E5, 1E6, 1E7, 1E8, 1E9, 1E10, 1E11, 1E12, 1E13, and c [Pa] = 2E7, 0 at different cycling steps and starting from the first impact

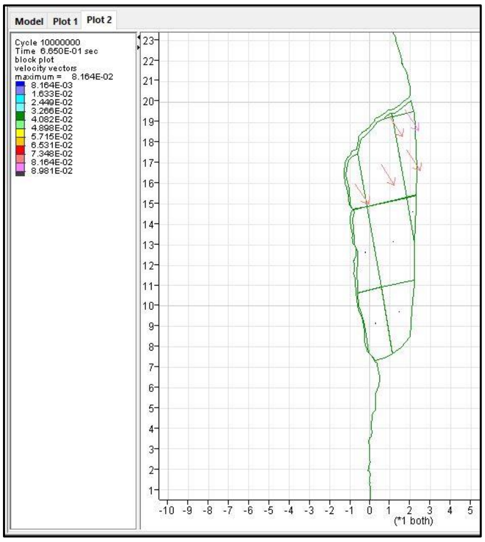

Fig. 7:, jkn = 1E13, jks = 1E13, c = 2E7, step 1E7

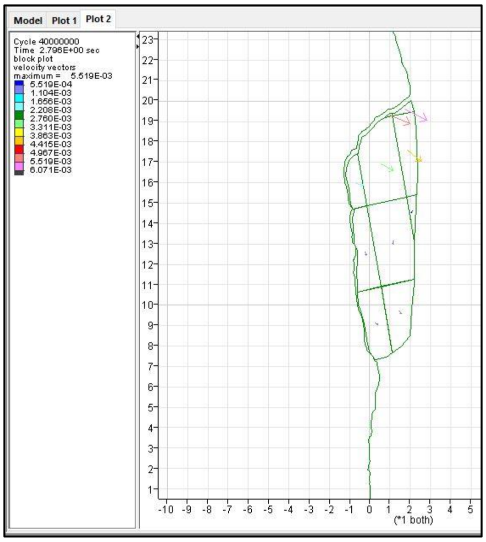

Fig. 8:, jkn = 1E13, jks = 1E13, c = 2E7, step 4E7

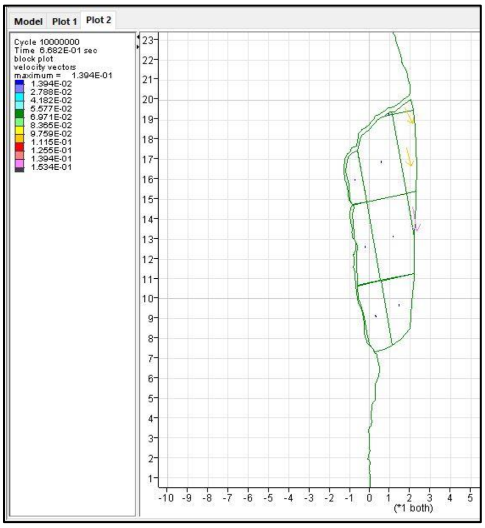

Fig. 9:, jkn = 1E13, jks = 1E13, c = 0, step 1E7

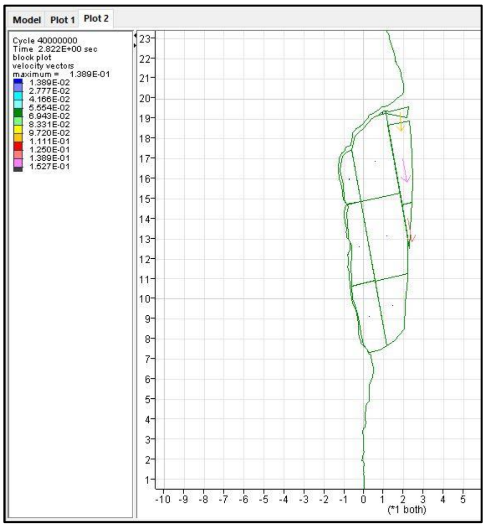

Fig. 10:, jkn = 1E13, jks = 1E13, c = 0, step 4E7

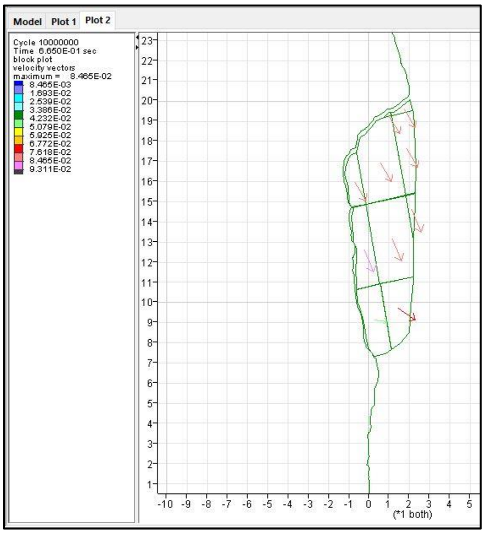

Fig. 11: jkn = 1E13, jks = 1E12, c = 2E7, step 1E7

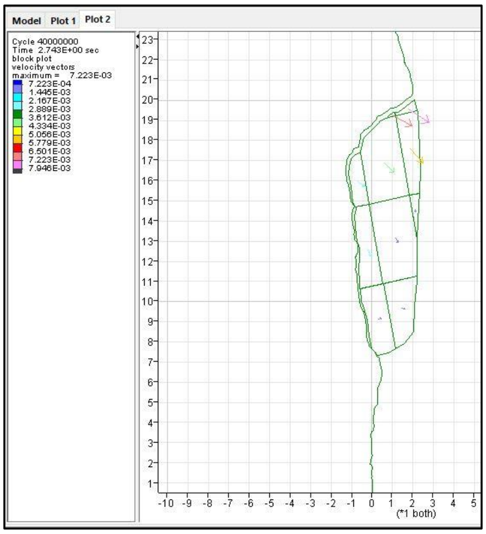

Fig. 12: jkn = 1E13, jks = 1E12, c = 2E7, step 4E7

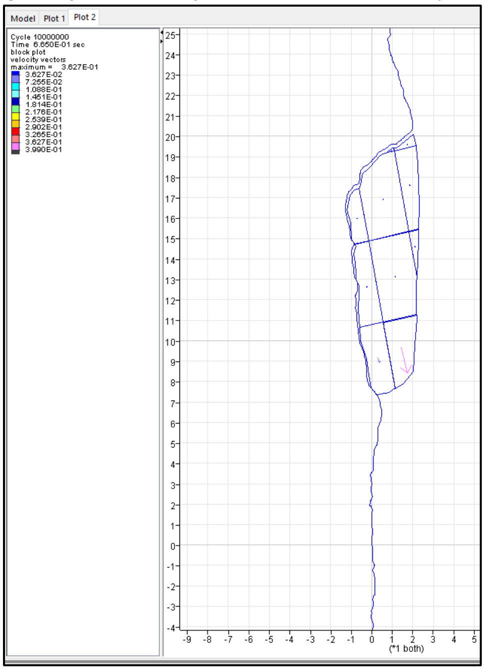

Fig. 13: jkn = 1E13, jks = 1E11, c = 2E7, step 1E7

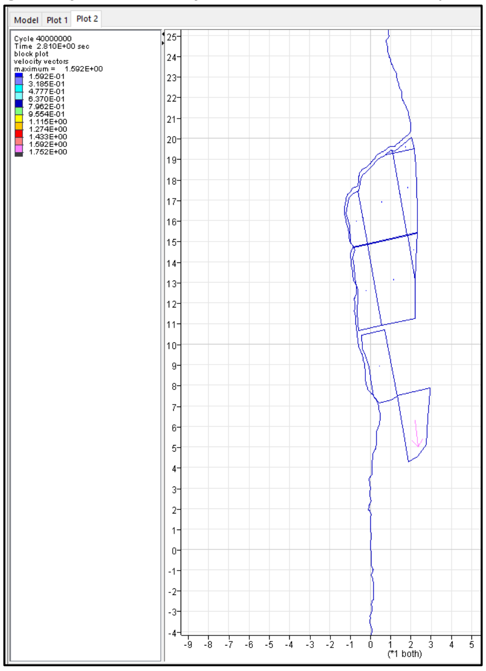

Fig. 14: jkn = 1E13, jks = 1E11, c = 2E7, step 4E7

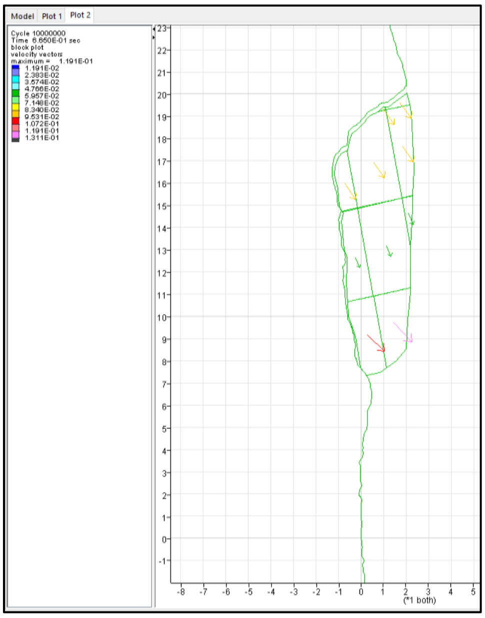

Fig. 15: jkn = 1E13, jks = 1E10, c = 2E7, step 1E7

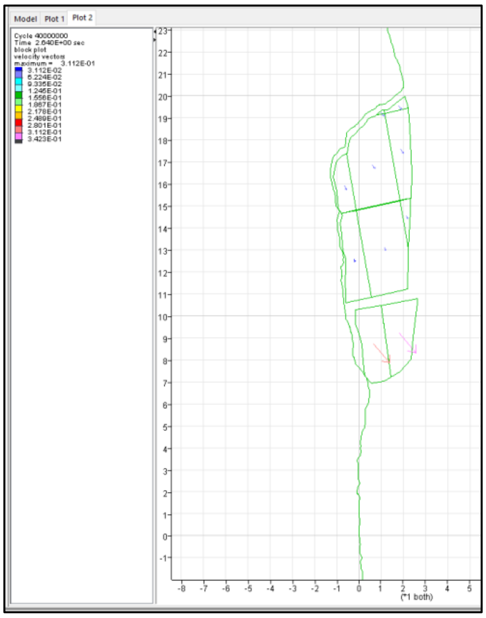

Fig. 16: jkn = 1E13, jks = 1E10, c = 2E7, step 4E7

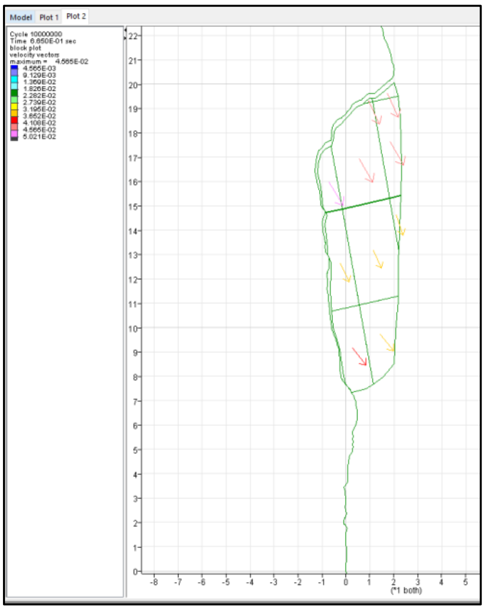

Fig. 17: jkn = 1E13, jks = 1E9, c = 2E7, step 1E7

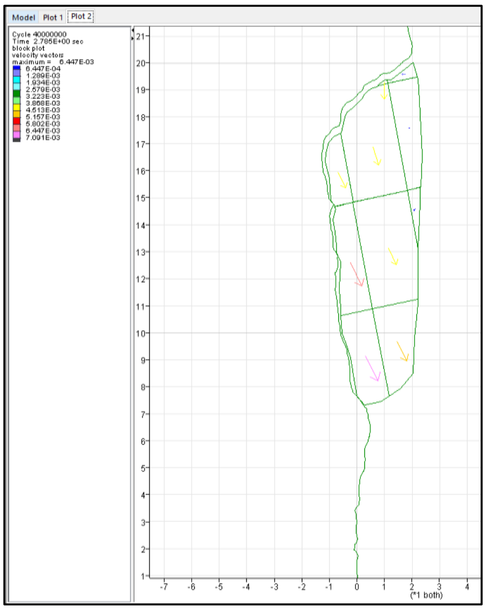

Fig. 18: jkn = 1E13, jks = 1E9, c = 2E7, step 4E7

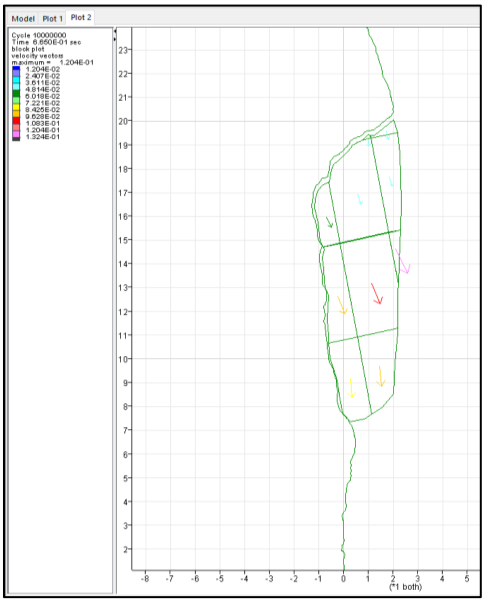

Fig. 19: jkn = 1E13, jks = 1E8, c = 2E7, step 1E7

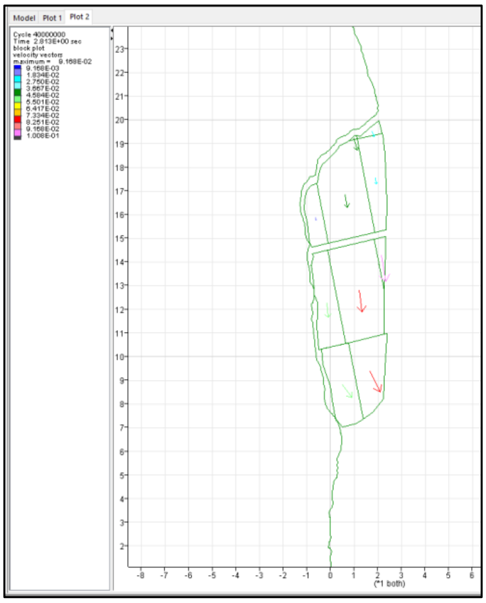

Fig. 20: jkn = 1E13, jks = 1E8, c = 2E7, step 4E7

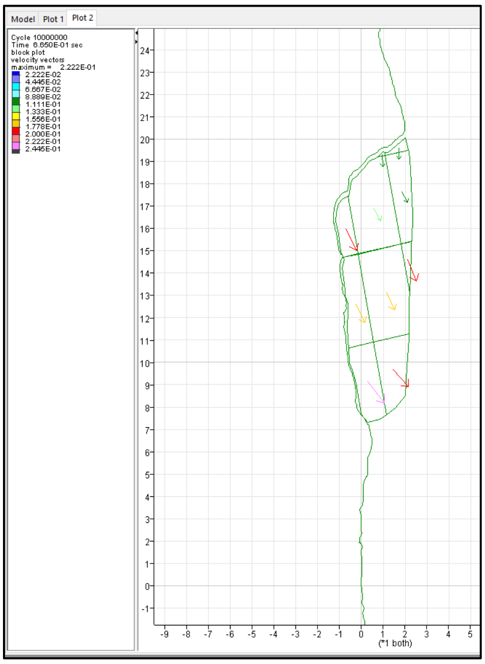

Fig. 21: jkn = 1E13, jks = 1E7, c = 2E7, step 1E7

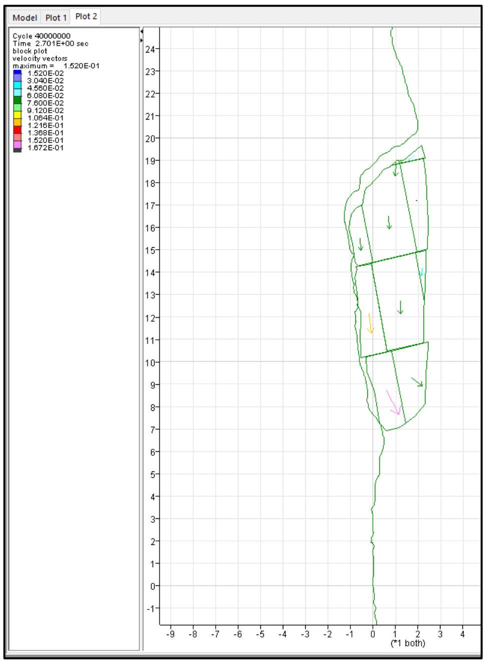

Fig. 22: jkn = 1E13, jks = 1E7, c = 2E7, step 4E7

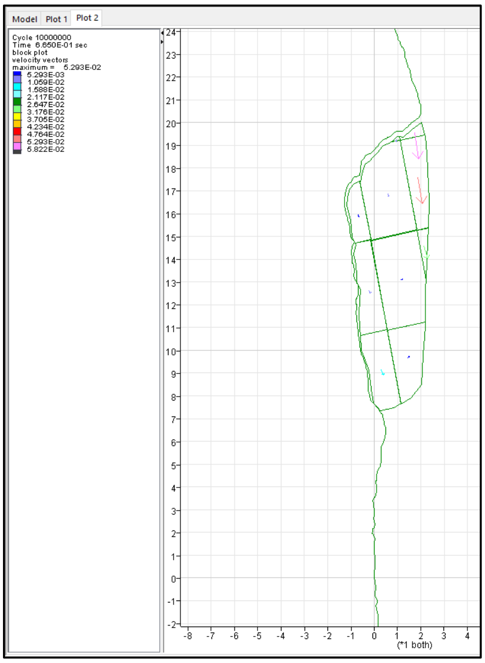

Fig. 23: jkn = 1E13, jks = 1E7, c = 2E7, step 1E7

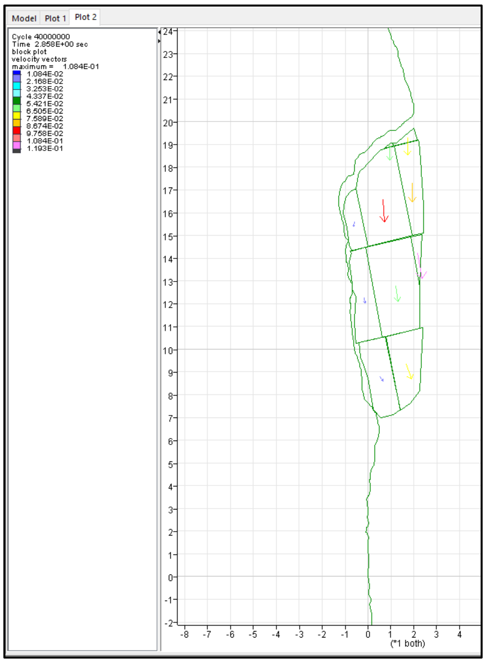

Fig. 24: jkn = 1E13, jks = 1E7, c = 2E7 , step 4E7

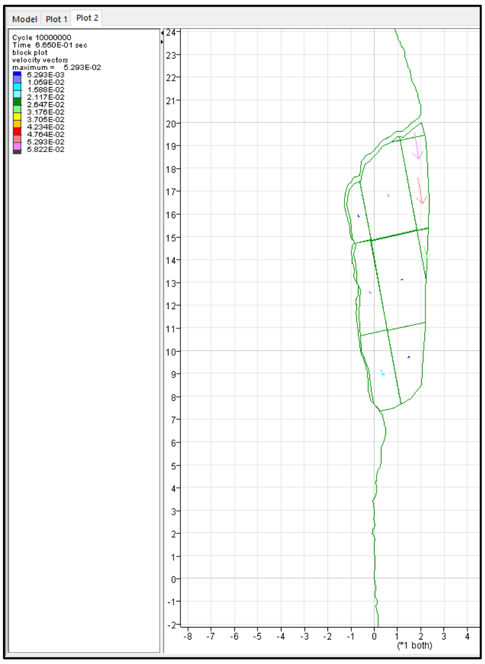

Fig. 25: jkn = 1E13, jks = 1E6, c = 2E7, step 1E7

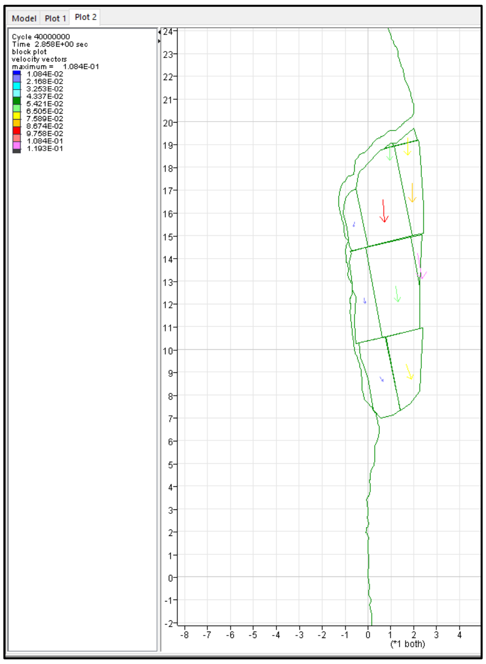

Fig. 26: jkn = 1E13, jks = 1E6, c = 2E7, step 4E7

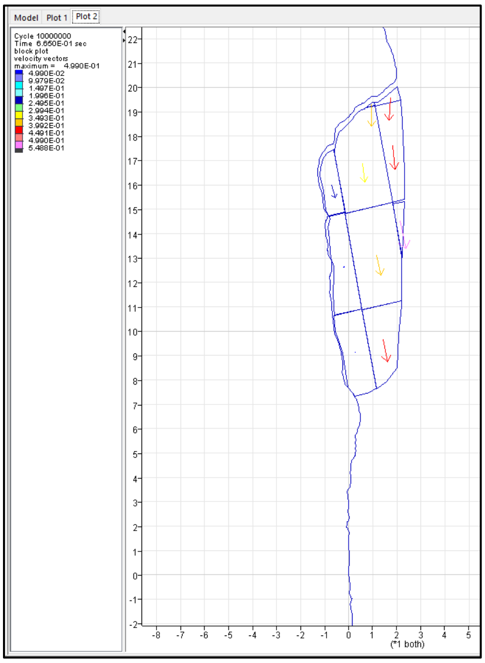

Fig. 27: jkn = 1E13, jks = 1E5, c = 2E7, step 1E7

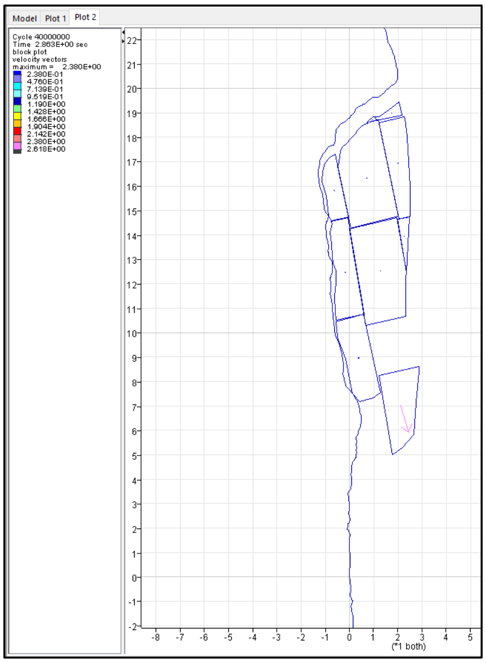

Fig. 28: jkn = 1E13, jks = 1E5, c = 2E7, step 4E7

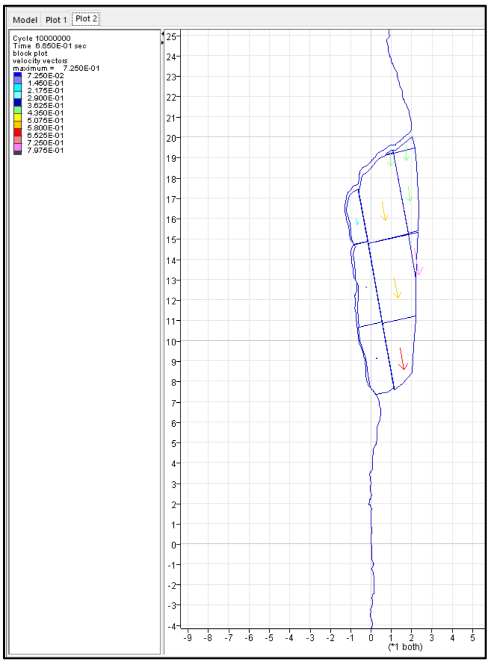

Fig. 29: jkn = 1E13, jks = 1E5, c = 0, step 1E7

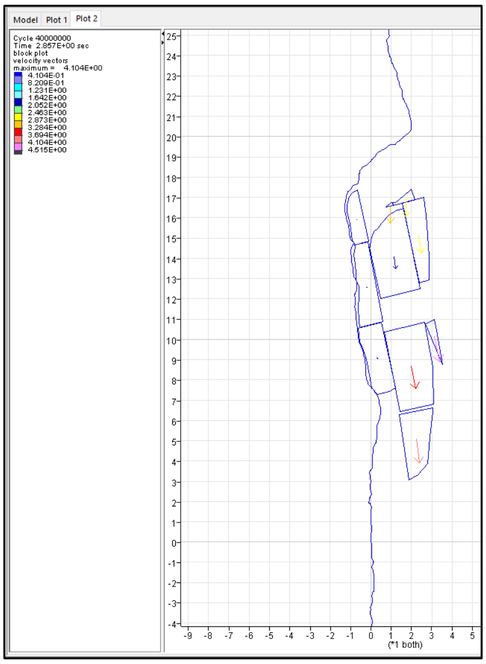

Fig. 30: jkn = 1E13, jks = 1E5, c = 0, step 4E7

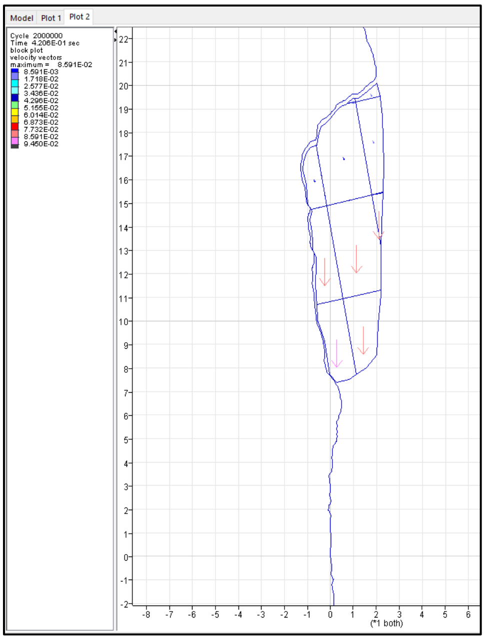

Fig. 31: jkn = 1E12, jks = 1E12, c = 2E7, step 2E6

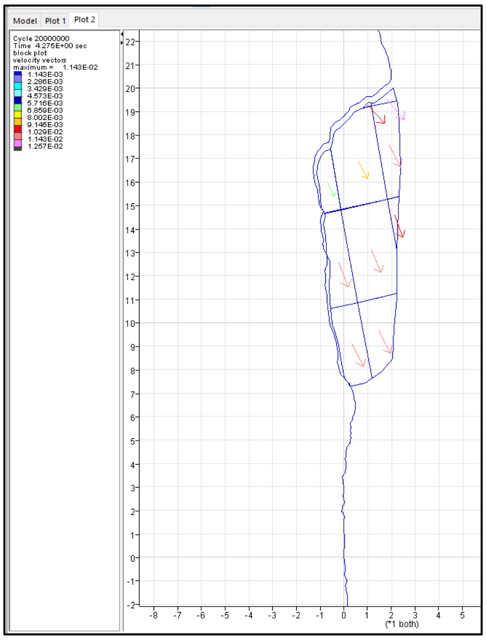

Fig. 32: jkn = 1E12, jks = 1E12, c = 2E7, step 2E7

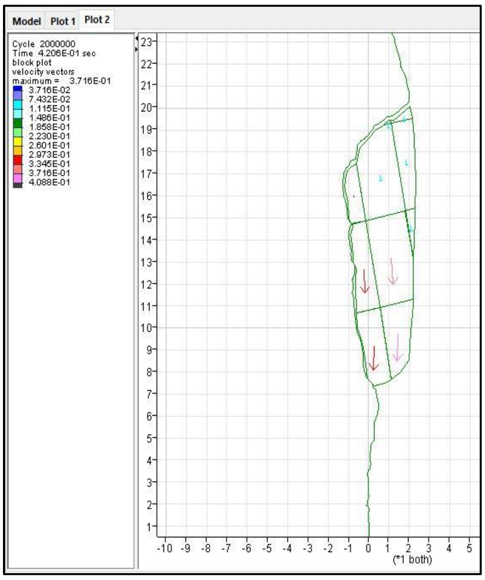

Fig. 33: jkn = 1E12, jks = 1E12, c = 0, step 2E6

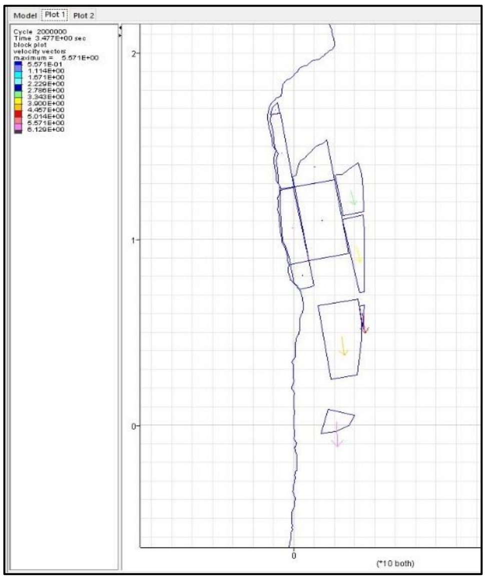

Fig. 34: jkn = 1E12, jks = 1E12, c = 0, step 2E7

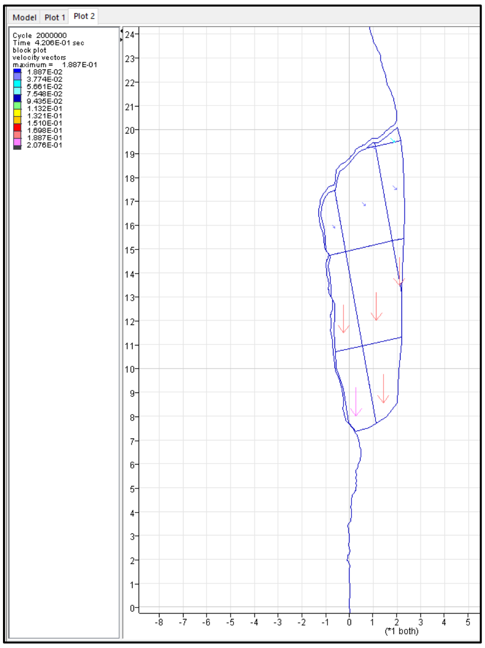

Fig. 35: jkn = 1E12, jks = 1E11, c = 2E7, step 2E6

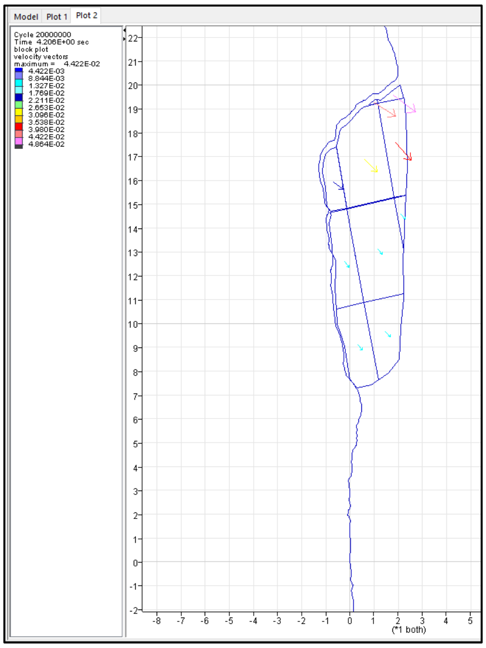

Fig. 36: jkn = 1E12, jks = 1E11, c = 2E7, step 2E7

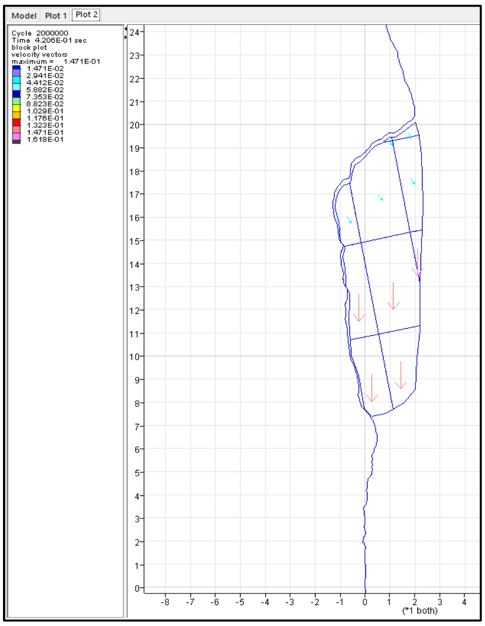

Fig. 37: jkn = 1E12, jks = 1E10, c = 2E7, step 2E6

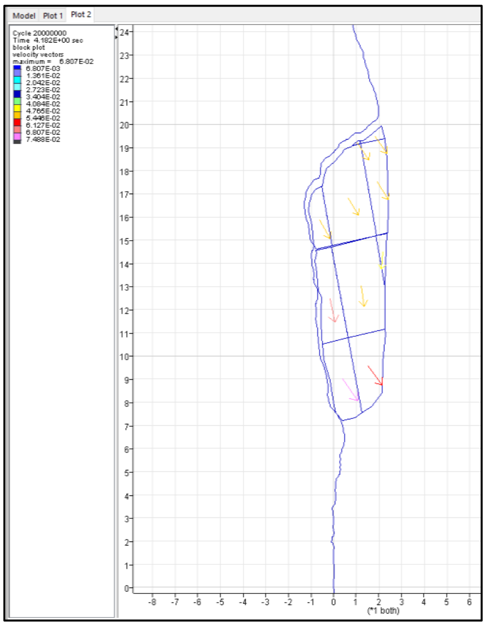

Fig. 38:, jkn = 1E12, jks = 1E10, c = 2E7, step 2E7

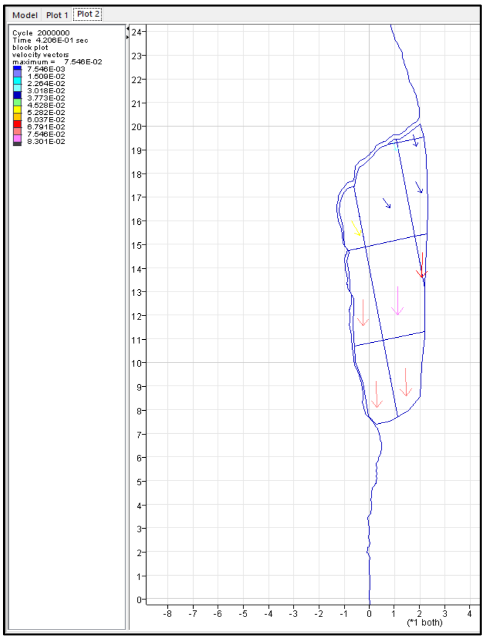

Fig. 39: jkn = 1E12, jks = 1E9, c = 2E7, step 2E6

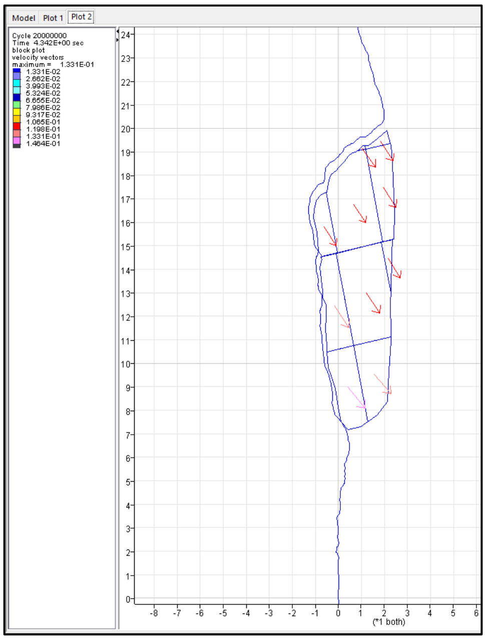

Fig. 40: jkn = 1E12, jks = 1E9, c = 2E7, step 2E7

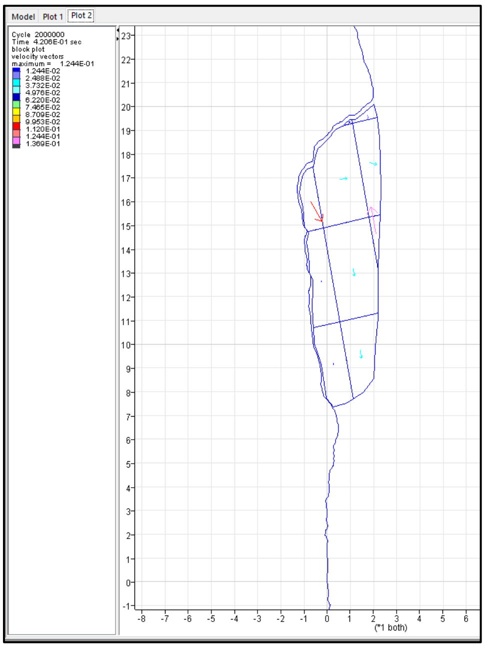

Fig. 41: jkn = 1E12, jks = 1E8, c = 2E7, step 2E6

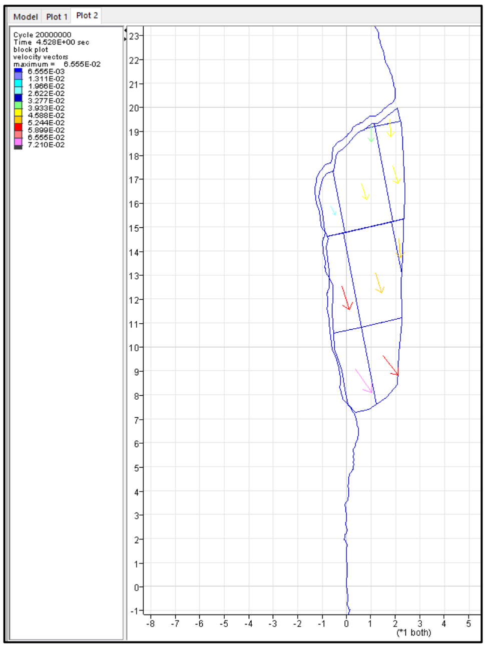

Fig. 42: jkn = 1E12, jks = 1E8, c = 2E7, step 2E7

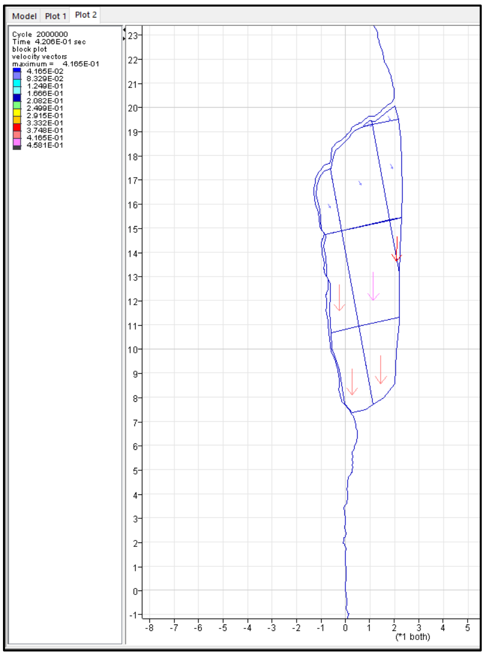

Fig. 43: jkn = 1E12, jks = 1E7, c = 2E7, step 2E6

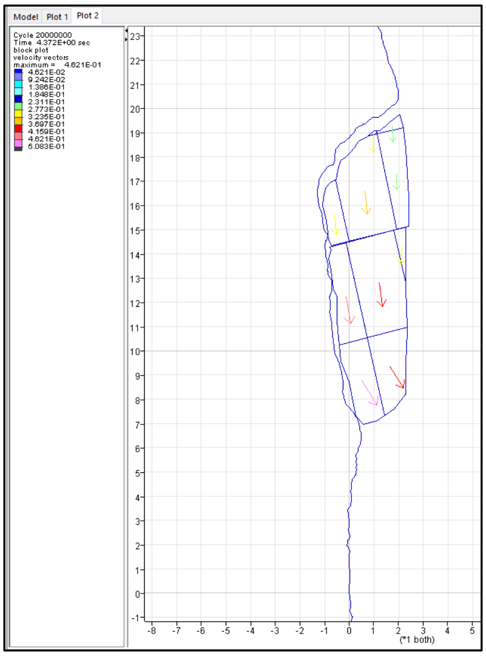

Fig. 44: jkn = 1E12, jks = 1E7, c = 2E7, step 2E7

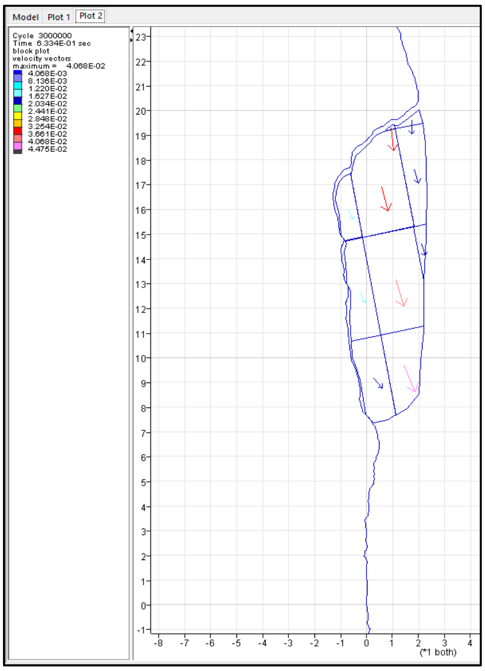

Fig. 45: jkn = 1E12, jks = 1E6, c = 2E7, step 3E6

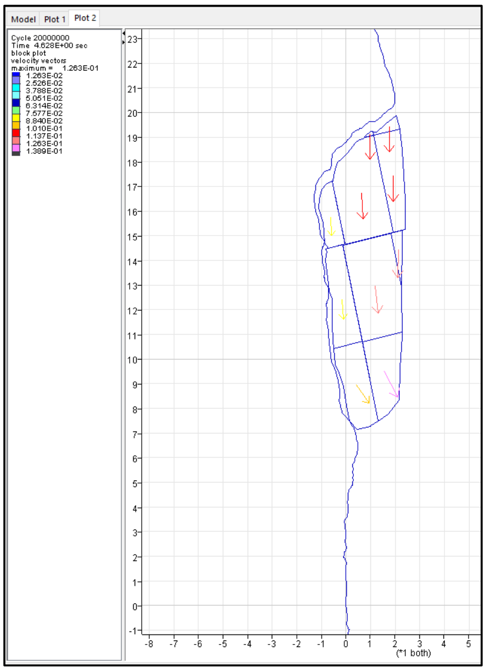

Fig. 46: jkn = 1E12, jks = 1E6, c = 2E7, step 2E7

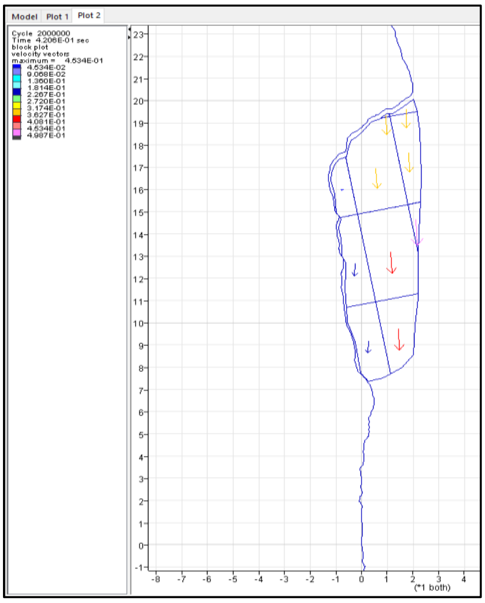

Fig. 47: jkn = 1E12, jks = 1E5, c = 2E7, step 2E6

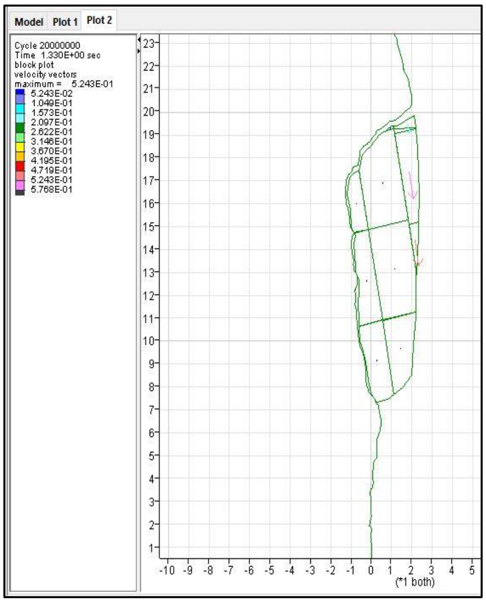

Fig. 48:, jkn = 1E12, jks = 1E5, c = 2E7, step 2E7

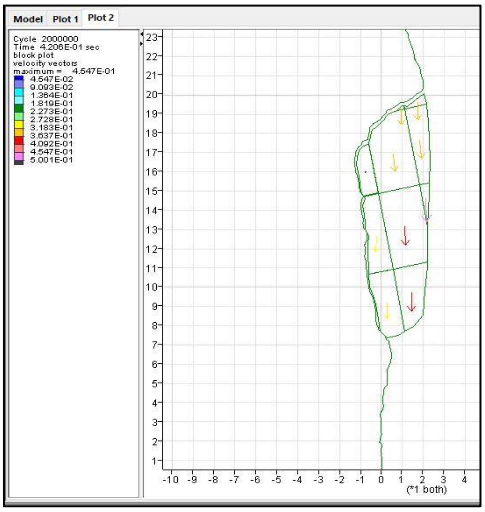

Fig. 49: jkn = 1E12, jks = 1E5, c = 0, step 2E6

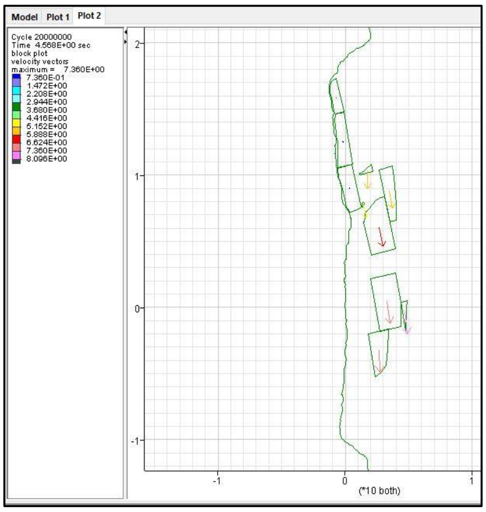

Fig. 50: jkn = 1E12, jks = 1E5, c = 0, step 2E7

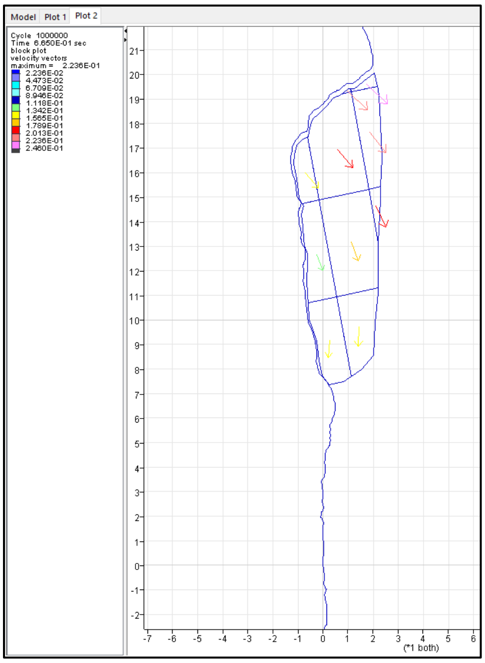

Fig. 51: jkn = 1E11, jks = 1E11, c = 2E7, step 1E6

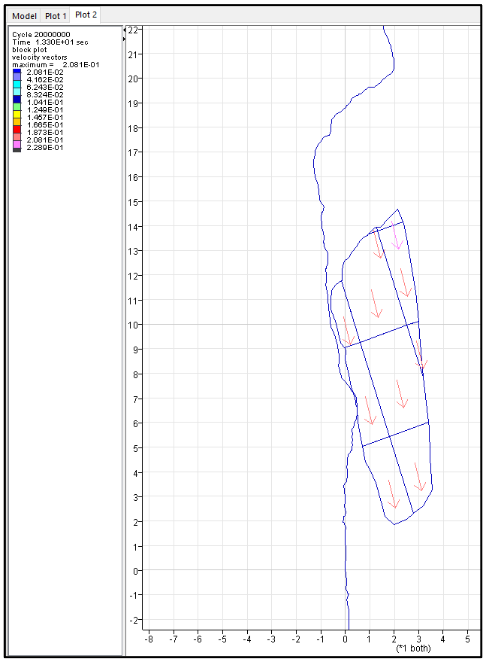

Fig. 52: jkn = 1E11, jks = 1E11, c = 2E7, step 2E7

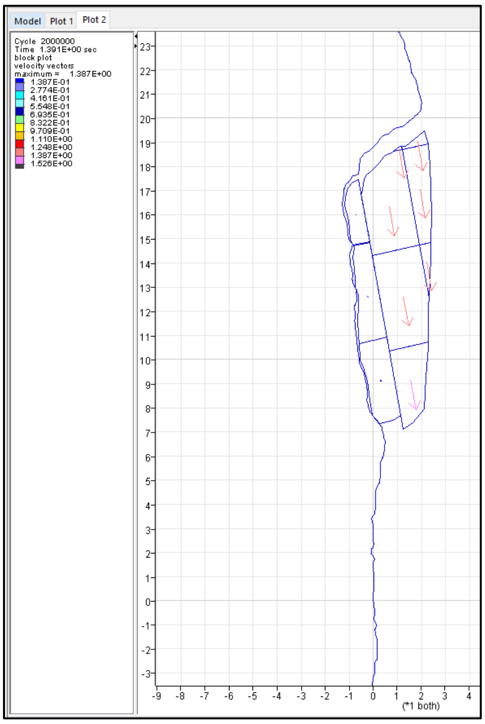

Fig. 53: jkn = 1E11, jks = 1E11, c = 0, step 2E6

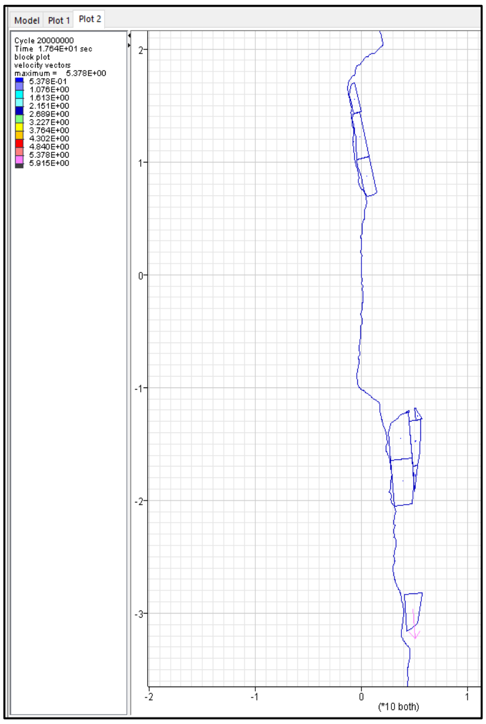

Fig. 54: jkn = 1E11, jks = 1E11, c = 0, step 2E7

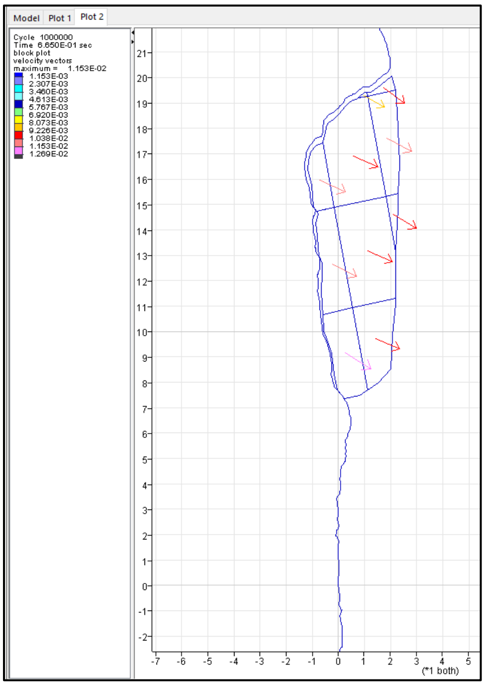

Fig. 55: jkn = 1E11, jks = 1E10, c = 2E7, step 1E6

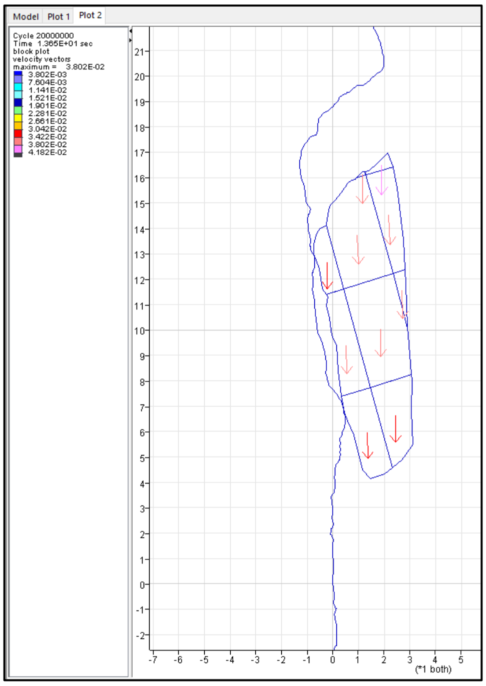

Fig. 56: jkn = 1E11, jks = 1E10, c = 2E7, step 2E7

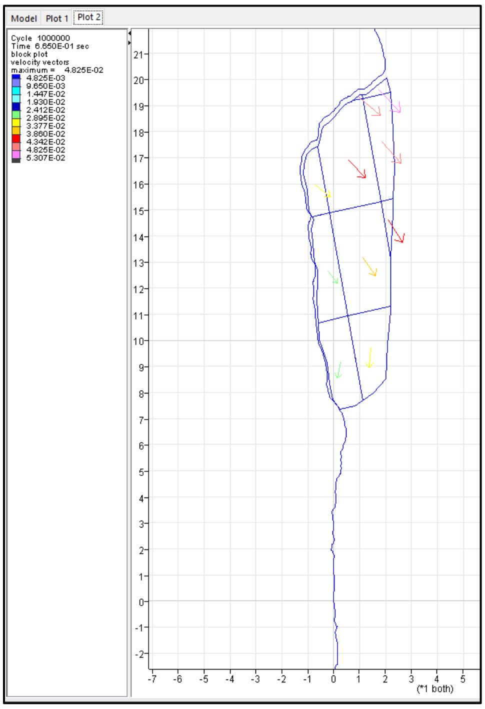

Fig. 57: jkn = 1E11, jks = 1E9, c = 2E7, step 1E6

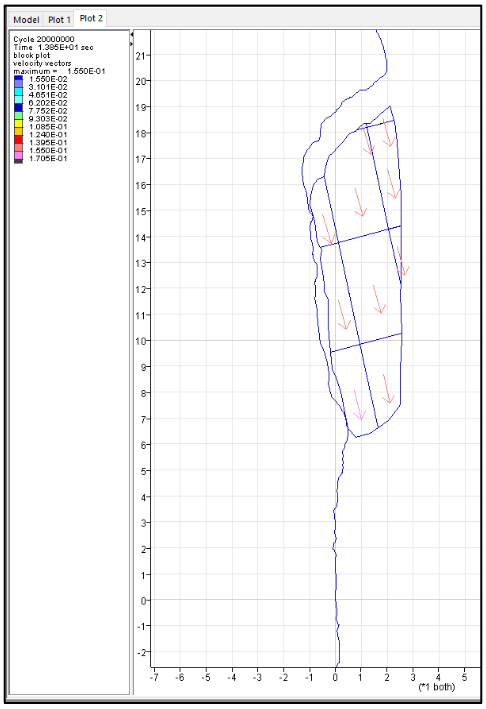

Fig. 58: jkn = 1E11, jks = 1E9, c = 2E7, step 2E7

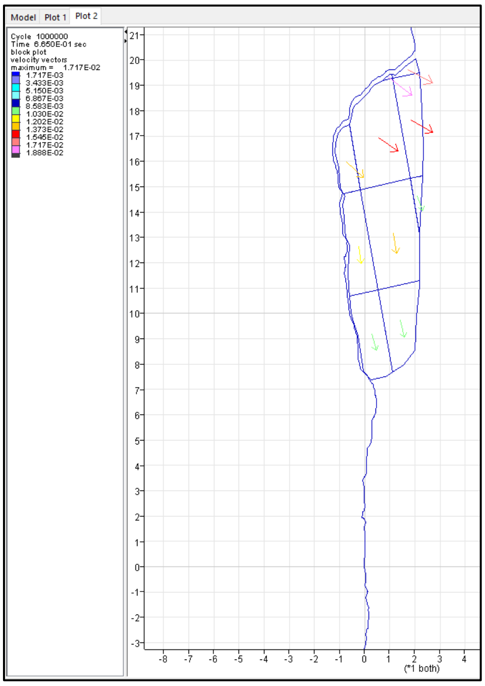

Fig. 59: jkn = 1E11, jks = 1E8, c = 2E7, step 1E6

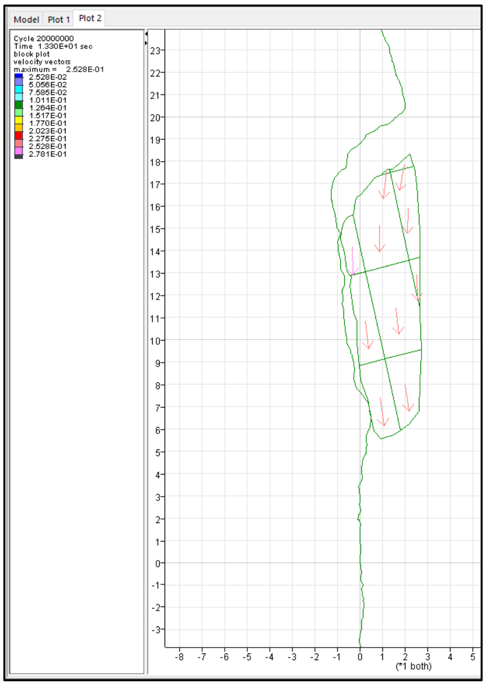

Fig. 60: jkn = 1E11, jks = 1E8, c = 2E7, step 2E7

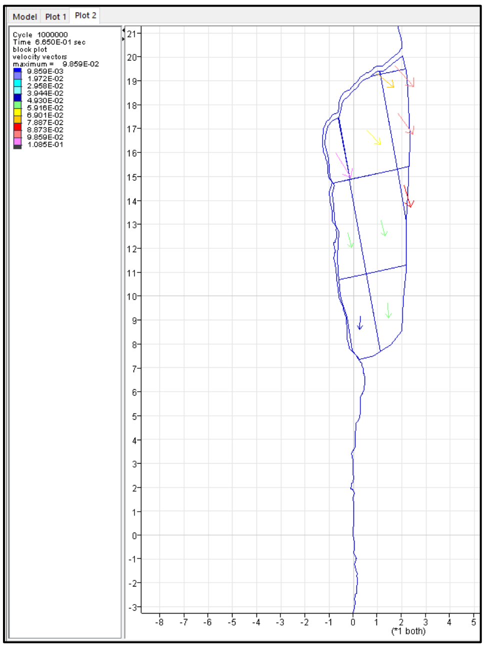

Fig. 61: jkn = 1E11, jks = 1E7, c = 2E7, step 1E6

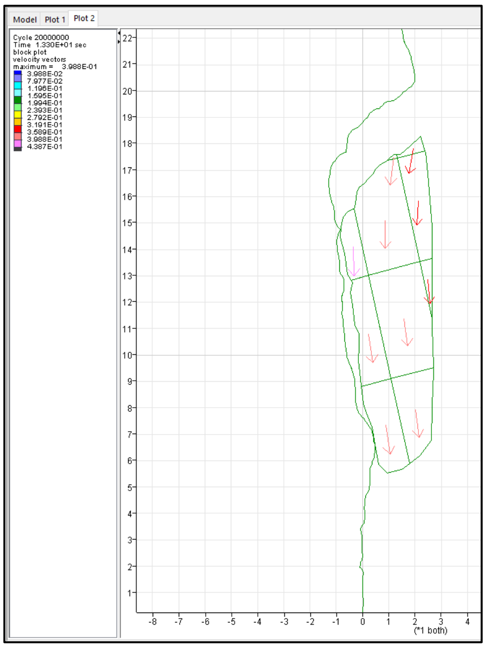

Fig. 62:, jkn = 1E11, jks = 1E7, c = 2E7, step 2E7

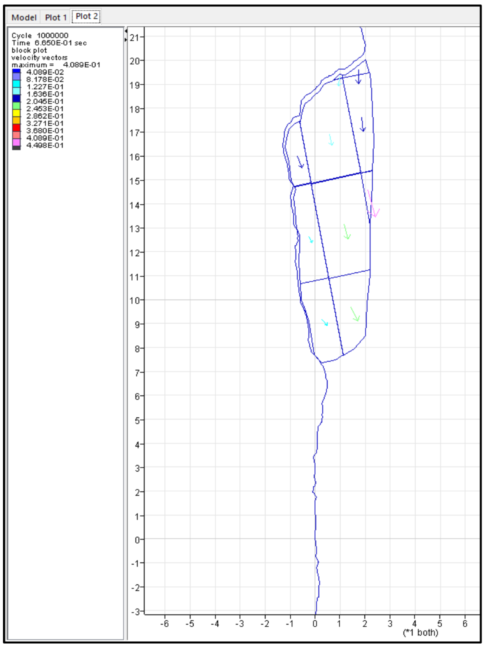

Fig. 63: jkn = 1E11, jks = 1E6, c = 2E7, step 1E6

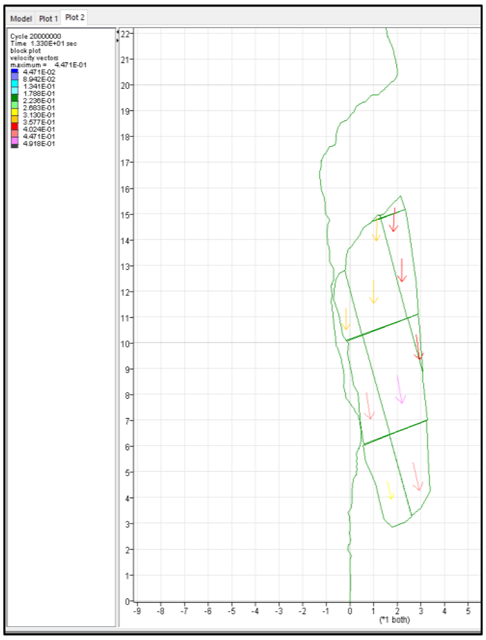

Fig. 64: jkn = 1E11, jks = 1E6, c = 2E7, step 2E7

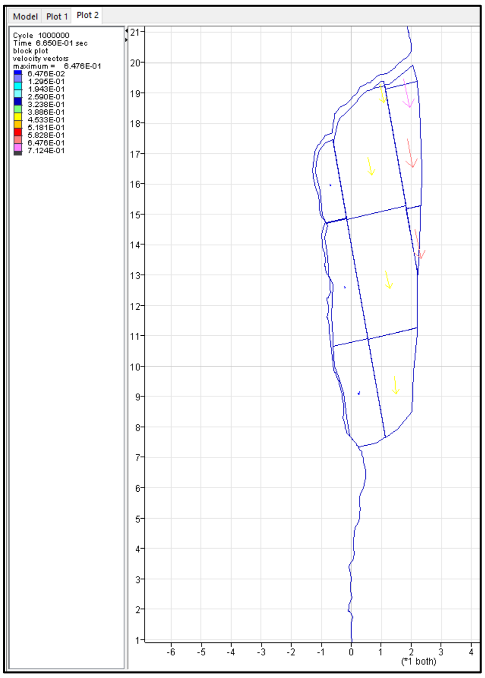

Fig. 65: jkn = 1E11, jks = 1E5, c = 2E7, step 1E6

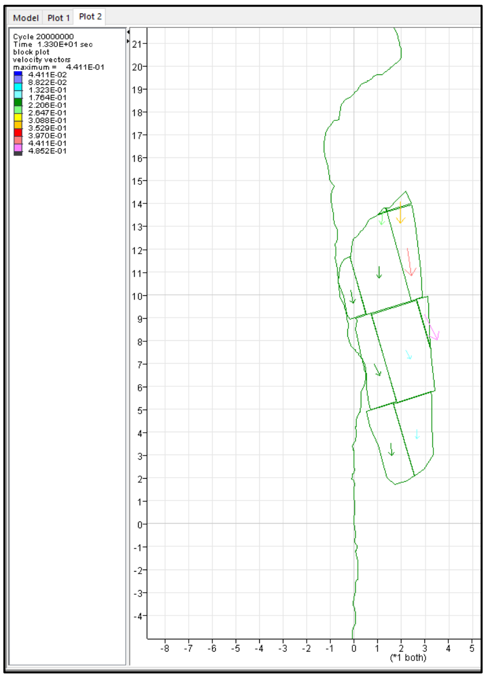

Fig. 66: jkn = 1E11, jks = 1E5, c = 2E7, step 2E7

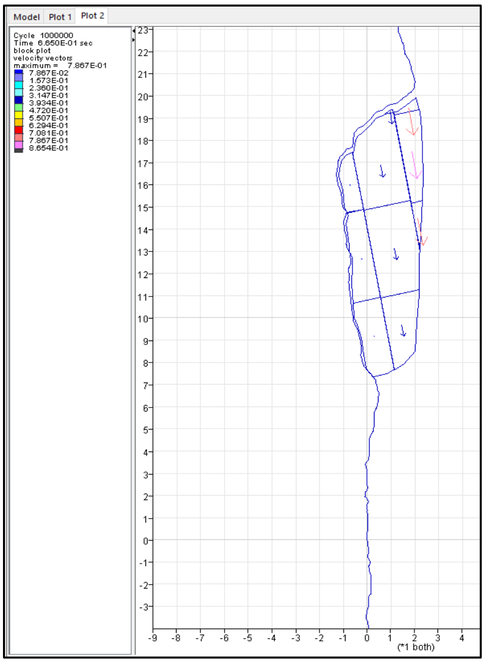

Fig. 67: jkn = 1E11, jks = 1E5, c = 0, step 1E6

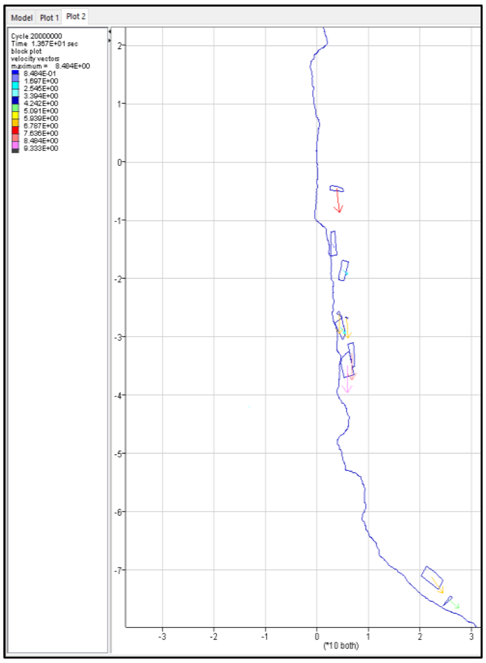

Fig. 68: jkn = 1E11, jks = 1E5, c = 0, step 2E7

Zoned-cracked model showing the maximum shear strain with varying jkn [Pa/m] = 1E11, 1E12, 1E13, and jks [Pa/m] = 1E5, 1E6, 1E7, 1E8, 1E9, 1E10, 1E11, 1E12, 1E13; c [Pa] = 2E7, 0

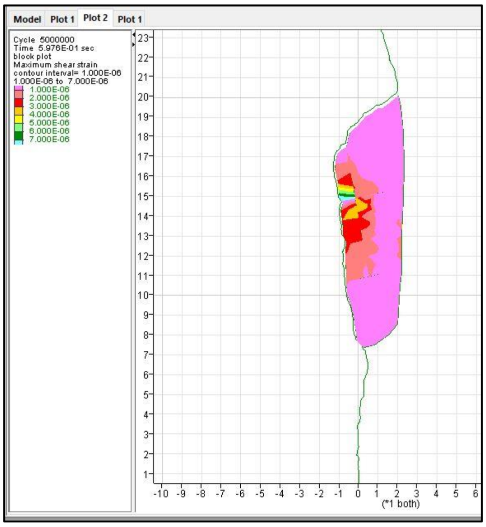

Fig. 69: jkn = 1E13, jks = 1E13, c = 2E7, step 5E6

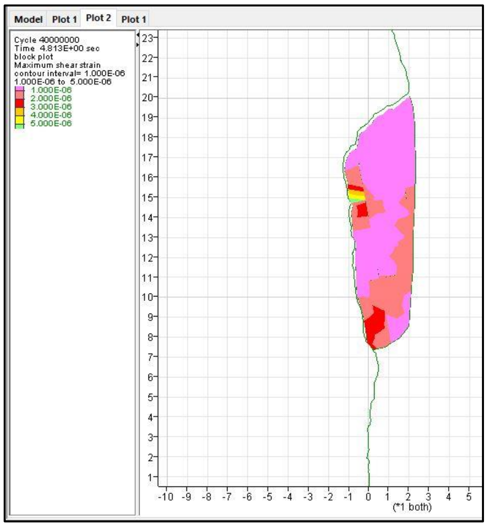

Fig. 70:, jkn = 1E13, jks = 1E13, c = 2E7, step 4E7

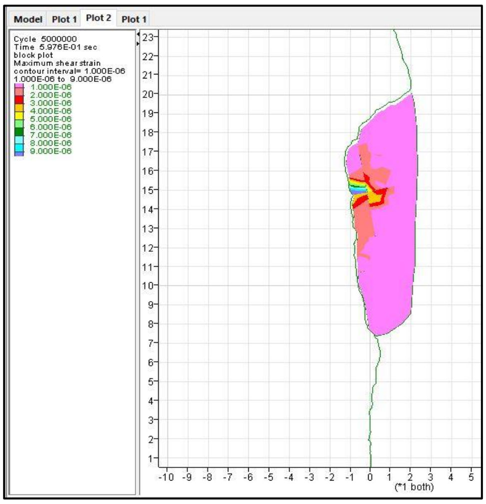

Fig. 71: jkn = 1E13, jks = 1E13, c = 0, step 5E6

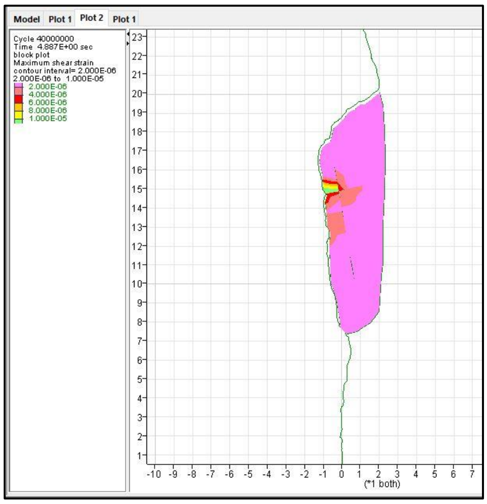

Fig. 72: jkn = 1E13, jks = 1E13, c = 0, step 4E7

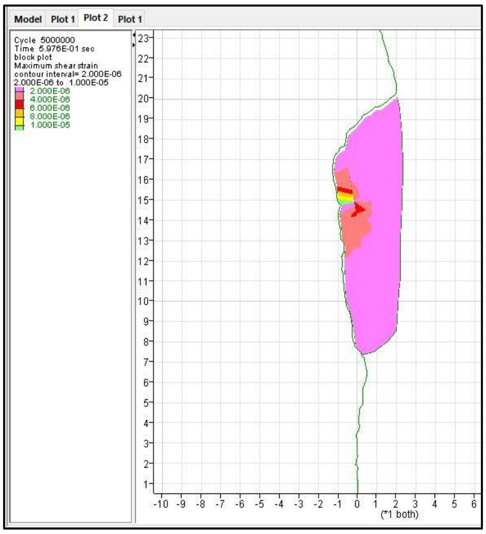

Fig. 73:, jkn = 1E13, jks = 1E12, c = 2E7, step 5E6

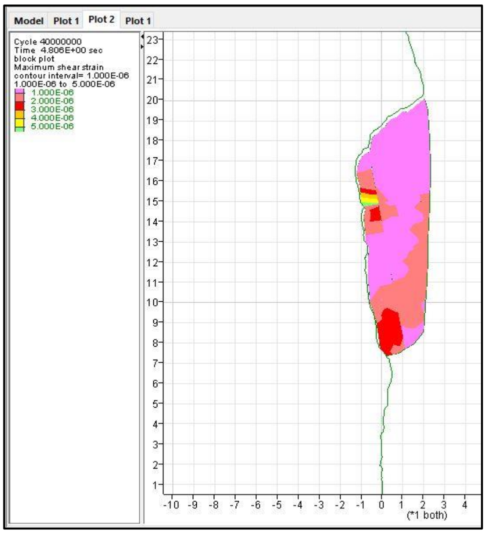

Fig. 74:, jkn = 1E13, jks = 1E12, c = 2E7, step 4E7

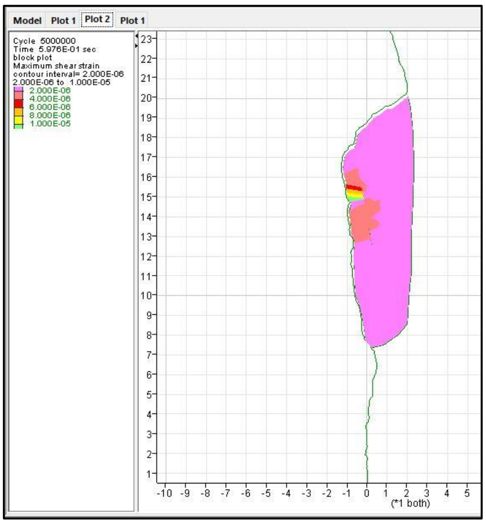

Fig. 75: jkn = 1E13, jks = 1E11, c = 2E7, step 5E6

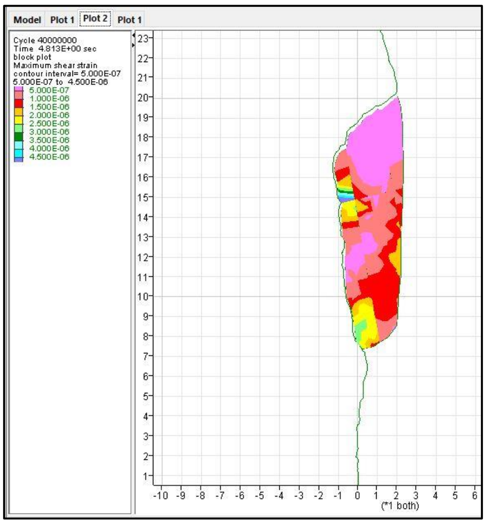

Fig. 76: jkn = 1E13, jks = 1E11, c = 2E7, step 4E7

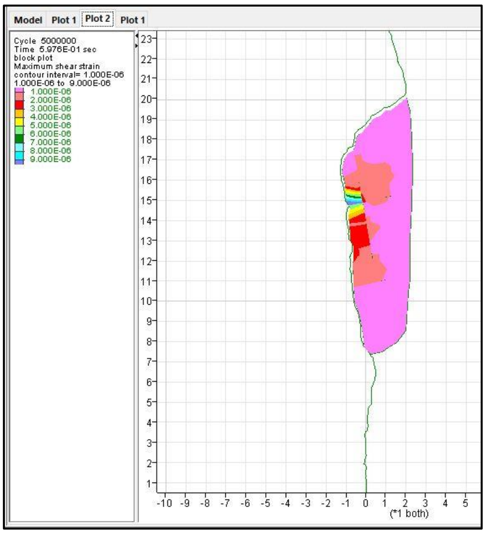

Fig. 77: jkn = 1E13, jks = 1E10, c = 2E7, step 5E6

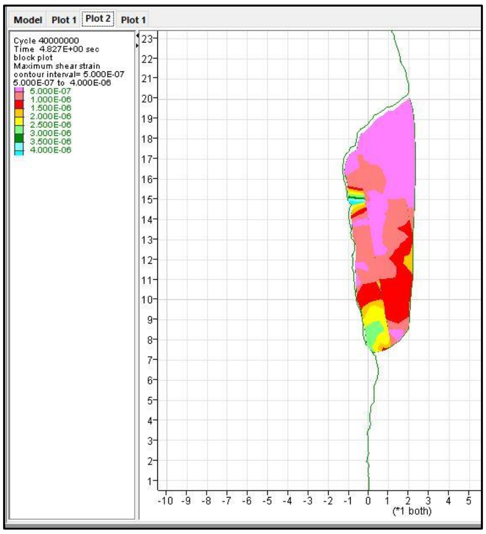

Fig. 78: jkn = 1E13, jks = 1E10, c = 2E7, step 4E7

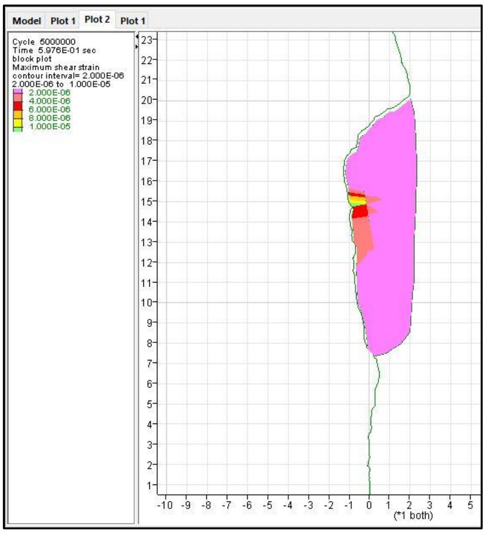

Fig. 79: jkn = 1E13, jks = 1E9, c = 2E7, step 5E6

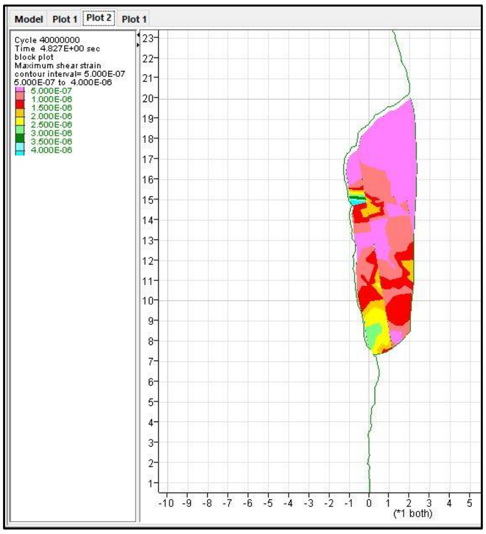

Fig. 80: jkn = 1E13, jks = 1E9, c = 2E7, step 4E7

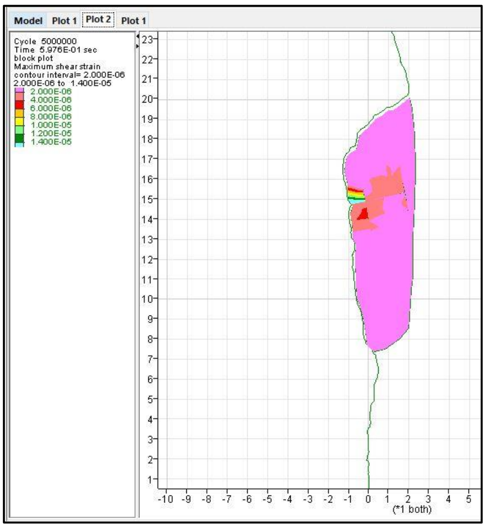

Fig. 81: jkn = 1E13, jks = 1E8, c = 2E7, step 5E6

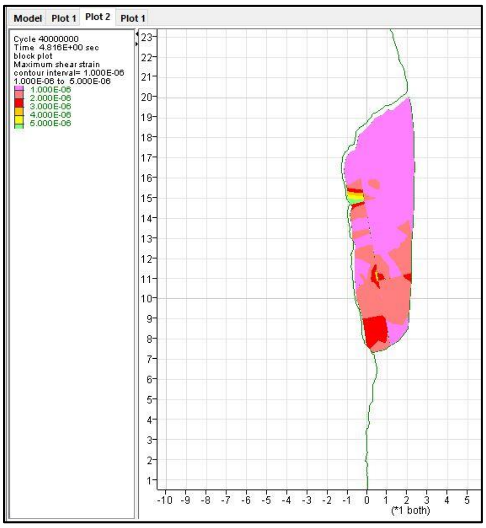

Fig. 82: jkn = 1E13, jks = 1E8, c = 2E7, step 4E7

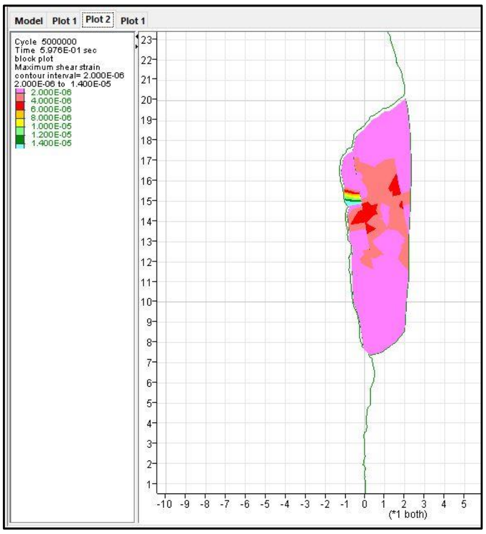

Fig. 83: jkn = 1E13, jks = 1E7, c = 2E7, step 5E6

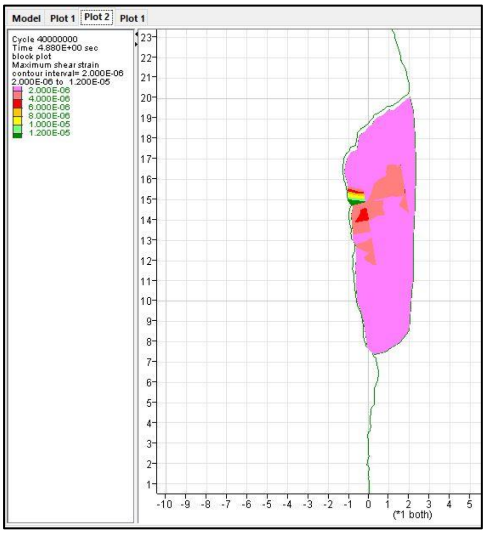

Fig. 84: jkn = 1E13, jks = 1E7, c = 2E7, step 4E7

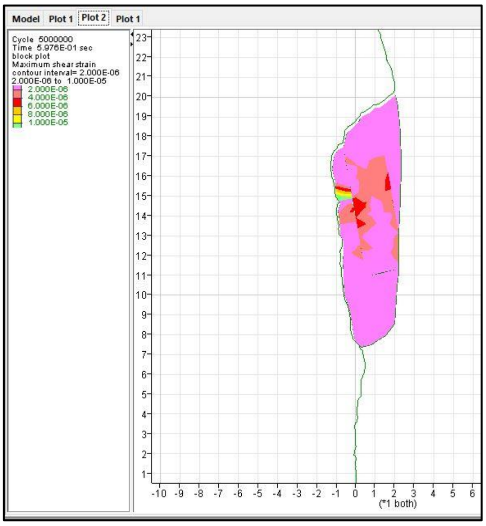

Fig. 85: jkn = 1E13, jks = 1E6, c = 2E7, step 5E6

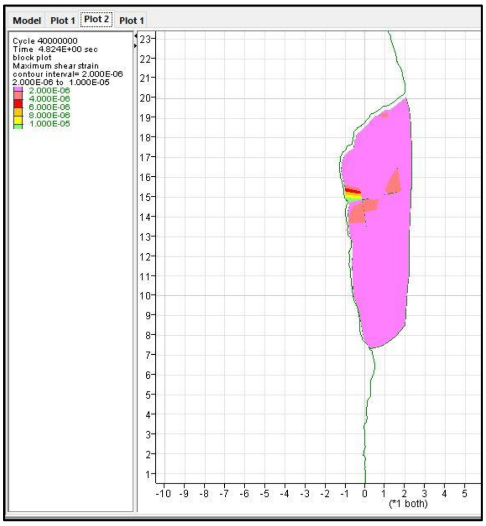

Fig. 86: jkn = 1E13, jks = 1E6, c = 2E7, step 4E7

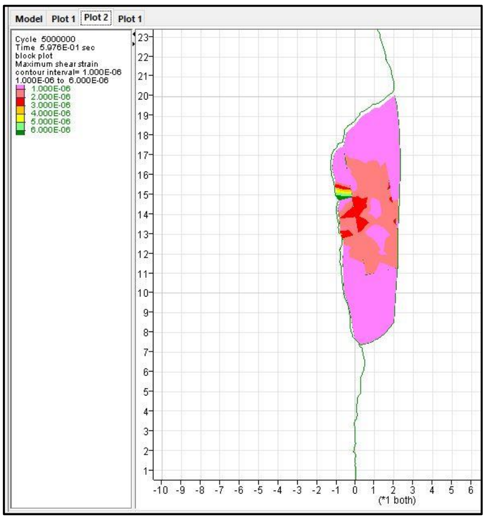

Fig. 87: jkn = 1E13, jks = 1E5, c = 2E7, step 5E6

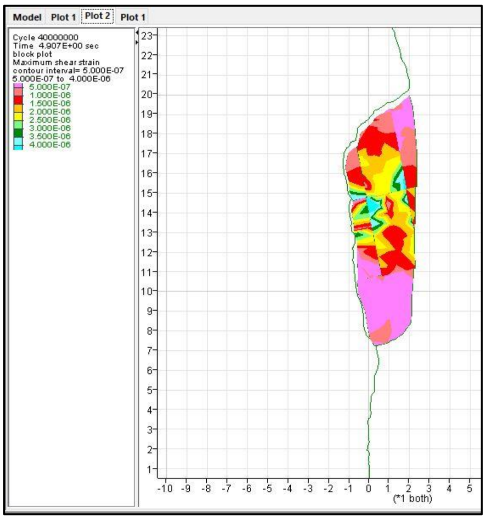

Fig. 88: jkn = 1E13, jks = 1E5, c = 2E7, step 4E7

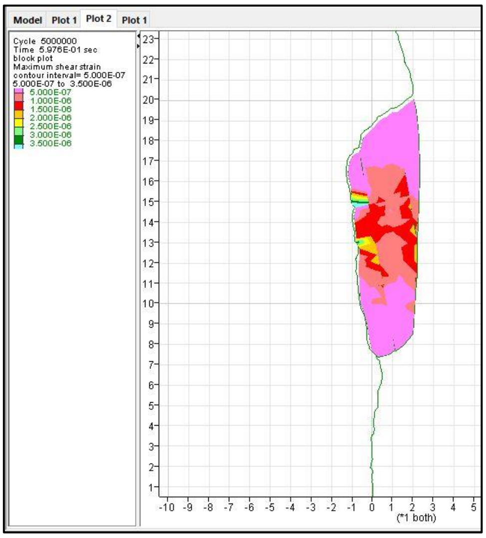

Fig. 89: jkn = 1E13, jks = 1E5, c = 0, step 5E6

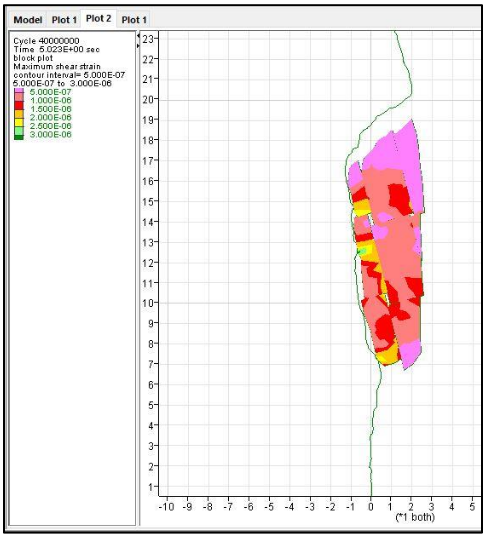

Fig. 90: jkn = 1E13, jks = 1E5, c = 0, step 4E7

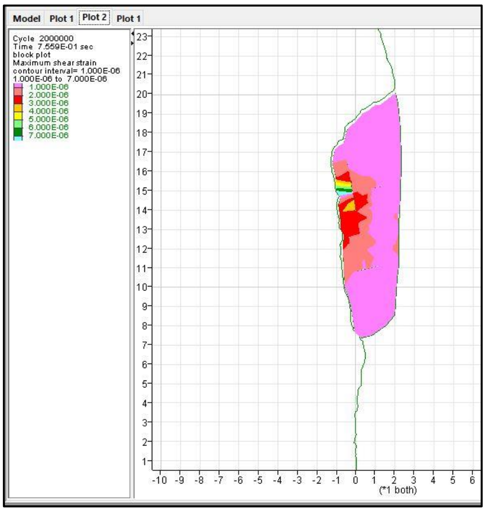

Fig. 91: jkn = 1E12, jks = 1E12, c = 2E7, step 2E6

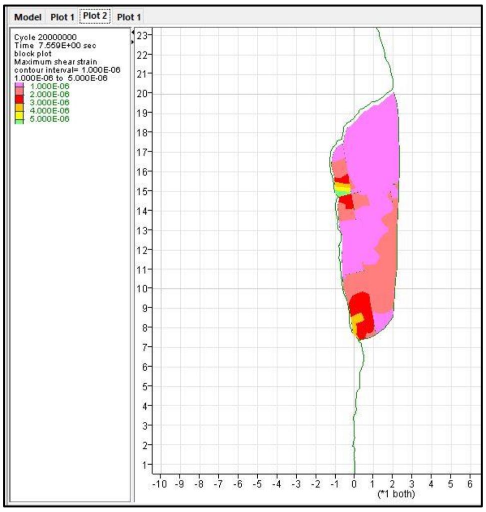

Fig. 92: jkn = 1E12, jks = 1E12, c = 2E7, step 2E7

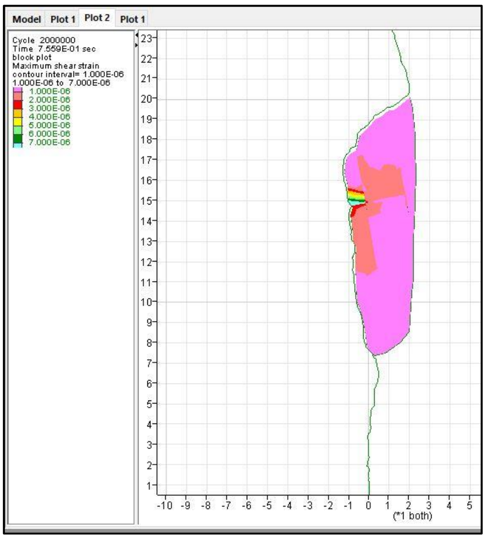

Fig. 93: jkn = 1E12, jks = 1E12, c = 0, step 2E6

Fig. 94: jkn = 1E12, jks = 1E12, c = 0, step 2E7

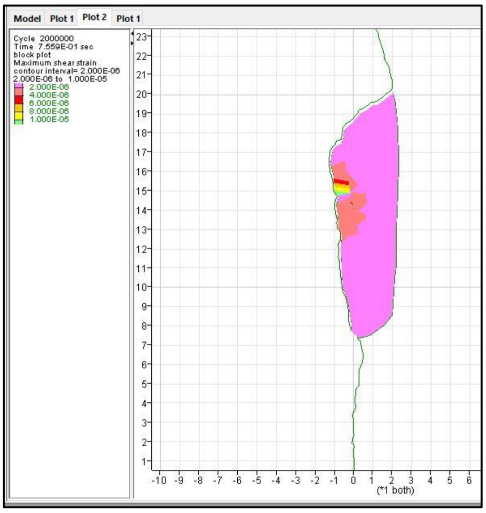

Fig. 95: jkn = 1E12, jks = 1E11, c = 2E7, step 2E6

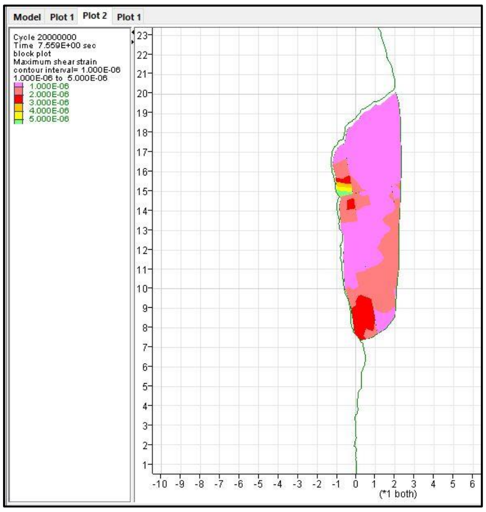

Fig. 96: jkn = 1E12, jks = 1E11, c = 2E7, step 2E7

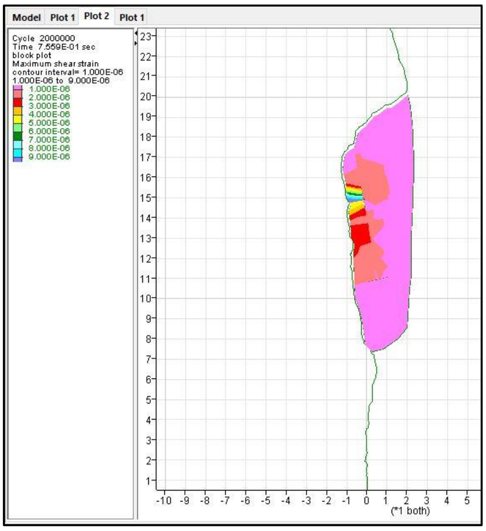

Fig. 97: jkn = 1E12, jks = 1E10, c = 2E7, step 2E6

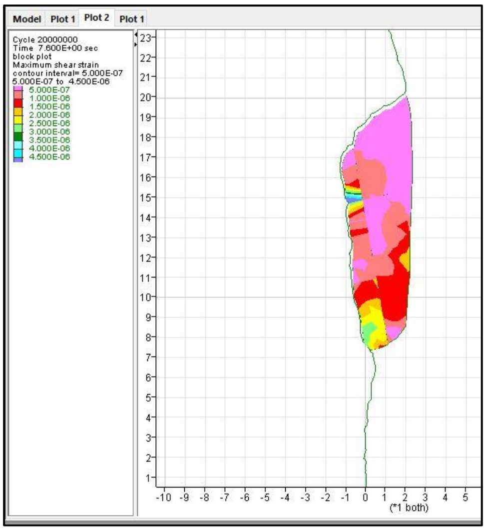

Fig. 98: jkn = 1E12, jks = 1E10, c = 2E7, step 2E7

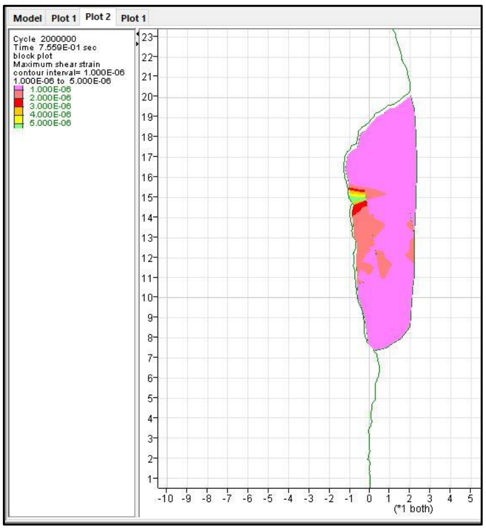

Fig. 99: jkn = 1E12, jks = 1E9, c = 2E7, step 2E6

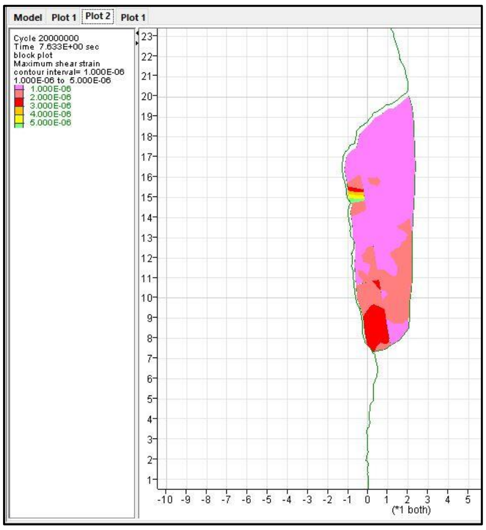

Fig. 100: jkn = 1E12, jks = 1E9, c = 2E7, step 2E7

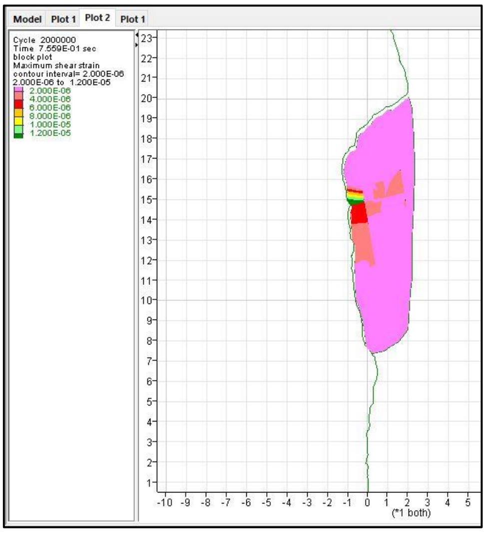

Fig. 101: jkn = 1E12, jks = 1E8, c = 2E7, step 2E6

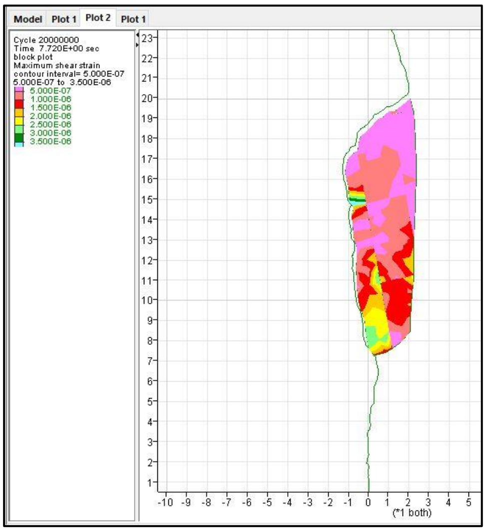

Fig. 102: jkn = 1E12, jks = 1E8, c = 2E7, step 2E7

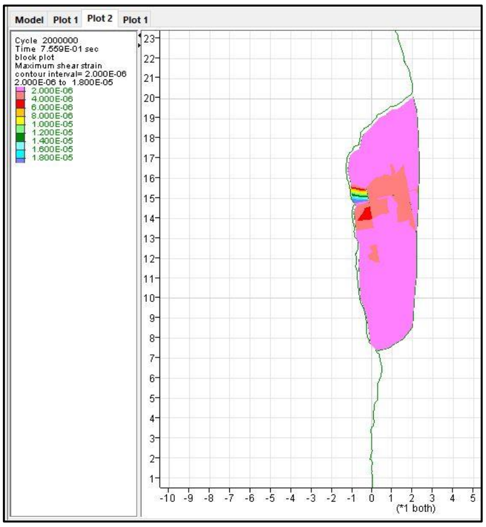

Fig. 103: jkn = 1E12, jks = 1E7, c = 2E7, step 2E6

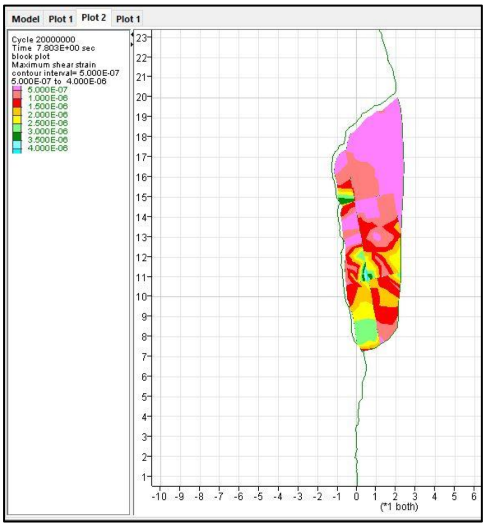

Fig. 104: jkn = 1E12, jks = 1E7, c = 2E7, step 2E7

Fig. 105: jkn = 1E12, jks = 1E6, c = 2E7, step 2E6

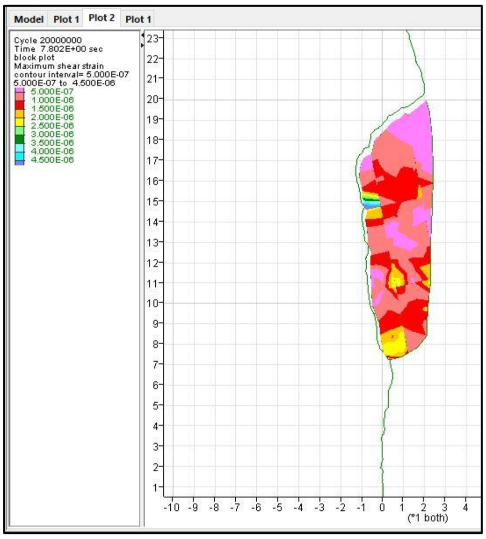

Fig. 106: jkn = 1E12, jks = 1E6, c = 2E7, step 2E7

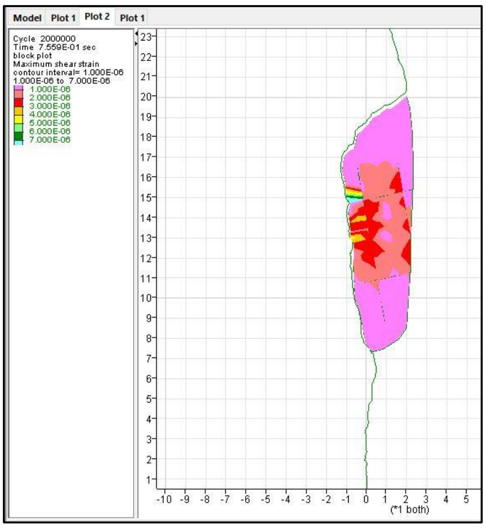

Fig. 107: jkn = 1E12, jks = 1E5, c = 2E7, step 2E6

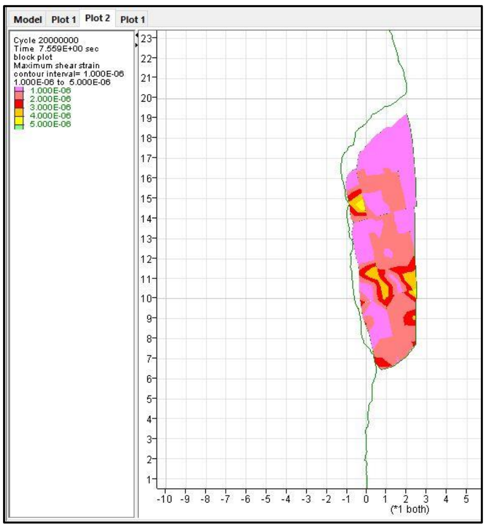

Fig. 108: jkn = 1E12, jks = 1E5, c = 2E7, step 2E7

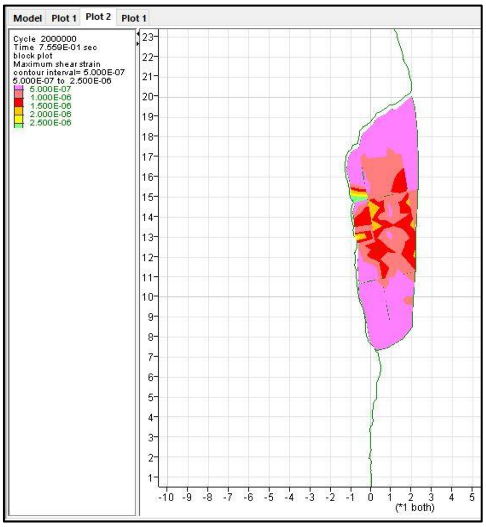

Fig. 109: jkn = 1E12, jks = 1E5, c = 0, step 2E6

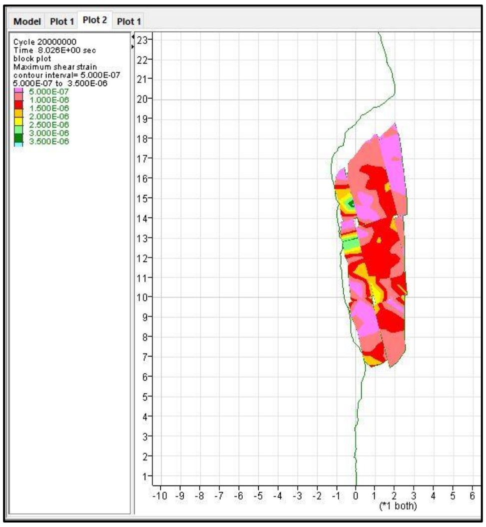

Fig. 110: jkn = 1E12, jks = 1E5, c = 0, step 2E7

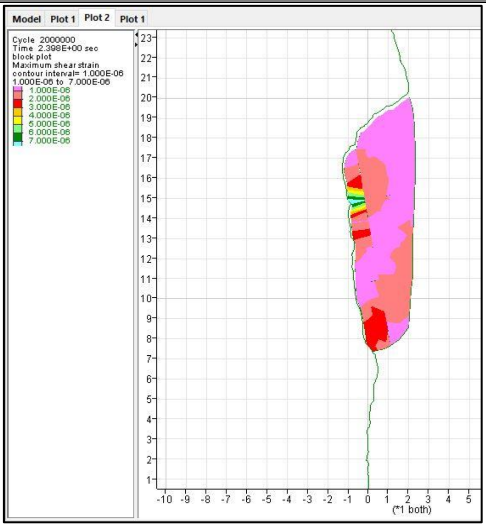

Fig. 111: jkn = 1E11, jks = 1E11, c = 2E7, step 2E6

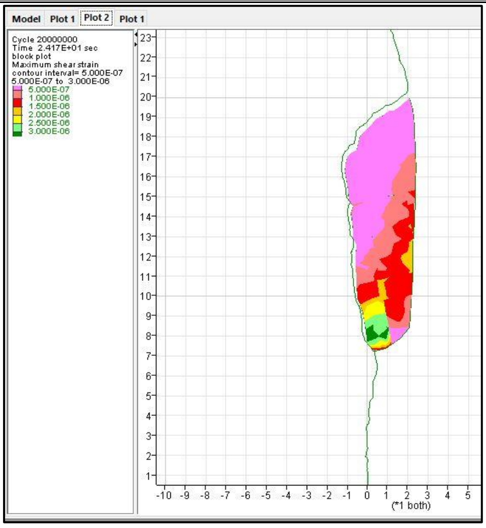

Fig. 112: jkn = 1E11, jks = 1E11, c = 2E7, step 2E7

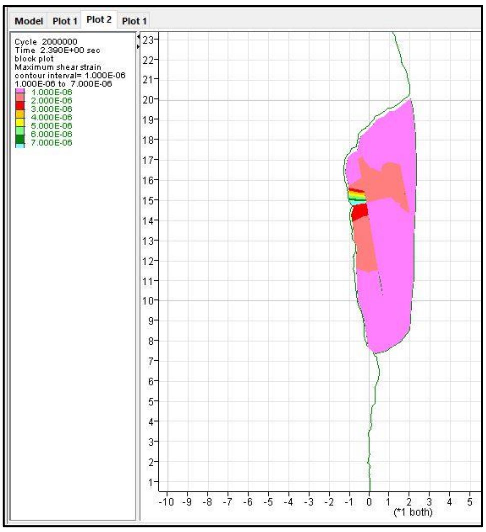

Fig. 113: jkn = 1E11, jks = 1E11, c = 0, step 2E6

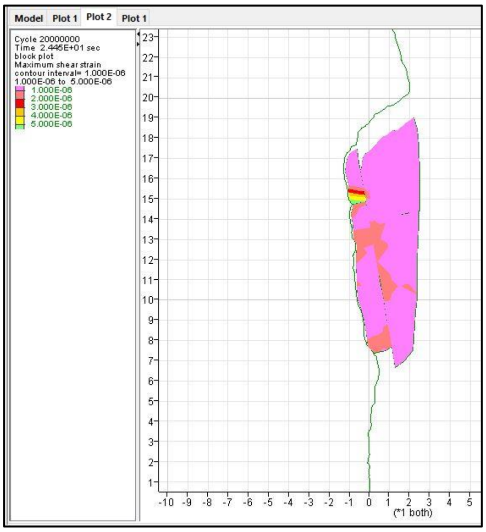

Fig. 114: jkn = 1E11, jks = 1E11, c = 0, step 2E7

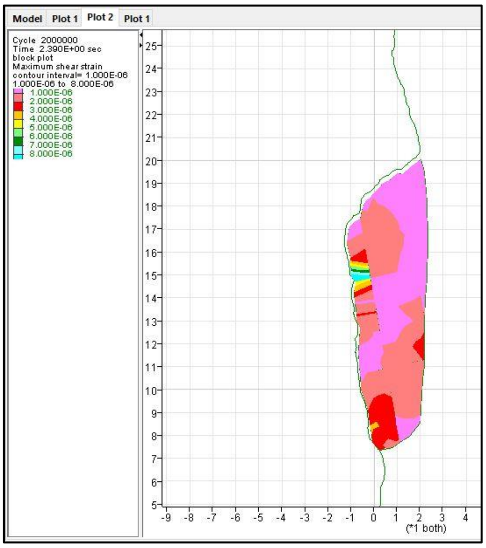

Fig. 115: jkn = 1E11, jks = 1E10, c = 2E7, step 2E6

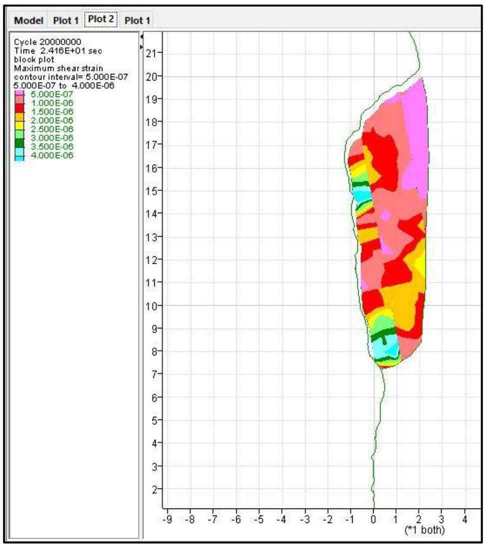

Fig. 116: jkn = 1E11, jks = 1E10, c = 2E7, step 2E7

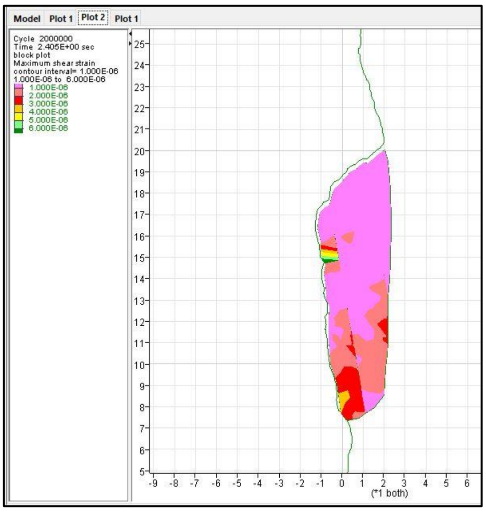

Fig. 117: jkn = 1E11, jks = 1E9, c = 2E7, step 2E6

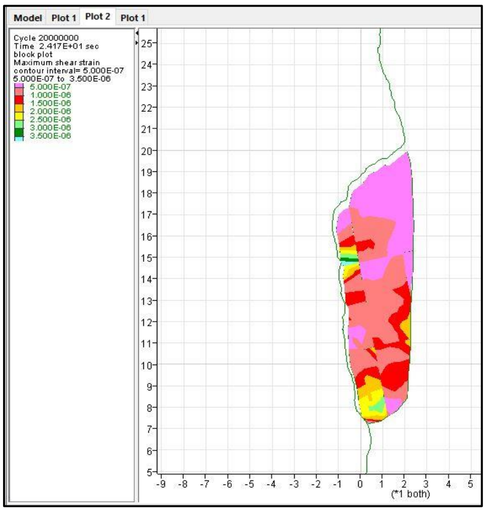

Fig. 118: jkn = 1E11, jks = 1E9, c = 2E7, step 2E7

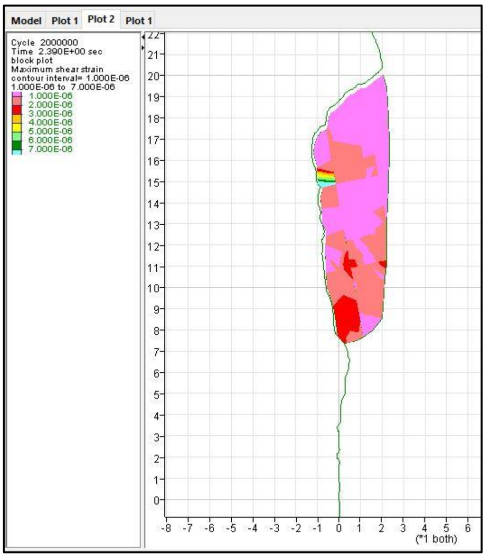

Fig. 119: jkn = 1E11, jks = 1E8, c = 2E7, step 2E6

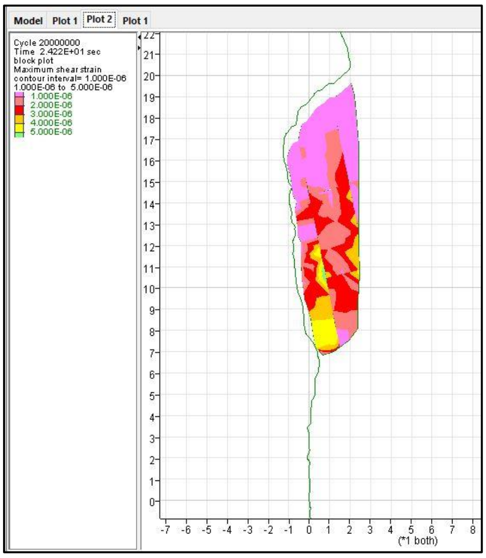

Fig. 120:, jkn = 1E11, jks = 1E8, c = 2E7, step 2E7

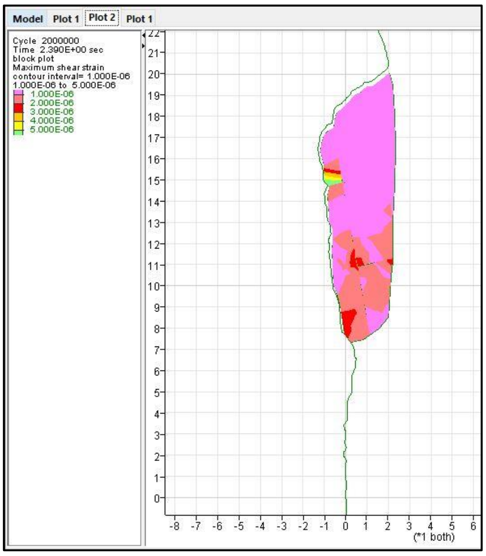

Fig. 121: jkn = 1E11, jks = 1E7, c = 2E7, step 2E6

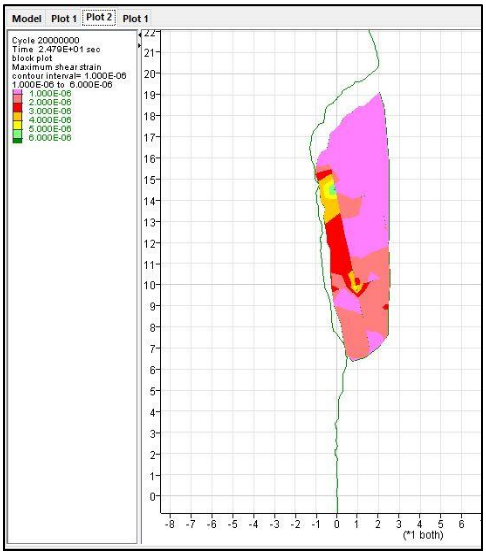

Fig. 122: jkn = 1E11, jks = 1E7, c = 2E7, step 2E7

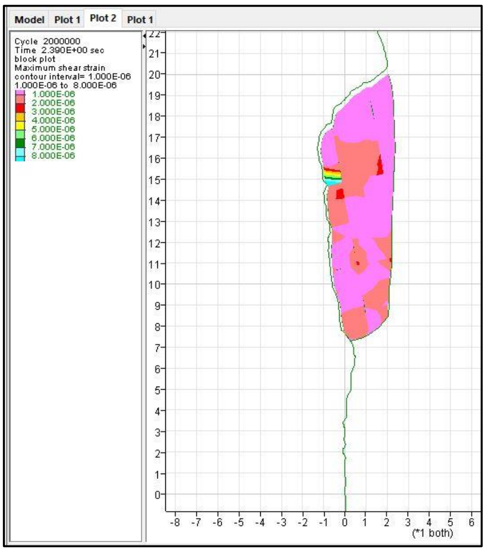

Fig. 123: jkn = 1E11, jks = 1E6, c = 2E7, step 2E6

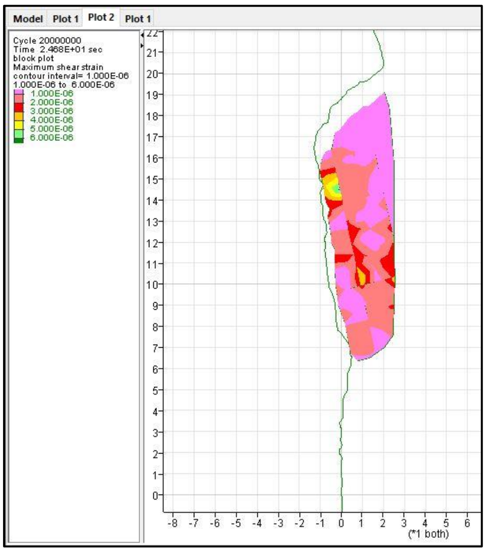

Fig. 124: jkn = 1E11, jks = 1E6, c = 2E7, step 2E7

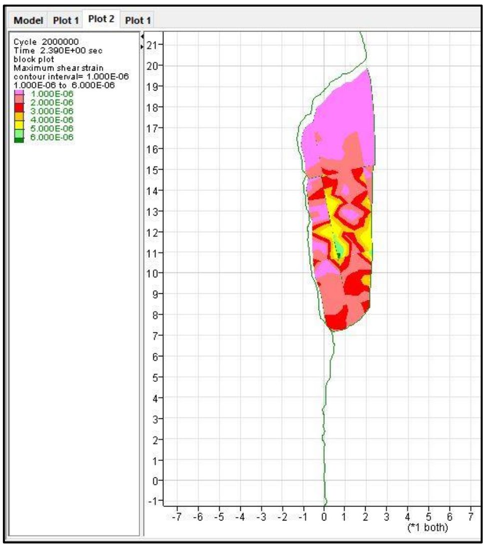

Fig. 125: jkn = 1E11, jks = 1E5, c = 2E7, step 2E6

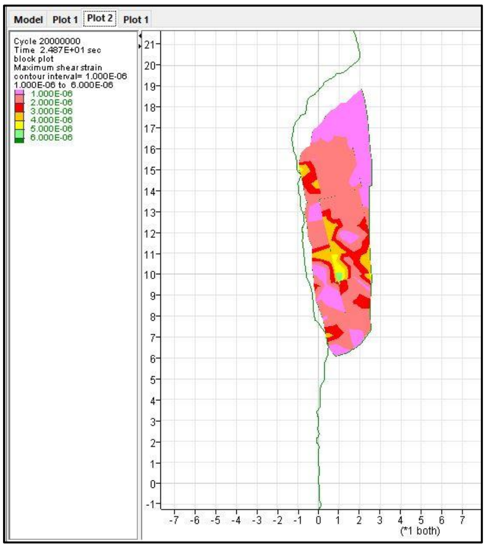

Fig. 126: jkn = 1E11, jks = 1E5, c = 2E7, step 2E7

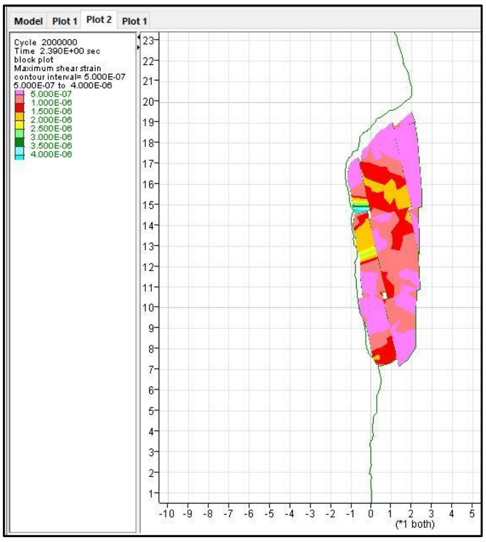

Fig. 127: jkn = 1E11, jks = 1E5, c = 0, step 2E6

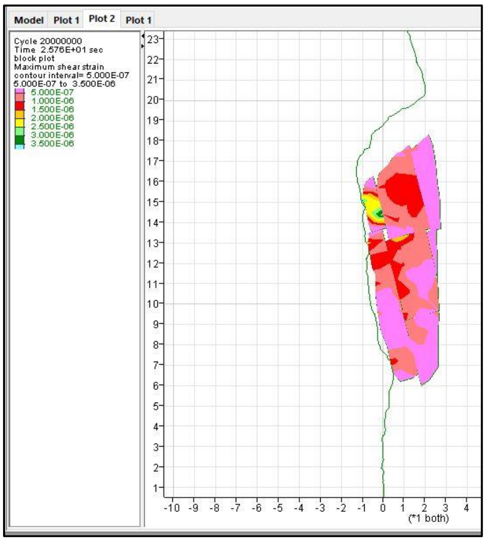

Fig. 128: jkn = 1E11, jks = 1E5, c = 0, step 2E7

Grid data highlighting the failure mechanisms using orientation data from ShapeMetrix3D with Dips 7.0

Orientations				Failure Mechanisms			
ID	Dip Direction	Dip	Set	Planar Sliding	Planar Sliding (No Limits)	Flexural Toppling	Direct Toppling (Base Plane)
1	174	87	**1**				
2	332	85					
3	161	58				Toppling	
4	142	55				Toppling	
5	196	64					
6	149	81				Toppling	
7	346	74					
8	184	78					
9	159	69				Toppling	
10	174	76					
11	151	82				Toppling	
12	173	86					
13	167	84					
14	176	81					
15	192	68					
16	175	69					
17	156	79				Toppling	
18	181	53					
19	174	55					
20	336	86					
21	182	71					
22	341	88					
23	184	67					
24	156	74				Toppling	
25	341	87					
26	167	84					
27	182	54					
28	191	86					
29	5	87					
30	29	83					
31	207	85					
32	179	89					
33	175	85					
34	200	83					
35	154	56				Toppling	
36	348	52			Sliding		
37	22	65					
38	27	60					
39	0	68					
40	3	54			Sliding		
41	167	85					
42	2	87					
43	160	77				Toppling	

44	18	88					
45	14	78					
46	2	69					
47	175	75					
48	23	57					
49	170	80					
50	346	87					
51	185	69					
52	336	86					
53	350	89					
54	339	81					
55	333	87					
56	154	86				Toppling	
57	334	80					
58	8	82					
59	337	83					
60	169	89					
61	14	83					
62	182	80					
63	169	87					
64	353	82					
65	193	83					
66	1	75					
67	168	89					
68	174	88					
69	341	85					
70	358	82					
71	157	89				Toppling	
72	167	73					
73	337	88					
74	354	88					
75	355	88					
76	187	86					
77	338	87					
78	4	81					
79	343	87					
80	193	87					
81	181	81					
82	159	89				Toppling	
83	340	90					
84	192	87					
85	189	82					
86	352	86					
87	173	73					
88	150	86				Toppling	
89	259	12	**2**				Sliding+Base
90	111	43					

91	138	18					
92	214	50					
93	236	5					Sliding+Base
94	203	17					
95	295	31			Sliding		
96	249	23					Sliding+Base
97	138	14					
98	147	23					
99	200	13					
100	280	24					Sliding+Base
101	199	19					
102	164	5					
103	248	26					Sliding+Base
104	136	1					
105	282	13					Sliding+Base
106	224	5					
107	177	11					
108	250	11					Sliding+Base
109	341	42		Sliding	Sliding		Base
110	346	25					Sliding+Base
111	240	8					Sliding+Base
112	312	38		Sliding	Sliding		Base
113	281	24					Sliding+Base
114	281	7					Sliding+Base
115	213	12					
116	307	29					Sliding+Base
117	285	22					Sliding+Base
118	127	23					
119	338	7					Sliding+Base
120	209	2					
121	267	39			Sliding		
122	221	43					
123	261	42			Sliding		
124	215	25					
125	192	44					
126	283	21					Sliding+Base
127	235	29					
128	287	22					Sliding+Base
129	232	33					
130	275	50			Sliding		
131	251	33			Sliding		
132	239	41					
133	191	23					
134	276	52			Sliding		
135	260	43			Sliding		
136	213	37					
137	277	48			Sliding		

138	206	48					
139	37	37			Sliding		
140	75	24					
141	51	13					Sliding+Base
142	68	35					
143	114	26					
144	338	41		Sliding	Sliding		Base
145	84	36					
146	39	42					
147	313	34		Sliding	Sliding		Base
148	287	48			Sliding		
149	327	42		Sliding	Sliding		Base
150	249	89	**3**				
151	100	79					
152	97	63					
153	249	76					
154	277	53			Sliding		
155	260	71					
156	276	67					
157	260	72					
158	264	90					
159	269	90					
160	242	88					
161	252	88					
162	67	86					
163	95	89					
164	272	81					
165	75	79					
166	277	76					
167	70	88					
168	91	90					
169	70	86					
170	246	80					
171	249	77					
172	240	87					
173	251	80					
174	275	78					
175	262	78					
176	272	68					
177	254	80					
178	95	66					
179	83	54					
180	78	65					
181	90	52					
182	77	69					
183	72	58					
184	267	79					

185	278	75					
186	219	65					
187	225	72					
188	47	87					
189	32	70					
190	233	82					
191	224	80					
192	48	86					
193	236	79					
194	230	76					
195	212	88					
196	44	51					
197	33	78					
198	36	64					
199	43	75					
200	34	51					
201	42	78					
202	222	52					
203	210	57					
204	255	59					
205	309	84	**4**				
206	306	85					
207	294	77					
208	308	81					
209	306	88					
210	297	79					
211	318	87					
212	124	46					
213	106	53					
214	138	50					
215	109	50					
216	141	84				Toppling	
217	320	86					
218	123	83					
219	301	48			Sliding		
220	316	47		Sliding	Sliding		Base
221	323	68		Sliding	Sliding		Base
222	311	70					Base
223	284	72					
224	306	84					
225	114	82					
226	146	90				Toppling	
227	299	79					
228	312	85					
229	126	89				Toppling	
230	118	70					
231	317	85					

232	101	81				
233	112	58				
234	324	58	Sliding	Sliding		Base
235	102	61				
236	101	53				
237	104	62				
238	321	80				
239	295	89				
240	312	80				
241	332	76				
242	311	79				
243	306	72				
244	318	86				
245	306	88				
246	283	83				
247	296	84				
248	292	82				
249	280	73				
250	307	78				
251	308	83				
252	301	87				
253	297	74				
254	300	65		Sliding		
255	141	88			Toppling	
256	329	86				
257	316	83				
258	118	87				
259	309	73				
260	313	79				
261	326	86				
262	326	74				
263	129	82			Toppling	
264	312	80				
265	310	79				
266	119	83				
267	284	75				
268	303	90				
269	315	69	Sliding	Sliding		Base
270	133	64			Toppling	
271	297	83				
272	279	62				
273	142	88			Toppling	
274	287	90				
275	308	78				
276	146	88			Toppling	
277	295	75				
278	305	78				

279	143	84				Toppling	
280	139	78				Toppling	
281	321	79					
282	318	74					
283	313	77					
284	329	72					
285	312	82					
286	141	88				Toppling	
287	320	78					
288	323	82					
289	311	67		Sliding	Sliding		Base
290	311	86					
291	317	68		Sliding	Sliding		Base
292	311	76					
293	307	79					
294	146	85				Toppling	
295	293	84					
296	294	64			Sliding		
297	314	74					
298	319	83					
299	309	85					
300	322	90					
301	326	67		Sliding	Sliding		Base
302	332	75					
303	316	65		Sliding	Sliding		Base
304	309	76					
305	297	55			Sliding		
306	304	75					
307	297	67			Sliding		
308	280	77					
309	303	78					
310	310	74					
311	304	81					
312	314	82					
313	302	87					
314	310	74					
315	319	81					
316	314	88					
317	318	79					
318	290	83					
319	330	81					
320	144	89				Toppling	
321	328	83					
322	114	81					
323	302	83					
324	330	76					
325	340	52		Sliding	Sliding		Base

326	149	83				Toppling	
327	330	86					
328	330	85					